FIRST-PRINCIPLES STUDY OF METAL–CERAMIC INTERFACES

BY

DONALD JASON SIEGEL

B.S., Case Western Reserve University, 1995

THESIS

Submitted in partial fulfillment of the requirements
for the degree of Doctor of Philosophy in Physics
in the Graduate College of the
University of Illinois at Urbana-Champaign, 2001

Urbana, Illinois

FIRST-PRINCIPLES STUDY OF METAL–CERAMIC INTERFACES

Donald Jason Siegel, Ph.D.
Department of Physics
University of Illinois at Urbana-Champaign, 2001
James B. Adams, Advisor

Despite their use in a variety of applications, the fundamental properties of metal–ceramic interfaces are still poorly understood. Historically, this has been due to experimental complications associated with the study of a buried interface, and to theoretical difficulties caused by complex interfacial bonding interactions. However, the advent of first-principles techniques based on Density Functional Theory (DFT) has led to new opportunities for highly-accurate computer simulations of the atomic and electronic structure of interfaces.

In this study we present a series of DFT calculations on a broad class of Al/ceramic interface systems, with the goal of explaining and predicting the nature of metal–ceramic adhesion. Since the strength of interfacial bonding, as quantified by the ideal work of adhesion $\mathcal{W}_{\rm ad}$, plays a crucial role in determining the mechanical properties of an interface, we have systematically calculated $\mathcal{W}_{\rm ad}$ for 20 different interface geometries including oxide (α–Al_2O_3), carbide (WC, VC), and nitride (VN) ceramic compounds with the goal of identifying trends. In order to identify the optimal atomic structures we consider the effects of several stacking sequences, interface terminations (both polar and non-polar), and allow for full atomic relaxations. For each system we use a variety of methods to carefully analyze the interfacial electronic structure in order to determine the nature of the metal–ceramic bonding.

Although we find significant differences in both the interfacial bonding and the inherent electronic structures of the bulk ceramics, our calculations reveal a trend in $\mathcal{W}_{\rm ad}$ with respect to the summed surface energies of the interfaced materials ($\sigma_{\rm Al} + \sigma_{\rm ceramic}$). Specifically, we find that surfaces having larger σ's adhere at interfaces more strongly than those with small σ's. We argue that this behavior is consistent with the intuitive notion of the surface energy being a measure of surface reactivity, and hence it could be used as a guide in the design of interfacial properties.

To my parents.

Acknowledgments

My greatest debt is to my advisor, Jim Adams, whose guidance, patience, imagination, and insight have been a positive influence on both my professional and personal development.

Lou Hector, Jr., served as my industrial advisor, and is responsible (or to blame) for introducing me to the practical aspects of *ab initio* simulation techniques. His enthusiasm, determination, energy, and friendship are greatly appreciated.

For serving on my Ph.D. committee, I thank Professors Richard Martin, Jim Eckstein, and Vijay Pandharipande. (Additional thanks to Richard Martin for serving as my *de facto* UIUC advisor during Jim's absence.)

I have grown immensely from many interactions with other group members, both students and postdocs. A large fraction of my learning was made possible through their generosity and patience. Of these, I offer special thanks to Debasis Sengupta, Blair Tuttle, Dave Richards, Rampi Ramprasad, and Bryan Goodman. Also, Karland Killian, Ben Liu, Sang Yang, Chun-Li Liu, Keith Glassford, Hualiang Yu, Youhong Li, Zhiyong Wang, Jie Zhang, Shahriar Anwar, Donghai Sun, Jaya Rajaraman, and Jun Zhong.

During the summer of 2000 I had the good fortune to be an intern at the GM Materials and Processes Lab, where I benefited from daily interactions with my mentors, Y. T. Cheng and Tom Perry.

Georg Kresse was an invaluable source of VASP information, and along with J. Hafner, made my use of that code possible.

Computational resources and consulting for this thesis were provided by the National Computational Science Alliance (NCSA) at the University of Illinois at Urbana-Champaign under grant MCA-96N001N. Financial support was provided by the National Science Foundation Division of Materials Research under grant DMR-9619353.

Lastly, (but by no means least,) I thank Annette Ostling, whose friendship and love have inspired me throughout my graduate studies.

Table of Contents

List of Tables

List of Figures

Chapter 1

Introduction

1.1 Motivation

Metal–ceramic interfaces play a vital role in modern materials technology, as evidenced by their use in a variety of applications. For example, high-strength materials such as metal-matrix composites consist of internal interfaces between ceramic (eg., SiC or Al_2O_3) particles or filaments within a metallic host. Because of their high melting points, extreme hardness, and favorable corrosion resistance, ceramic coatings are often used to protect an underlying metallic component in environments subject to high temperatures and wear rates (i.e., cutting tools). As environmental concerns regarding greenhouse gas emissions and NO_x pollutants have increased, so too have efforts to optimize the mechanisms of heterogeneous catalysis. Because traditional automotive catalysts rely on transition metal clusters supported by ceramic substrates, understanding these cluster-surface interactions will continue to be a prime focus in the chemical and automotive industries for years to come. Lastly, in microelectronics packaging, interfaces between metallic (Cu and/or Al) interconnects and SiO_2 or other carbide/nitride ceramics (TiN) are commonplace, and impact the performance and longevity of solid state devices.

Despite their widespread use, a basic understanding of these interfaces has been elusive. For example, given a particular heterophase interface system, it is not yet possible to accurately predict such fundamental properties as its fracture energy. Also, it is still a matter of debate as to which are the dominant bonding mechanisms at selected metal–oxide interfaces[1, 2]. Historically, these failings have been due to experimental complications associated with the study of a buried interface, and theoretical difficulties arising from complex interfacial bonding interactions. A further stumbling block impeding the prediction of the mechanical properties of interfaces arises from their multi-length-scale nature. That is, while many of the favorable properties of these interfaces manifest themselves on the meso- or macroscales, these attributes are intimately coupled to the detailed atomic and electronic *nanostrucuture* at the junction. Only very recently has a multi-scale theory of homophase materials appeared[3], and extension to heterophase systems is still far into the future. For the most part, improvements in interface properties proceed via a costly and time-consuming trial-and-error process in which numerous materials are evaluated until suitable performance is obtained.

In addition to their appeal from a basic science standpoint, further motivation for the study of metal–

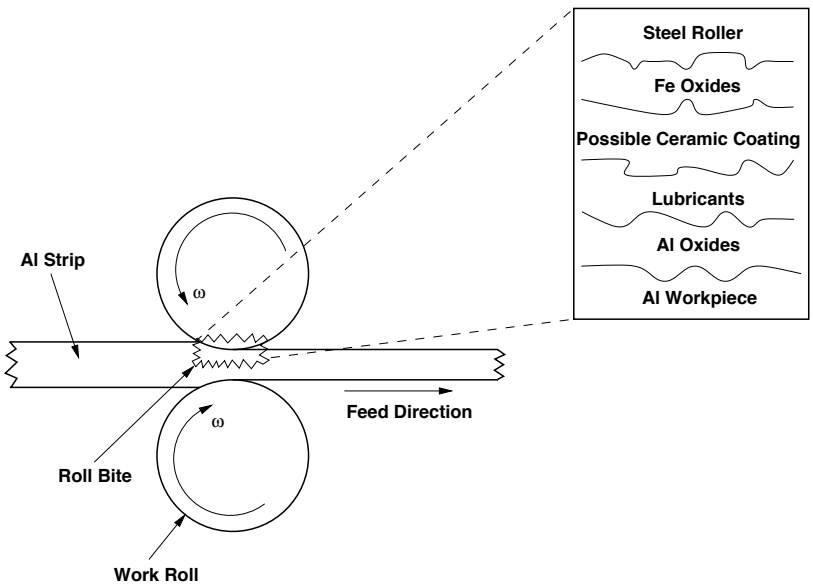

Figure 1.1: The Al strip rolling process.

ceramic interfaces stems from a collaboration with the Aluminum Company of America (ALCOA) and, more recently, General Motors, Inc. In aluminum manufacturing one of the most common problems is that of adhesion and adhesive metal transfer, in which the aluminum workpiece material adheres to the surface of another material (the toolpiece) along a heavily loaded interface[4]. It is especially prevalent in the aluminum industry, for example, where thick ingots are subjected to massive loads in numerous hot and cold rolling processes that form a cast ingot into strip and plate products (see Fig 1.1). The surface oxide common to aluminum is broken up within the lubricant-depleted roll bite under extreme normal loads to expose nascent metal which subsequently adheres to the roll surface. As the two surfaces part, small quantities of aluminum remain on the roll surface only to be brought back into contact with the product surface as it re-enters the roll bite. What eventually results is an aluminum coating of the roll surface, the thickness of which usually stabilizes, but under certain circumstances can become unstable. In either case, adhesive metal transfer of softer aluminum to the surface of steel work rolls leads to degradation of vitally important product surface attributes such as distinctness of image clarity, fluid retention, spot weldability, and cleanliness. The transferred material forms a new surface on the rollers that abrades the product surface, generating unmitigated levels of debris in the roll bite. The debris particles increase the load on the mill and on the oil filtration house, and generate a dirty product surface. Extra steps, that are often quite costly, must be added to the overall manufacturing process to remove adhered material before it can damage the product surface.

One means through which adhesive metal transfer from the strip to the tool surface can be reduced is through the application of a ceramic tool coating that protects the tool surface for an extended period of time. Unfortunately, no guidelines currently exist for the design of tool coatings that minimize or prevent adhesive metal transfer of aluminum alloys to tool surfaces. There have been some attempts to develop rudimentary guidelines based on simple thermodynamic models[5, 6], but these models are generally inconsistent in

their ability to predict how a selected coating material will perform in even the simplest laboratory forming process. Thus there is a glaring need for a fundamental understanding of the basic mechanisms of metal adhesion and transfer to ceramic surfaces.

In a similar manner, scientists at General Motors are in search of mechanisms by which to reduce adhesion during the "green machining" of Al engine parts. Traditionally, a machining operation such as drilling would involve the use of a lubricant to prevent adhesion of the machined debris to the tool piece. However, concerns about the safety of vaporized lubricants (caused by high working temperatures) to the health of machine operators has resulted in a push for dry processes that do not require lubricants. The goal then is to identify ceramic tool coating materials that adhere weakly to Al and its alloys.

1.2 Definitions

A fundamental quantity which influences the mechanical properties of an interface is the ideal work of adhesion, $\mathcal{W}_{\rm ad}$[7], which is defined as the energy required to break interfacial bonds and reversibly separate an interface into two free surfaces, neglecting diffusion and plastic deformation (see Fig 1.2). When combined with the work of plastic deformation $\mathcal{W}_{\rm plastic}$, the work of adhesion determines the fracture energy of an interface, Γ:

$$\Gamma = \mathcal{W}_{\rm ad} + \mathcal{W}_{\rm plastic}. \tag{1.1}$$

However, since the degree of plastic deformation which occurs during interfacial fracture is known to depend upon $\mathcal{W}_{\rm ad}$[8–10],

$$\mathcal{W}_{\rm plastic} = \mathcal{W}_{\rm plastic}(\mathcal{W}_{\rm ad}), \qquad \text{and thus,} \tag{1.2}$$

$$\Gamma = \Gamma(\mathcal{W}_{\rm ad}). \tag{1.3}$$

On its own, $\mathcal{W}_{\rm ad}$ therefore serves as a lower bound to the amount of energy needed to cleave an interface. Formally, $\mathcal{W}_{\rm ad}$ is defined either in terms of the surface and interfacial energies (relative to the respective bulk materials) or by the difference in total energy between the interface and its isolated surfaces:

$$\mathcal{W}_{\rm ad} = \sigma_{1v} + \sigma_{2v} - \gamma_{12} = \left(E_1^{\rm tot} + E_2^{\rm tot} - E_{12}^{\rm tot}\right)/A. \tag{1.4}$$

Here σ_{iv} is the surface energy of slab i, γ_{12} is the interface energy, $E_i^{\rm tot}$ is the total energy of slab i, and $E_{12}^{\rm tot}$ is the total energy of the interface system. The total interface area is given by A. (Note that in the case where the interfaced materials are identical (1 = 2), then $\mathcal{W}_{\rm ad} = 2\sigma_1$.)

The $\mathcal{W}_{\rm ad}$ can also influence where an interface fails, as it is known that strongly adhering media tend to fail within one of the individual slabs (with adhesive transfer to the other) rather than at the interface. One way to check for the possibility of adhesive transfer is to compare $\mathcal{W}_{\rm ad}$ with twice the surface energy of each material. If $2\sigma_i \leq \mathcal{W}_{\rm ad}$ then adhesive transfer could be possible. However, it is more rigorous to evaluate this inequality by replacing $2\sigma_i$ with the $\mathcal{W}_{\rm ad}$ as determined for cleavage inside one of the media, since for

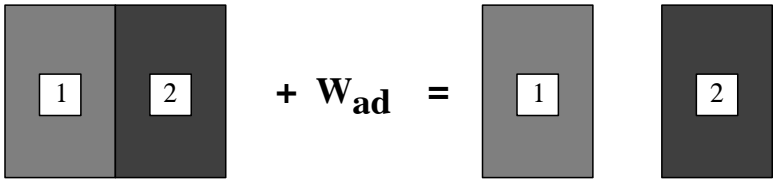

Figure 1.2: Definition of the work of adhesion.

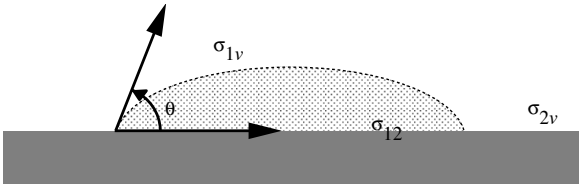

Figure 1.3: The sessile drop wetting process. θ is the wetting angle, σ_{12} is the interfacial energy, and σ_{iv} represent the surface energies of the drop and substrate.

cleavage close to the interface the work to form two surfaces may not equal 2σ.[1]

Although $\mathcal{W}_{\text{ad}}$ and γ_{12} both relate information regarding the state of an interface, $\mathcal{W}_{\text{ad}}$ is more relevant for a discussion of mechanical properties since it directly characterizes the strength of interfacial bonding. In contrast, γ_{12} gives the free energy of an interface in excess to that found in the corresponding bulk materials (or equivalently, it expresses how much weaker/stronger the interfacial bonding is with respect to that found in the bulk):

$$\gamma_{12} = \left(E_{12}^{\text{tot}} - E_1^{\text{bulk}} - E_2^{\text{bulk}}\right)/A. \tag{1.5}$$

It should be noted, however, that use of γ_{12} is desirable in other contexts, such as in studies of interfacial segregation and stability, as will be demonstrated in Chapter 4. Lastly, $\mathcal{W}_{\text{ad}}$ is more approachable from an experimental standpoint, as it can be extracted from the sessile drop experiments discussed below.

1.3 Review of the Literature

1.3.1 Experimental Studies and Empirical Correlations

Perhaps the most straightforward and common way to determine $\mathcal{W}_{\text{ad}}$ experimentally is through a sessile drop experiment[7, 11] (see Fig. 1.3). Roughly speaking, the procedure involves the application of a drop of liquid metal to a ceramic substrate; the contact angle θ between the drop profile and the surface plane of the ceramic is then measured. The contact angle characterizes the degree to which the metal "wets" the ceramic, and two (somewhat arbitrary) regimes can be identified:

$$\theta < 90^\circ \qquad \text{wetting}, \tag{1.6}$$

$$\theta > 90^\circ \qquad \text{non-wetting}. \tag{1.7}$$

[1] For example, the cleavage point could fall within in a non-bulk-like region close to the interface, whereas σ_i is usually determined using a bulk-like slab.

The greater the wetting the greater the strength of metal–ceramic interaction. By combining the Young equation[12]:

$$\cos\theta = \frac{\sigma_{2v} - \gamma_{12}}{\sigma_{1v}}, \tag{1.8}$$

with the Dupré equation (the first half of Eq. 1.4) it is possible to eliminate the interfacial energy γ_{12} and express the $\mathcal{W}_{\rm ad}$ in terms of the metal's surface energy and the contact angle (the Young-Dupré equation):

$$\mathcal{W}_{\rm ad} = \sigma_{1v}(1 + \cos\theta). \tag{1.9}$$

Although it would now seem that a direct comparison could be made between $\mathcal{W}_{\rm ad}$ from a theoretical calculation (see below) to the contact angle from experiment, one must proceed with caution. In particular, the experimental $\mathcal{W}_{\rm ad}$ derived from Eqns. 1.8-1.9 depends upon surface and interfacial energies which are in *equilibrium* with the surrounding vapor and contiguous bulk phases. The presence of surface/interfacial diffusion will likely result in different compositions from those assumed in the calculation, and will result in correspondingly different σ and γ values. There are often additional differences between experiment and theory, such as temperature effects and structural differences related to a liquid-solid interface vs. a solid-solid system. In all, it is perhaps best to assume no more than qualitative agreement between the calculated and experimental $\mathcal{W}_{\rm ad}$ values. A recent compilation of experimental data pertaining to the wettability of ceramics by liquid metals can be found in Ref. [13].

Our understanding of the nature of metal–ceramic adhesion is still mainly derived from simplistic empirical correlations. Several authors have identified experimental trends in the wettability of ceramics by liquid metals (see Refs. [7, 13–17]), some of which include:

- The wettability of an oxide by a metal increases with the heat of formation of the metal's oxide.
- The wettability of oxides and carbides decreases as their ionicity or heat of formation increases. For a given metal, the wettability improves as the ceramic's bonding becomes more covalent.
- The addition of oxygen to a metal improves its adhesion to an oxide.
- The addition of an element (y), which reduces the oxide substrate, to a wetting metal (x), enhances adhesion.

Needless to say, these correlations say nothing about the effects of crystallographic structure and orientation of the interfaced media. Moreover, they are unable to predict the nature of interfacial bonding.

1.3.2 Analytic Models

At present, there are no accurate and general analytical models capable of predicting the adhesive properties between a given metal and ceramic. However, two models have been developed which attempt to predict only the strength of dispersion forces (van der Waals-type interactions) at an interface. Barrera and Duke[18] devised one of the first such models based on dielectric continuum theory. Although their approach formulated the metal–ceramic contact angle in terms of a few easily determined bulk properties, it was later shown to give inconsistent results when compared to the wetting of both oxides[19] and carbides[20].

Lipkin *et al*.[21] also developed an analytical expression for estimating the van der Waals contribution to the adhesion energy at metal/oxide interfaces. This provided a lower-bound estimate of the measured adhesion energies for Al/alumina and several other non-reactive metal/alumina systems, and found that adhesion involving the noble metals Cu, Au, and Ag was well accounted for by dipole-dipole interactions alone. To our knowledge, no models exist which attempt to account for all the possible interface interactions, including covalent, ionic, and metallic bonding.

1.3.3 First-Principles Simulation

Given the limitations of the models mentioned above, and the incomplete data provided by empirical correlations, it is clear that more accurate and detailed methods are necessary for a thorough understanding of metal–ceramic adhesion. With the advent of simulation techniques based on Density Functional Theory (DFT)[22, 23], a clearer picture of the atomic and electronic structure of these interfaces is beginning to emerge. These methods are collectively referred to as "first-principles" or *ab initio* because they do not rely upon experimental input other than the atomic mass and number of a given species. The fundamental electronic interactions are treated at the quantum-mechanical level through a self-consistent solution of a Schrödinger-like wave equation. In this section we briefly review the existing studies of adhesion which have utilized these techniques.

The primary reasons for using first-principles methods to study metal–ceramic interfaces are their generality and accuracy. Because of the disparity in electronic structure between metals (where bonding is often dominated by delocalized electrons) and ceramics (generally having localized covalent bonds or ionic interactions), bonding at the interface can involve any combination of metallic, covalent, ionic, or via polarization. This variety makes it nearly impossible to develop empirical or semi-empirical atomistic models wherein one must pre-suppose the undetermined nature of the atomic interactions. Since the self-consistent nature of a DFT calculation requires no such foreknowledge, and is general enough to describe a range of bonding interactions, it provides a natural, unbiased choice for such studies.

The accuracy of first-principles methods have been well established in the context of total-energy bulk calculations[24]. For the most part, properties such as the lattice constants, cohesive energies, elastic constants, phonon dispersion curves, formation enthalpies, and other quantities dependent upon total energies agree with experiment to within 10% or less. On the other hand, excited-state properties such as band gaps can be moderately to severely underestimated depending on the details of a material's electronic structure (eg., NiO is erroneously predicted to be a metal rather than an insulator). However, these shortcomings are not due to errors in what is explicitly a *ground state* theory, but are rather caused by attempts to apply the methodology for purposes which it was not designed (see Chapter 2 for more details on the fundamentals of DFT). Because of computational limitations on the number of atoms which may be simulated, it is not currently possible to fully predict the mechanical properties or strength of a material; the processes (plastic deformation, misfit dislocations, *etc*.) which control these properties occur over inaccessible time and length scales. Nonetheless, the *energetics* upon which those mechanisms depend (Eqns. 1.1-1.3) *can* be accurately calculated within DFT, and therein lies the value of a first-principles approach. In addition, the ability to

explicitly specify and manipulate the atomic arrangement of a system within a computer simulation allows the investigation of interfacial phenomena at a level of detail not attainable by experiment. Finally, since a converged DFT calculation yields as output the ground state charge density, a comprehensive analysis of the system's electronic structure is routinely available.

Early Studies: Metal–Oxide Systems

The first *ab initio* calculations of adhesion were performed on metal/oxide interfaces, and these systems have remained as the focus of intensive study during the last few years. One of the first such calculations was performed by Freeman and co-workers[25]. They used the full-potential linearized augmented-plane-wave method (FPLAPW)[26] to study a Ag monolayer adsorbed on a rigid MgO(001) surface, and determined that the preferred adsorption site for the Ag atoms was above the O sites. They also examined the electronic structure and binding energy of the Ag/CdO(001) interface[27] (again using a monolayer-on-rigid-slab configuration) and have investigated the magnetic properties of *M*/MgO(001) interfaces, with *M* representing monolayers of Fe, Pd, Rh, and Ru[28, 29].

Smith and co-workers used a self-consistent local orbital method (LCAO)[30] to study two metal/oxide interfaces, Ag/MgO(100) and Al/MgO(100), including the effects of an interfacial monolayer of C or S impurities[31–33]. In addition to calculating the energetics of adhesion and the electronic structure of these interfaces, they found that for rigid slabs the adhesive energy versus interfacial separation curves accurately obeyed the universal binding energy relation[34, 35]. Somewhat unexpectedly, they also showed that the non-self-consistent Harris functional[36, 37] gave interfacial results in good agreement with the self-consistent calculations. (Smith has conducted additional calculations of interfacial adhesion in the transition metals Mo, Nb and V and the intermetallic compound $MoSi_2$[38], and has studied the effects of monolayers of C, O, B, S and Nb impurities on adhesion at those interfaces[39, 40].)

Schönberger, Anderson, and Methfessel employed the full-potential linearized muffin-tin orbital method (FLMTO)[41] to study the Ti/MgO(001) and Ag/MgO(001) interfaces[42]. Using a rigid MgO slab, they found that the preferred binding site for both Ti and Ag was above the O sites, and that the interface force constants for the Ti/MgO interface were 3–4 times larger than those for Ag/MgO.

Lastly, Finnis and co-workers used both FLMTO and pseudopotential-based planewave[24] methods to study three interfaces: Ti/MgO, Ag/MgO, and a Nb monolayer adsorbed on a Al_2O_3 surface[43, 44]. For these systems they were able to calculate the ideal work of adhesion, the nature of the interfacial bonding, the local electronic densities of states, and the electronic charge distribution.

The calculations discussed above demonstrate that pioneering *ab initio* calculations of metal-ceramic interfaces became possible during the early and mid-1990's. However, problems with computational throughput and algorithmic efficiency limited the applicability of these methods to relatively small (model) systems that could not account for more realistic effects such as atomic relaxations, slab thickness, or interfacial defects like vacancies and misfits. Recent advances have made such studies possible, and below we present a brief review of the most recent developments involving metal–ceramic systems.

Recent Progress: Realistic Metal–Ceramic Interfaces

Following up on their earlier study of the rigid Nb/α–Al_2O_3 interface, Batirev and co-workers[45] completed a fully relaxed study of the same system, considering both Al– and O–terminations of the ceramic. A mixture of ionic and covalent bonds characterized the interfacial electronic structure, while $\mathcal{W}_{\rm ad}$ calculated at the interface was found to be larger than in the metal, suggesting a failure mode within the Nb.

Further studies using Al_2O_3 as the ceramic have been performed by two groups. The Sandia group[1, 46] has authored the only studies of trends in metal–ceramic adhesion, wherein they calculated adsorption/adhesion energies of several M/Al_2O_3 interfaces, (M = mainly transition metals) at coverages ranging from 1/3 to 4 monolayers (ML). They established that, with a few exceptions, the dominant bonding mechanism at low metal coverages ($\sim \frac{1}{3}$ ML) was ionic, and due to metal polarization at higher coverages. Oxide relaxation effects were found to be significant for the prediction of accurate energetics.

Zhang and Smith[47] conducted the first study of interfacial stability of non-stoichiometric interfaces involving Al and Ag on α–Al_2O_3(0001). By calculating the interfacial free energy as a function of oxygen partial pressure, they determined that the Al/α–Al_2O_3 interface is oxygen terminated at all but the lowest of oxygen potentials. Conversely, Ag/α–Al_2O_3 was mainly Al terminated until switching over to oxygen termination at higher potentials. Calculated $\mathcal{W}_{\rm ad}$ values for both metal/oxide systems were in good agreement with wetting experiments. We perform a similar stability analysis upon the Al/WC interface in Chapter 4.

Recognizing that defects play an important role in adhesion of metals to ceramics, Zhukovskii and co-workers[48] presented the first *ab initio* study including the effects of interfacial ceramic vacancies for Ag/MgO. While bonding was found to be relatively weak and due to Ag polarization for the defect-free systems, $\mathcal{W}_{\rm ad}$ values increased by roughly an order of magnitude upon inclusion of electron F_s or hole V_s centers. Defect sites induced interfacial charge transfer and the formation of ionic bonds.

An additional study upon defect effects was performed by Benedek *et al*[49] on the $\{222\}$MgO/Cu polar interface system. To accommodate a relatively large mismatch of $\sim$ 17%, a 399-atom supercell was constructed that explicitly included the mismatch geometry. Relaxed geometries showed a significant warping of both the ceramic and metal interfacial layers, as those atoms situated close to 3-fold hollow sites tended to minimize their interfacial distance. (On top sites were found to be least favorable.) The relatively large $\mathcal{W}_{\rm ad}$ of 3.6 eV per interface O atom was found to be slightly larger than that for the coherent model[50] (3.1 eV), although a different pseudopotential was used in each calculation.

Although the above citations suggest that there has recently been much activity aimed at understanding metal/oxide interfaces, much less is known about metal–ceramic adhesion involving non-oxide ceramics. Within this class, the transition metal carbides and nitrides are a particularly notable omission, considering their exceptional hardness, strength, and corrosion resistance[51]. To our knowledge, there have been only two studies of adhesion between metals and transition metal carbides/nitrides based on Density Functional Theory(DFT), along with a few earlier studies[52–54] performed using semi-empirical methods. Hartford[55] calculated the interfacial free energy of the Fe/VN system, including the effects of N vacancies. The interface energy was found to be negative for all systems consisting of more than one VN layer, with the presence of vacancies resulting in a small increase in interfacial energy. The interfacial bonds

were determined to consist mainly of covalent N(p)–Fe(d) σ interactions, with minor V(d)–Fe(d) character. Secondly, Dudiy and co-workers[56] examined the Co/TiC interface, and found that their calculated $\mathcal{W}_{\rm ad}$ values agreed with wetting experiments to within 10%. The dominant bonding mechanism involved strong "metal-modified" covalent Co–C bonds.

We are not aware of any theoretical studies which examine adhesion of Al (which is the focus of this thesis) to transition metal carbides/nitrides. However, two groups have used DFT to study interfaces of Al with other non-oxide ceramics. Hoekstra and Kohyama[57] considered the polar Al/β-SiC(001) interface, and found relatively large adhesion energies of 6.42 and 3.74 J/m^2 for both C and Si terminations, respectively. Conversely, a relatively weak adhesion of about 0.9 J/m^2 was found for the Al/AlN system by Ogata and Kitagawa[58].

1.4 Goals of this Study

Now that we have provided a background in some of the previous experimental and theoretical studies of metal–ceramic interfaces, we identify how this work will build upon that foundation.

The purpose of this thesis is to use first-principles simulation methodologies to systematically examine and predict the mechanical (adhesion), structural (atomic geometries), and electronic properties (bond type) of several different classes of metal–ceramic interfaces. Although an ever-growing number of these systems has now been studied by both theoretical and experimental methods, the disparity of methods used (especially in the context of the *ab initio* calculations), has made the extraction of trends across studies performed by different groups difficult or impossible. A broad and consistent sampling of interfacial properties is therefore needed to establish trends and facilitate predictions. To address this lack of consistency we have examined the significance of the ceramic component on adhesion at interfaces with Al. In all, we have considered 20 different interface geometries spanning a broad class of ceramic compositions (oxides, carbides, and nitrides) and terminations (both polar and non-polar). The breadth of this study has not implied a sacrifice in depth of analysis, as the electronic structure of each interface presented has been carefully analyzed.

Before proceeding further we give a brief outline of this document: In Chapter 2 we discuss the computational methods employed herein. We start with an overview of the many-body electron problem and its solution via Density Functional Theory. Then we discuss the issues of exchange correlation energy and the other practical aspects of a planewave, pseudopotential implementation of DFT. An overview of the tools used to classify interfacial bonding concludes the chapter.

Chapter 3 formally begins the discussion of metal–ceramic adhesion by analyzing our first interface system, Al/α–Al_2O_3. We open first with a more detailed summary of the literature that was omitted from Chapter 1. After presenting the results of our bulk and surface validation tests, we consider the structure and bonding of the Al– and O–terminated geometries. A thorough analysis of the electronic structure for both models is presented through use of the Electron Localization Function, density of states, Mayer bond orders, and Mulliken populations. We find that the calculated $\mathcal{W}_{\rm ad}$ for the optimal Al–terminated interface is in good agreement with the value predicted by wetting experiments.

Chapter 4 addresses the relatively unexplored issue of metal–carbide adhesion in the form of the Al/WC interface. Here we follow roughly the same outline as in Chapter 3, considering the bulk, surface, and interface properties in succession. However, in addition to calculating $\mathcal{W}_{\rm ad}$ we also determine the interfacial energy in order to predict the most stable interface structure. Again, we analyze the electronic structure and draw comparisons between the bonding at the W– and C–terminated systems.

In Chapter 5 we compare the adhesion of Al to related carbide and nitride ceramics (VN and VC) in order to establish the importance of the ceramic's metalloid component. We show that the differences in the adhesion properties of the two ceramics can be related to differences in their surface energies, which in turn reflect their "rigid band" bulk electronic structures. Similarities with earlier studies of Ag/MgO and Al/MgO are noted.

Chapter 6 presents the culmination of our work, in that it attempts to identify a trend in $\mathcal{W}_{\rm ad}$ amongst those systems presented in Chapters 3-5. We find that $\mathcal{W}_{\rm ad}$ correlates with the sum of the surface energies of the interfaced slabs.

Finally, in Chapter 7 we conclude this study with a summary of our findings and suggest some avenues for its extension.

The four main chapters of this thesis (Chapters 3-6) include the results presented in the following publications:

1. D. J. Siegel, L. G. Hector, Jr., and J. B. Adams, *Adhesion, Atomic Structure, and Bonding at the Al(111)/α-Al_2O_3 Interface: a First-Principles Study*. Submitted to Phys. Rev. B.

2. D. J. Siegel, L. G. Hector, Jr., and J. B. Adams, *Adhesion, Stability, and Bonding at Metal/Metal-Carbide Interfaces: Al/WC*. Submitted to Surf. Sci.

3. D. J. Siegel, L. G. Hector, Jr., and J. B. Adams, *First-Principles Study of Metal–Carbide/Nitride Adhesion: Al/VC vs. Al/VN*. Submitted to Acta mater.

4. D. J. Siegel, L. G. Hector, Jr., and J. B. Adams, *Trends in Metal–Ceramic Adhesion from First-Principles Simulation*. Submitted to Phys. Rev. Lett.

5. D. J. Siegel, L. G. Hector, Jr., and J. B. Adams, *Electronic Structure and Bonding at the Al–terminated Al(111)/α-Al_2O_3(0001) Interface: A First-Principles Study*. Mat. Res. Soc. Proc. V. 654, AA4.2.1 (2001).

6. D. J. Siegel, L. G. Hector, Jr., and J. B. Adams, *Stoichiometry and Adhesion of Al/WC*. Mat. Res. Soc. Proc. V. 677, AA4.25.1 (2001).

Chapter 2

Methodology

2.1 Many-Body Problem

The vast majority of physical phenomena in chemistry, biology, condensed matter physics, and materials science are determined at the atomic level, through interactions between electrons and atomic nuclei. With the development of quantum mechanics during the first decades of the 1900's, the laws governing these interactions were known, and all that remained was the daunting task of obtaining a solution. This state of affairs was summed up by Dirac in 1929: "The underlying physical laws necessary for the mathematical theory of a large part of physics and the whole of chemistry are thus completely known, and the difficulty is only that the exact application of these laws leads to equations much too complicated to be soluble[59]." For more than 70 years, obtaining solutions of the quantum-mechanical Schrödinger equation has been a primary focus of mathematical physicists and chemists; in this chapter we review the state of the art in condensed-phase quantum simulations, and describe its application to our study of interfaces.

At the heart of any quantum simulation is the need to solve (or find a suitable approximation to) the many-body problem,

$$\mathcal{H}\Psi = E\Psi, \tag{2.1}$$

where the wavefunction Ψ is a function of all the electronic $\mathbf{r}_i$ and ionic $\mathbf{R}_I$ coordinates:

$$\Psi = \Psi(\mathbf{r}_1, \mathbf{r}_2, \ldots, \mathbf{r}_N; \mathbf{R}_1, \mathbf{R}_2, \ldots, \mathbf{R}_M). \tag{2.2}$$

The physical interactions are specified by the Hamiltonian operator, $\mathcal{H}$:

$$\mathcal{H} = \frac{-\hbar^2}{2m_e}\sum_i \nabla_i^2 - \frac{\hbar^2}{2M_I}\sum_I \nabla_I^2 - \frac{1}{2}\sum_{i,I}\frac{Z_I e^2}{|\mathbf{r}_i - \mathbf{R}_I|} + \frac{1}{2}\sum_{i\neq j}\frac{e^2}{|\mathbf{r}_i - \mathbf{r}_j|} + \frac{1}{2}\sum_{I\neq J}\frac{Z_I Z_J e^2}{|\mathbf{R}_I - \mathbf{R}_J|}, \tag{2.3}$$

where the first two terms give the kinetic energy of the electrons and nuclei, respectively, the remaining three terms specify electrostatic interactions between electron-ion, electron-electron, and ion-ion pairs, respectively. The solution of Eq. 2.1 yields the total energy E and the wavefunction Ψ from which all physical properties may be derived. Unfortunately, the solution of this $3N$ + $3M$-coordinate problem is analytically

impossible for all but the smallest systems. Although essentially exact numerical solutions may be obtained using sampling techniques such as quantum Monte Carlo, these are currently limited to systems of modest size, and alternate methods are required.

One of the earliest simplifications to the problem (as proposed by Born and Oppenheimer[60]) is based upon the large differences between the masses of the electron and that of the nuclei. Since the electrons are substantially lighter than the nuclei, yet they experience the same forces through their mutual interaction, one may consider the electrons to respond instantaneously to the motions of the ions. The Hamiltonian (Eq. 2.3) can then be decoupled into an electronic part and an ionic part; only the electronic part need be considered quantum-mechanically, and the nuclear effects can be treated adiabatically via classical methods. In essence, the Born-Oppenheimer approximation reduces the many-body problem to one of $3N$ coordinates, where only the first, third, and fourth terms in Eq. 2.3 need be considered.

There have been several attempts to solve the electronic problem using approximate methods based on non-interacting single-particle wavefunctions (Hartree and Hartree-Fock[61]), or on the charge density (Thomas-Fermi-Dirac[62]). More recently, solutions based upon Density Functional Theory[22, 23] (also based upon the charge density) have become the preferred method of solution due to their accuracy and computational efficiency.

2.2 Density Functional Theory

The most crucial aspect of an electronic structure calculation is the manner by which it accounts for electron–electron interactions. The fact that electrons are both Fermions and interact via the long-ranged Coulomb potential makes for an especially complicated physical system. The Fermionic nature of the electrons, manifested in the anti-symmetry of the wavefunction, reduces the electronic energy of the system by keeping spin-aligned electrons spatially separated. This energy contribution is referred to as the *exchange energy*, and it is straightforward to include in a total-energy calculation by writing the wavefunction as a sum of Slater determinants (as is done in Hartree-Fock). The electronic Coulomb energy can be further reduced by maximizing the spatial separation between electrons with opposite spins. The *correlation energy* is thus defined as the difference between the many-body energy and the energy calculated within the Hartree-Fock approximation. Unfortunately, it is extremely difficult to calculate the correlation energy for any but the most trivial of electronic systems.

The desire to develop a simpler method for describing exchange and correlation effects led in 1964 to Hohenberg and Kohn's formulation of Density Functional Theory[22]. In principle, DFT provided an exact mapping of the complicated interacting electron problem (even in the presence of an external field like that caused by the nuclei) onto a fictitious, equivalent set of non-interacting single particles moving in an effective nonlocal potential.

The first theorem of Hohenberg and Kohn (HK) states that the ground state charge density, $n_0(\mathbf{r})$, for a system of electrons in an external potential $V_{\text{ion}}(\mathbf{r})$, *uniquely* determines that potential up to an arbitrary constant. Since $V_{\text{ion}}(\mathbf{r})$ determines the Hamiltonian, which in turn specifies Ψ through solution of the Schrödinger equation, HK had effectively identified $n(\mathbf{r})$ as the fundamental quantity of interest, thereby

reducing a problem of $3N$ dimensions to one of only 3.

The second HK theorem states that the total energy of an electronic system is a universal functional of the density $E[n(\mathbf{r})]$, and that the global minimum in energy E_0 corresponds to the ground state charge density $n_0(\mathbf{r})$.

The total energy functional can then be written in its full many-body, interacting-electron form as:

$$E[n(\mathbf{r})] = \langle\Psi|\mathcal{H}|\Psi\rangle = T[n(\mathbf{r})] + U[n(\mathbf{r})] + \int V_{\text{ion}}(\mathbf{r})n(\mathbf{r})\,d\mathbf{r}. \tag{2.4}$$

Using the Kohn-Sham[23] ansatz we can replace the many-body kinetic energy $T[n(\mathbf{r})]$ and electron–electron terms $U[n(\mathbf{r})]$ of Eq. 2.4 with the kinetic energy of a set of non-interacting electrons T_0, the classical Coulomb interaction E_{h}, *and* an additional term, E_{xc}:

$$E[n(\mathbf{r})] = T_0[n(\mathbf{r})] + \int V_{\text{ion}}(\mathbf{r})\,n(\mathbf{r})\,d\mathbf{r} + E_{\text{h}}[n(\mathbf{r})] + E_{\text{xc}}[n(\mathbf{r})]. \tag{2.5}$$

Here,

$$T_0[n(\mathbf{r})] = \frac{-\hbar^2}{2m_e}\sum_{i=1}^{N}\langle\psi_i|\nabla^2|\psi_i\rangle \tag{2.6}$$

$$E_{\text{h}}[n(\mathbf{r})] = \frac{1}{2}\int\frac{n(\mathbf{r})\,n(\mathbf{r}')}{|\mathbf{r}-\mathbf{r}'|}\,d\mathbf{r}\,d\mathbf{r}' \qquad \text{and,} \tag{2.7}$$

$$n(\mathbf{r}) = \sum_{i=1}^{N}|\psi_i(\mathbf{r})|^2. \tag{2.8}$$

Equation 2.8 represents the charge density in terms of the non-interacting single-particle wavefunctions, ψ_i. The exchange-correlation energy E_{xc} is the sum of all remaining many-body contributions (including kinetic energy effects) to the total energy. Unfortunately, its exact functional dependence upon $n(\mathbf{r})$ is unknown, and the successful implementation of DFT relies upon its accurate estimation (see below).

Assuming a form for E_{xc}, the ground state energy can be found by one of two methods. The first is based upon direct minimization of Eq. 2.5 with respect to $n(\mathbf{r})$ (or upon a related simulated annealing Car-Parrinello approach[63]), subject to the orthonormality constraint: $\langle\psi_i|\psi_j\rangle = \delta_{ij}$. Alternatively, a set of single-particle Schrödinger-like equations (the Kohn-Sham equations) may be solved self-consistently (in a manner similar to what is done for Hartree-Fock) for the non-interacting wavefunctions, ψ_i:

$$\hat{h}\psi_i(\mathbf{r}) = \left[\frac{-\hbar^2}{2m}\nabla^2 + V_{\text{eff}}[n(\mathbf{r})]\right]\psi_i(\mathbf{r}) = \epsilon_i\psi_i(\mathbf{r}) \tag{2.9}$$

$$V_{\text{eff}}[n(\mathbf{r})] = V_{\text{ion}}[n(\mathbf{r})] + V_{\text{h}}[n(\mathbf{r})] + V_{\text{xc}}[n(\mathbf{r})], \tag{2.10}$$

where,

$$V_{\rm h}[n(\mathbf{r})] = \frac{\delta E_{\rm h}[n(\mathbf{r})]}{\delta n(\mathbf{r})} \qquad \text{and,} \tag{2.11}$$

$$V_{\rm xc}[n(\mathbf{r})] = \frac{\delta E_{\rm xc}[n(\mathbf{r})]}{\delta n(\mathbf{r})} \tag{2.12}$$

Finally, in terms of the Kohn-Sham eigenvalues ϵ_i, the total energy can be expressed as:

$$E = \sum_{i=1}^{N} \epsilon_i - \frac{1}{2}\int \frac{n(\mathbf{r})\, n(\mathbf{r'})}{|\mathbf{r}-\mathbf{r'}|}\, d\mathbf{r}\, d\mathbf{r'} - \int V_{\rm xc}\,[n(\mathbf{r})] n(\mathbf{r})\, d\mathbf{r} + E_{\rm xc}[n(\mathbf{r})]. \tag{2.13}$$

2.2.1 Exchange and Correlation

As mentioned above, a practical implementation of DFT requires an approximate form of the unknown exchange-correlation (XC) energy, $E_{\rm xc}$. In a follow-up to the 1964 paper outlining DFT, Kohn and Sham[23] explained how a local approximation for $E_{\rm xc}$ could be implemented. By defining the XC energy density per electron $\epsilon_{xc}[n(\mathbf{r})]$, $E_{\rm xc}$ can be expressed as:

$$E_{\rm xc}[n(\mathbf{r})] = \int \epsilon_{\rm xc}[n(\mathbf{r})]\, n(\mathbf{r})\, d\mathbf{r}. \tag{2.14}$$

In this local approximation, $\epsilon_{\rm xc}$ for a point $\mathbf{r}$ in a condensed system with density $n(\mathbf{r})$ was taken to be equal to the XC energy per electron in a homogeneous, interacting electron gas of the same density, n:

$$\epsilon_{\rm xc}[n(\mathbf{r})] = \epsilon_{\rm xc}^{\rm hom}[n(\mathbf{r})]. \tag{2.15}$$

Within the Local Density Approximation (LDA), corrections to XC caused by nearby inhomogeneities in the density are ignored. Although there exists no *a priori* reason for the validity of the LDA, extensive testing has shown it to give unexpectedly good results for studies of condensed phases[64].

Currently, there exist several different versions of LDA functionals. Most modern forms write $E_{\rm xc}$ as a sum of separate exchange and correlation contributions. Estimating the correlation contribution tends to be more difficult; the best current estimates come from parameterizations[65] of exact many-body calculations performed by Ceperley and Alder[66].

Since the accuracy of a DFT calculation hinges upon the formulation of $E_{\rm xc}$, recently there have been numerous attempts to go beyond the LDA. In particular, the inclusion of gradient corrections to XC (the generalized gradient approximation, GGA) has shown promise especially in chemistry applications where they improve estimates of dissociation energies. In condensed phase calculations, the current slate of GGA's is known to improve cohesive energies and prediction of magnetic properties. More details on the GGA can be found in Ref. [67].

2.2.2 Supercells, Planewaves, k-point Sampling

Another practical matter which must be addressed for solution of the Kohn-Sham equations is the choice of basis set for expansion of the single-particle wavefunctions, $\psi_{\mathbf{k}n}$. Although several choices are possible in theory (some of the more exotic include wavelets and multigrids), in practice the two most common types are atomic orbitals (AO's) and planewaves (PW's). Atomic orbitals are most efficient in contexts that involve localized bonding, and as such are often used in quantum chemical calculations on atoms, molecules, and clusters. Since the shape of molecular orbitals often resembles that of atomic orbitals, usually only a small number of basis functions are needed to expand the wavefunctions. On the other hand, it can be very difficult to ensure the *completeness* of an AO basis set, which determines if properties such as the total energy are converged with respect to the number of basis functions. Other complications, such as spurious Pulay forces[68], result from the position-dependent nature of AO's, which are tied to the atomic positions.

A planewave basis set is the most common choice for simulations of crystalline systems, especially those containing metallic phases. Apart from their inherent functional simplicity, PW's have the advantage of being orthonormal and complete; the accuracy of the basis can be systematically improved by simply increasing the number of basis functions, thereby making it easy to check for convergence. One drawback to the use of PW's arises from their non-local nature: PW's put basis weight in regions devoid of charge where no basis is needed (eg., the vacuum region in a surface calculation). Since the majority of our calculations are performed using PW's, we have formulated the remainder of this discussion assuming their use.

Another challenge facing the simulation of condensed phases results from the large number of electrons ($\sim 10^{23}$), and, nearly infinite extent of the wavefunctions, required in simulating even a relatively small (1 cm^3) amount of matter. Both of these issues may be resolved by implementing periodic boundary conditions (PBC), in which a "supercell" is replicated throughout space. By creating an artificially periodic system Bloch's theorem[69] can be applied, thereby allowing the periodic part of the wavefunction $u_{\mathbf{k}n}(\mathbf{r})$ to be expanded in a discrete set of PW's whose wave vectors are the reciprocal lattice vectors $\mathbf{G}$ of the crystal structure:

$$\psi_{\mathbf{k}n}(\mathbf{r}) = \mathrm{e}^{i\mathbf{k}\cdot\mathbf{r}} u_{\mathbf{k}n}(\mathbf{r}) = \sum_{\mathbf{G}} c_{\mathbf{G}}(\mathbf{k}n)\mathrm{e}^{i(\mathbf{k}+\mathbf{G})\cdot\mathbf{r}}. \tag{2.16}$$

The use of PBC does not preclude the study of aperiodic systems such as defects and surfaces. One simply constructs a large supercell with the appropriate atomic configuration, and then checks that enough vacuum or intervening atoms are included to prevent interactions between periodic images.

The number of PW's included in a calculation determines its accuracy and computational requirements: a large basis increases the dimensions of the Hamiltonian matrix, and requires more time for its diagonalization. However, a larger basis set more faithfully reproduces small variations in the charge density. In practice a compromise is necessary, and the PW set is truncated at a cutoff energy, E_{cut}.

The quantum mechanics of a confined system dictates that the electronic states of a crystal are allowed only at a discrete set of $\mathbf{k}$-points, with the number of $\mathbf{k}$-points (and thus electrons) determined by the practically infinite number of primitive unit cells. At each $\mathbf{k}$-point only a finite number of states or bands are occupied. Fortunately, the wavefunctions from $\mathbf{k}$-points that are located close together are nearly identical, and it is therefore possible to represent several wavefunctions with just a single wavefunction from a nearby

$\mathbf{k}$-point. As such, only a finite number of "special" $\mathbf{k}$-points are needed to calculate the full charge density and hence determine the total energy of the solid. Several efficient schemes are available for choosing the $\mathbf{k}$-points set[70, 71], and the accuracy of the sampling can be systematically improved by including more points.

2.2.3 Pseudopotentials

An additional means by which to improve the efficiency (and accuracy) of a planewave-based DFT calculation is through the use of pseudopotentials[72]. Pseudopotentials are artificial or *ad hoc* potentials devised to simulate the combined effect of the ion nucleus and core electrons on the valence electrons. The basic idea involves removing the core electrons from the calculation and treating only the valence electrons explicitly. The core electrons and nuclear potential are replaced by a weaker pseudopotential that interacts with a set of modified valence wavefunctions, or "pseudowavefunctions," (pWF) which are nodeless and maximally smooth within some core radius, r_c. The pseudowavefunctions can now be expanded in a much smaller basis set of planewaves, saving a substantial amount of computer time. Some of the main advantages of using pseudopotentials include:

Fewer electrons Since the core electrons have been omitted from the simulation there are fewer wavefunctions to calculate.

Precision The total energy of a valence-only system is roughly 1000 times smaller than the energy of an all-electron system. Since the energy difference between different ionic and bonding configurations is caused almost totally by differences in the valence electrons, the precision required to determine energy differences in a pseudopotential calculation is much less than for the all-electron calculation.

Accuracy Because most properties of solids depend upon the valence electrons much more so than on the core electrons, by removing the core we lose very little by way of accuracy. In many classes of problems pseudopotential results are indistinguishable from all-electron results.

Fewer planewaves As alluded to above, the use of smooth pseudowavefunctions allows for a much smaller set of basis functions.

In earlier calculations it was customary to parameterize pseudopotentials by fitting to experimental data such as a bandstructure. These were known as empirical pseudopotentials, and should be distinguished from the *ab initio* pseudopotentials used in this and other modern DFT calculations. These modern potentials are developed through a parameter-free solution to the all-electron atomic problem, and are then used in a variety of different bonding environments. Some of the properties common to *ab initio* pseudopotentials include:

Non-locality The scattering properties of the pWF are constructed to be the same as those of the all-electron WF. The only difference being that the pWF is nodeless within the core region. Since the scattering from the ion core is different for each angular momentum l-value of the WF, the scattering from the pseudopotential must likewise be angular momentum dependent. Most modern pseudopotentials are

thus described as "non-local" in that they treat each l-value differently:

$$V_{\mathrm{NL}} = \sum_{lm} |Y_{lm}\rangle V_l \langle Y_{lm}|. \tag{2.17}$$

Here V_{NL} is the total pseudopotential, V_l is the pseudopotential for angular momentum l, and Y_{lm} are spherical harmonics.

Reproduction of eigenvalues and eigenfunctions The pWF ψ_l^{pv} should exactly equal the all electron WF ψ_l^{ae} for all r outside of a chosen core radius r_c, and the pseudoeigenvalue ϵ_l^{pv} should equal the all-electron value ϵ_l^{ae} when interacting with V_{NL}.

Norm conservation Since quantities like E_{xc} and E_{h} depend on both the spatial shape and magnitude of the valence charge density, the pseudovalence charge density must be equal in amount or normalized to the all-electron density:

$$\int_0^{r_c} r^2[|\psi_l^{ae}(r)|^2 - |\psi_l^{pv}(r)|^2]\, dr = 0. \tag{2.18}$$

In this way the core charge for both all-electron and pseudowavefunctions is the same, and since $\psi_l^{ae} = \psi_l^{pv}$ for $r \geq r_c$, the remaining charge is reproduced exactly.

Transferability and softness Pseudopotentials are constructed to be maximally smooth within r_c, yet should be transferable for use in a wide range of chemical environments (dimers, solids, surfaces, *etc.*). The choice of r_c determines the tradeoff in these two competing properties: small r_c values make for a very transferable pseudopotential with a large PW cutoff, and *vice versa*. The choice of which electrons be classified as "valence" and which as "core" also determines the transferability. For most elements beyond the first row, there is significant overlap between the core and valence charge densities, and a clear separation is not possible. This overlap can cause inaccuracies in the evaluation of the non-linear core-valence exchange-correlation energy, which should be treated via partial core corrections[73].

In the calculations presented herein we make use of the norm-conserving pseudopotentials described above, and an additional "ultrasoft" form proposed by Vanderbilt[74]. These ultrasoft pseudopotentials are most advantageous for the first row and transition metal elements, where the norm-conservation constraint (Eq. 2.18) results in "deep" pseudopotentials requiring large cutoff energies, $E_{textcut}$. Although it is possible to generate a softer potential by increasing the cutoff radius, this always results in a less transferable solution. Because of these difficulties, early calculations on first row and transition elements were problematic.

Vanderbilt's solution to this problem involved abandoning the norm-conservation constraint on the pseudowavefunction and introducing a set of atom-centered augmentation charges. Taken together, the sum of the pseudo-charge density and the augmentation charge density maintain the original charge distribution's size and shape (satisfying Eq. 2.18). Moreover, the pseudowavefunctions could now be constructed with a very large r_c, allowing for very small basis sets. In essence, this approach is similar to a mixed-basis where localized atomic orbitals are combined with planewaves. The accuracy of ultrasoft pseudopotentials has been found to be comparable to the best all-electron first-principles methods currently available.

More details regarding the pseudopotential implementation can be found in the following chapters and in Ref. [75].

2.2.4 Forces and Geometries: Hellman-Feynman Theorem

One of the goals of this study is to identify equilibrium interfacial structures. To do so requires the ability to calculate atomic forces and subsequently move the atoms such that these forces are minimized. Within a DFT calculation atomic forces and integrated stresses on the simulation cell can be obtained through use of the Hellmann-Feynman theorem[76, 77]. The theorem states that when the system is in its electronic ground state the partial derivative of the total energy with respect to the position of an ion gives the real physical force $\mathbf{f}_I$ on an ion:

$$\mathbf{f}_I = -\frac{\partial E^{\text{tot}}}{\partial \mathbf{R}_I}. \tag{2.19}$$

Expanding E^{tot} to reflect its dependence upon the KS wavefunctions,

$$\mathbf{f}_I = -\frac{\partial E^{\text{tot}}}{\partial \mathbf{R}_I} - \sum_{i=1}^{N} \frac{\partial E^{\text{tot}}}{\partial \psi_i} \frac{\partial \psi_i}{\partial \mathbf{R}_I} - \sum_{i=1}^{N} \frac{\partial E^{\text{tot}}}{\partial \psi_i^*} \frac{\partial \psi_i^*}{\partial \mathbf{R}_I} \tag{2.20}$$

it can be shown that the final two terms vanish for a system in its electronic ground state, once again yielding Eq. 2.19. When used in conjunction with a planewave basis set, atomic forces can be conveniently evaluated using an analytic expression[78]. The search for the ground state atomic configuration then proceeds in an iterative fashion, in which the electronic ground state is determined first, followed by the calculation of the atomic forces, and finally the atomic positions are adjusted in a direction consistent with those forces. The entire process is repeated until a minimum force configuration is obtained, usually through use of a conjugate-gradient[79] or other optimization algorithm.

2.2.5 Implementation: VASP

For this study we employ Density Functional Theory (DFT)[22, 23], as implemented in the Vienna *ab initio* Simulation Package (VASP)[80]. VASP uses a plane-wave basis set for the expansion of the single particle Kohn-Sham wavefunctions, and pseudopotentials[75, 81] to describe the computationally expensive electron-ion interaction. The ground state charge density and energy are calculated using a pre-conditioned conjugate gradient minimization algorithm[79, 82] coupled with a Pulay-like mixing scheme[83–85]. Sampling of the irreducible wedge of the Brillouin zone is performed with a regular Monkhorst-Pack grid of special $\mathbf{k}$-points[71]. Due to numerical instabilities associated with integrating the step-function character of the 0 K Fermi-Dirac distribution, partial occupancies of the single-particle wavefunctions are introduced[86, 87] with an energy level broadening of 0.1 eV. Ground state atomic geometries were obtained by minimizing the Hellman-Feynman forces[76, 77] using either a conjugate gradient[79] or quasi-Newton[83] algorithm. Finally, two separate approximations to the exchange-correlation energy were employed: the traditional Local Density Approximation (LDA) as parameterized by Perdew and Zunger[65], and the Generalized Gradient Approximation (GGA) of Perdew and Wang[88] (PW91).

Due to the substantial computational cost of performing a DFT calculation on supercells containing first row and transition metal elements, we emphasize that our molecular statics (0 K) predictions of structure and adhesion energies do not account for temperature and larger-scale size effects such as reconstructions and lattice mismatch. In order to minimize mismatch effects, we have intentionally selected ceramic compounds that are both technologically relevant and that have a relatively small mismatch (see Table 6.3) with the Al lattice. In addition, our model of VC is restricted to perfect 1:1 V:C stoichiometry (to permit the use of smaller supercells), even though the stoichiometry of realistic VC compounds is closer to $VC_{0.88}$[51].

2.3 Bonding Analysis

A major component of this study is the analysis of interfacial electronic structure, that is, we would like to classify the bond nature for each interface system. Unfortunately, this is not a straightforward task, as arriving at an understanding of bonding in the solid state can be difficult, even for homophase systems such as WC. Of course the situation is even more complicated at metal–ceramic interfaces, where media with vastly different electronic structures are adjoined. To handle this inherent complexity—and to address the fact that no single method can fully characterize atomic bonding—our analysis has relied upon several complimentary methods. In this section we give a brief overview of these tools, touching on some of their respective strengths and weaknesses.

2.3.1 Charge Density

Perhaps that quantity used most for bonding analysis is the total charge density, $n(\mathbf{r})$. In the context of a DFT-planewave calculation $n(\mathbf{r})$ is usually calculated on a grid according to Eq. 2.8, and is readily visualized as three-dimensional isosurfaces or two-dimensional contour slices. Although on its own $n(\mathbf{r})$ can provide valuable information, it is often difficult to work with in systems having very large variations in the magnitude of $n(\mathbf{r})$, where for example, the relatively small densities associated with a covalent bond might be obscured against the backdrop of larger atom-centered charge concentrations. For this reason a common way to utilize $n(\mathbf{r})$ is by forming a difference density $\Delta n(\mathbf{r})$ between the total charge and an appropriate reference system. (For example, in a crystal one could subtract the superposition of atomic charge densities from the crystal total density:

$$\Delta n(\mathbf{r}) = n(\mathbf{r}) - \sum_i n_i^{\text{atom}}(\mathbf{r}). \tag{2.21}$$

In an interface the isolated slab densities could be subtracted from the total interface density.) This difference charge then reveals the nature of charge *redistribution* upon forming the solid, interface, *etc*.: positive regions correspond to charge accumulation, negative regions correspond to charge depletion. In addition. the range of values in $\Delta n(\mathbf{r})$ is usually much smaller in magnitude than the total density. The only problems associated with using $\Delta n(\mathbf{r})$ arise when there are substantial atomic relaxations/rearrangements, for in this case it is difficult to choose the proper reference system to difference against. The charge density may be further analyzed by taking averages along certain directions, partitioning into Mulliken populations, or by incorporation into other schemes such as the Electron Localization Function (see below).

2.3.2 Density of States

A second tool commonly used to analyze bonding in extended structures is the density of states (DOS)[89]. A DOS plot is the analogue of a discrete energy level diagram for non-periodic systems such as molecules and clusters; the total DOS illustrates the number of electronic crystal orbital states $\psi_{n\mathbf{k}}(\mathbf{r})$ within an energy window $E + dE$. For the most part, the DOS is useful in determining the nature of covalent or metallic bonding involving the overlap or hybridization of states from different atoms. The DOS is often further decomposed into position-dependent (local DOS) or angular-momentum-dependent (partial DOS) contributions. The local DOS counts the number of states per unit energy within a region of space, and can be used to determine the spatial extent of bonding or other changes in the electronic structure due to the presence of surfaces, interfaces, *etc*. In the present study we will refer to the local DOS as projected onto selected atoms. In this case it is necessary to divide space into atom-centered Wigner-Seitz spheres of radius R_α, and all states within a given sphere are said to belong to the respective atom, α. The local DOS is thus defined as:

$$D(E, \mathbf{r}_\alpha) = \sum_{n\mathbf{k}} \int d\mathbf{r}\, \theta(R_\alpha - |\mathbf{r} - \mathbf{r}_\alpha|)\, \psi^*_{n\mathbf{k}}(\mathbf{r}) \psi_{n\mathbf{k}}(\mathbf{r}) f(E - E_{n\mathbf{k}}), \tag{2.22}$$

where $\mathbf{r}_\alpha$ is the location of atom α, $\theta(x)$ is the Heaviside function, and $f(E - E_{n\mathbf{k}})$ is the occupancy of the state with energy $En\mathbf{k}$. It should be noted that the results of a local DOS analysis depend upon the choice of R_α; for this reason it should be considered as a qualitative tool only. Within a local analysis, bonds between neighboring atoms appear as shared peaks with similar shapes and positioning in energy-space.

The local DOS can be further decomposed into the partial DOS by projecting the electronic states onto angular momentum eigenstates (spherical harmonics), Y_{lm}. In this way it is possible to determine the s, p, d, *etc*. nature of a given DOS peak/bond. While the DOS is useful in analyzing covalent/metallic bonding, its application to systems involving charge transfer is less straightforward. In theory, one can determine the charge on an atom by integrating the local DOS. In practice, the absolute value of the integration depends sensitively upon the projection radius R_α, and only qualitative comparisons are possible. A more natural approach to determining charge transfer (Mulliken populations) can be obtained by using a basis of atomic orbitals.

2.3.3 Mulliken Populations

For the purposes of evaluating Mulliken populations and Mayer bond orders (discussed below) it is desirable to use a basis of localized atomic-like orbitals rather than planewaves. For this reason some of our bonding analysis (especially those aspects pertaining to charge transfer effects) has been performed using the SIESTA package[90], wherein the electronic wavefunctions $\psi_i(\mathbf{r})$ are represented as:

$$\psi_i(\mathbf{r}) = \sum_{\mu=1}^{K} C_{\mu i} \phi_\mu(\mathbf{r}), \tag{2.23}$$

where the $C_{\mu i}$ are the expansion coefficients of state $\psi_i(\mathbf{r})$ in terms of pseudo-atomic orbitals $\phi_\mu(\mathbf{r})$ centered on the atoms. The net charge q_α (or Mulliken population) associated with a given atom α can then be expressed as[61]:

$$q_\alpha = Z_\alpha - \sum_{\mu \in \alpha} (\mathbf{PS})_{\mu\mu}, \tag{2.24}$$

where Z_α is the nuclear charge and the summation index runs over all basis functions μ centered on atom α. The density matrix $\mathbf{P}$ and overlap matrices $\mathbf{S}$ are defined as:

$$P_{\mu\nu} = \sum_i^K C_{\mu i} C^*_{\nu i} \tag{2.25}$$

$$S_{\mu\nu} = \int d\mathbf{r}\, \phi^*_\mu(\mathbf{r}) \phi_\nu(\mathbf{r}). \tag{2.26}$$

Although the choice of an atomic basis makes for a more realistic partitioning of atomic charges when compared to Wigner-Seitz spheres, the partitioning is still not unique; the relative values of the q_α are determined by the choice of basis. Nevertheless, it is still possible to use the Mulliken charges in a qualitative manner by comparing, for example, the charges on atoms at an interface with those at a surface or in the bulk.

2.3.4 Mayer Bond Orders

Just as a Mulliken population analysis attempts to quantify the amount of charge transfer, the Mayer bond order[91] likewise attempts to classify the nature and strength of bonding between atoms by assigning a numerical value to each bond. For an appropriate basis set, integral bond orders indicate the presence of single, double, *etc*. covalent bonds as in classical valence theory. Non-integral values indicate delocalized electrons (i.e., metallic bonding) or partial polar character (ionic bonding). Formally, the bond order B_{AB} between two atoms A and B is defined as:

$$B_{AB} = \sum_{\lambda \in A} \sum_{\omega \in B} (\mathbf{PS})_{\omega\lambda} (\mathbf{PS})_{\lambda\omega}, \tag{2.27}$$

where $\mathbf{P}$ and $\mathbf{S}$ are, respectively, the density and overlap matrices (Eqns. 2.25-2.26), and the summations are over all atomic orbitals λ on atom A, and all orbitals ω on atom B. Since B_{AB} is also dependent upon the choice of basis, it is in practice not possible to use the absolute magnitude of the bond order to classify bonding as being either ionic, covalent, metallic, *etc*. A more sensible approach is to instead draw comparisons between bond orders of related structures. The bond order is therefore more of a qualitative tool to be used in a manner similar to that of the Mulliken populations. Our bond order calculations were performed using the SIESTA package, which we modified for this purpose.

2.3.5 Electron Localization Function

The final tool used in our bonding analysis is the Electron Localization Function (ELF)[92–94], which has recently become very popular in the field of quantum chemistry. The ELF is a scalar quantity ranging from zero to one that identifies regions of space where electrons are well localized, as one would find in a bonded pair or lone pair. In a many-electron system the ELF is approximately one where electrons are paired in a covalent bond or in a lone pair; it is also nearly unity for regions near the unpaired lone electron of a dangling bond. The ELF is small in low density regions and assumes a value of about 0.5 in regions characterized by metallic bonding.

As a result of the Pauli exclusion principle, the kinetic energy density of a system of fermions must be greater than or equal to that of a system of bosons with the same density. Savin *et al*.[92] used this fact to interpret the ELF as a measure of the extra contribution to the kinetic energy due to Pauli exclusion: Large values of the ELF indicate regions of strongly paired electrons having a local bosonic character. More formally, the ELF is defined as:

$$ELF = \frac{1}{1 + [D(\mathbf{r})/D_{\mathrm{h}}(\mathbf{r})]^2}, \tag{2.28}$$

where $D(\mathbf{r})$ is the Pauli excess kinetic energy density, which is the difference between the kinetic energy density of the Kohn-Sham system of electrons and that of a system of non-interacting bosons of the same density. Finally, D_{h} is the kinetic energy density of a homogeneous electron gas with the same local density. By plotting the ELF and analyzing its shape and magnitude, one can easily identify regions of ionic, covalent, and metallic bonding.

Chapter 3

The Al(111)/α–Al_2O_3(0001) Interface

3.1 Introduction

One important metal–ceramic interface is that between Aluminum and its native oxide, Al_2O_3. Aluminum is one of the world's most widely used metals, in large part due to its superior strength-to-weight ratio, but also because of the favorable protective properties afforded by its oxide layer. This layer is predominantly amorphous[95], with a thickness ranging from 3-6 nm, and consists of AlO_4 tetrahedra with a small number of AlO_6 octahedra[96]. (In addition, its composition can be strongly affected by the concentration of alloying agents that have diffused from the bulk. Transition aluminas, such as γ–Al_2O_3, may also be present in addition to hydroxylated structures such as pseudoboehmite[97]). The oxide can be created by direct oxidation of Al metal with O_2 at high temperatures—a process which proceeds rapidly and is highly exothermic[97]. Because of the difficulties associated with modeling an amorphous oxide/metal interface, for this study we have made a simplifying approximation by substituting the amorphous oxide with its thermodynamically stable phase, α–Al_2O_3. We believe this model system still embodies much of the essential physics of the true Al/Al_2O_3 interface. Despite its importance, there have been surprisingly few theoretical studies of the atomic and electronic structure of this system, with only one *ab initio* calculation[47] appearing during the preparation of this manuscript.

To our knowledge, the first theoretical study of atomic-scale adhesion at the Al/α–Al_2O_3 interface was performed by Anderson and co-workers[98]. They utilized a semi-empirical molecular orbital method based on cluster models to study cation vacancy diffusion in alumina and the adherence of alumina to Ni, Al, and Yt surfaces for one particular interface geometry. They reported an adhesion energy of 4.8 eV for the interface between a 10-atom Al cluster and an $[AlO_6]^{6-}$ cluster, and found that the presence of Yt at the interface at monolayer coverage greatly strengthened the bond between metal and oxide. Unfortunately, the influence of lattice relaxation was not examined; more recent studies[45, 46] of metal adsorption and adhesion on alumina surfaces have shown these effects to be significant. Streitz and Mintmire[99, 100] developed an electrostatic model (ES+) for alumina taking into account charge transfer between the cations and anions, and merged it with an Embedded Atom Method (EAM) potential for metallic Al to study adhesion and adhesive failure at the Al/alumina interface. By equilibrating the interface at 100 K for 1-2 ps, they found that O atoms rapidly diffused into the Al, resulting in a relatively weak interface with a highly disordered

interphase region. Subsequent application of a tensile stress to the system resulted in fracture under a maximum stress of 2 GPa with $\mathcal{W}_{\rm ad} \simeq 0.3$ J/m^2. Angelo and Baskes[101] used the modified EAM to perform molecular dynamics simulations of the relative energetics of (111) oriented Al islands on the basal plane of alumina. (The adhesion energy was not reported.) They found that the orientation with $[1\bar{1}0]_{\rm Al} \parallel [10\bar{1}0]_{\rm Al_2O_3}$ gave the most stable structure, in good agreement with experiment[102], and noted a significant increase in interlayer separation for the first two layers of the Al island relative to that of the bulk. It was suggested that this would weaken the interface, with fracture occurring within the metal. Finally, Lipkin *et al.*[21] have recently developed an analytical expression for estimating the van der Waals contribution to the adhesion energy at metal–ceramic interfaces. They were able to obtain a lower-bound estimate of the measured adhesion energies for Al/alumina and several other non-reactive metal/alumina systems, and found that adhesion involving Cu, Au, and Ag was well accounted for by dipole-dipole interactions alone.

Experimentally, two groups have reported heteroepitaxial growth of Al films on an α–Al_2O_3 substrate in ultra-high vacuum (UHV)[102–104]. At room temperature, Vermeersch and co-workers[103] found that for Al coverages of less than 5 monolayers, the Al film reacted with the alumina surface giving rise to an Al suboxide layer with a $(\sqrt{31}\times\sqrt{31})R\pm 9^\circ$ geometry. Further deposition resulted in clustering of the Al atoms followed by island growth. Deposition at 470°C[104] was characterized by the same suboxide formation for low coverages, followed by epitaxial growth with an orientation of $[\bar{2}11](111)_{\rm Al} \parallel \langle\bar{2}110\rangle(0001)_{\rm Al_2O_3}$. In a more recent experiment, Medlin[102] *et al.* found three distinct grain orientations of the Al film relative to the substrate, with the primary orientation being $[\bar{1}10](111)_{\rm Al} \parallel [10\bar{1}0](0001)_{\rm Al_2O_3}$ for growth at 200°C. High resolution transmission electron microscopy revealed an interface that was atomically sharp to within a few atomic layers, while atomic force microscopy of the surface morphology revealed large planar terraces characteristic of step-flow growth. We have adopted Medlin's orientation relationship in our calculations.

There has been a large body of work devoted to understanding the surface properties of α–Al_2O_3. These studies range from investigations of the clean and hydrogenated surfaces[105–113], to the adsorption properties of metal overlayers[1, 46, 114–117], water[118–120], and organo-phosphorous acids[121]. Electrostatic considerations[122] as well as a number of experimental and theoretical studies suggest that the bulk crystal structure with a single terminating layer of Al yields the most stable *clean* (0001) surface. However, this issue is still a matter of debate, as Toofan and Watson[108] have reported a mixture of 2:1 O/Al–terminated surface domains using a tensor LEED analysis in UHV. Moreover, a recent crystal truncation rod diffraction study[119] performed under ambient conditions has shown that the hydrated surface is O–terminated with a semi-ordered layer of adsorbed water about 2.3Å above the terminal oxygen layer. In practice, it has proven very difficult to create a clean surface due to the presence of Hydrogen, even in UHV[106, 116]. Therefore, one should be cautious in making direct comparisons between theoretical studies of clean surfaces/interfaces and experiments that may by H–contaminated. As a first step towards simulating a more realistic fully hydrated interface, we have neglected the influence of Hydrogen in this work and have focused instead only on clean surfaces/interfaces with either Al– or O–terminations. We have chosen to include O–terminated surfaces in our interfacial study in order to draw comparisons with the Al–terminated case and as a precursor to follow-up studies that will include the effects of adsorbed Hydrogen and/or water. Furthermore, a recent study by Zhang and Smith[47] has shown that both terminations are possible, depending upon the

partial pressure of O_2 gas. There is also experimental evidence that other alumina/metal interfaces, such as alumina/Nb, are O–terminated[123].

In addition to determining adhesion energies, the goal of this study is to systematically analyze the atomic and electronic structure of the Al/α–Al_2O_3 interface. Since quantities such as $\mathcal{W}_{\rm ad}$ are intimately related to the interfacial atomic structure and bonding, an understanding of these issues is a prerequisite to formulation of a general theory of adhesion. First of all, in order to identify the energetically preferred structure, we have studied six candidate interface geometries, including two distinct terminations of the oxide, and have allowed for full relaxation of all atomic coordinates. The optimal geometries are rationalized in terms of the bulk stacking sequence of the oxide. The second goal of this work is to illuminate the nature of the interface bonds through the application of several complementary analytical tools. This is necessary because the vastly different chemical environments within the constituent slabs make for a wide variety of possible interface bonds, ranging from highly delocalized (as in the Al), to highly ionic (as in the oxide). Unfortunately, no one method can completely classify the bonding, and we will demonstrate how the application of an ensemble of techniques is preferable. It will be shown that the ability of the metal to transfer charge to the oxide—and thereby form ionic bonds—is key to predicting the magnitude of $\mathcal{W}_{\rm ad}$.

The remainder of this chapter is organized as follows: Section 3.2 presents the results of our bulk and surface validation calculations on the pure materials. Section 3.3 describes the six different interfacial geometries used in our simulations, and Section 3.4 outlines the methods used to calculate the lowest energy structures and their corresponding adhesion energies. The results for the structure, adhesion, and bond character for the Al–terminated and O–terminated interfaces appear in Sections 3.5 and 3.6, respectively. Finally, we summarize our findings in Section 3.7.

3.2 Bulk and Surface Calculations

3.2.1 Bulk Properties

The first step in any first principles study is to verify the accuracy of the chosen method(s). This is accomplished by calculating the bulk properties of the materials in question and comparing with experimental and other theoretical results. The degree to which the calculated values agree with experiment can then be used to validate the methodology and to place error bars on later results. To these ends, we present a series of calculations on bulk Al and α-Al_2O_3 in the sections that follow.

Aluminum

Our calculations on bulk Aluminum were performed using a norm conserving Rappe, Rabe, Kaxiras, Joannopoulos-type (RRKJ)[81] pseudopotential in the separable Kleinman-Bylander[124] form. The d function was chosen as the local component, and the cutoff radius for matching of the all-electron and pseudo-wavefunctions was set at 0.96 Å. Additionally, we have taken into account the nonlinear core-valence exchange-correlation interaction by including partial core corrections. The total energy per bulk atom was converged to within 1-2 meV upon using a planewave kinetic energy cutoff of 270 eV. The same

degree of convergence in $\mathbf{k}$-point sampling was attained using a Monkhorst-Pack grid of 110 $\mathbf{k}$-points in the irreducible wedge of the Brillouin zone (IBZ).

To estimate the ground state lattice constant, a, bulk modulus, B_0, and cohesive energy, $\mathrm{E_{coh}}$, a series of two energy vs. volume calculations was performed, with the results fit to the Murnaghan[139] equation of state (see Fig. 3.1):

$$E(V) = \frac{B_0 V}{B_0'(B_0'-1)}\left[B_0'\left(1-\frac{V_0}{V}\right)+\left(\frac{V_0}{V}\right)^{B_0'}-1\right]+E_0(V_0). \tag{3.1}$$

In the first set of calculations the equation of state was fit to a relatively wide range of volume data (denoted as the "full range fit" in Fig. 3.1), spanning -24% to +20% of the equilibrium experimental volume. The second set ("limited range fit") uses a smaller volume range of about -7% to +8%.

The cohesive energy calculations are performed by subtracting the total energy of the spin polarized Al atom from the energy per atom in the bulk. Our results for both the LDA and GGA are summarized in Table 3.1 and compared with other recent calculations and experimental data. All experimental data reported from Refs. [128], [129] and [69] are taken at 0 K. We find that the GGA does substantially improve the well-known LDA errors in lattice constant and cohesive energy (the so-called "overbinding" effect), yet it underestimates the bulk modulus with respect to the experimental values[129–131], regardless of which volume set is used. Of the two volume sets, fitting to the smaller volume range results in a slightly larger bulk modulus for both functionals, thereby shifting the GGA value closer to experiment, while pushing the LDA result further from it. The lattice constant and cohesive energy are not dependent upon the volume range. Table 3.1 also shows that all the gradient-corrected (GC) functionals systematically underestimate the bulk modulus, with the PBE[140] functional giving somewhat better agreement with experiment than PW91. Overall, we find that our calculated values are in excellent agreement with the other first-principles results. However, since neither the GC nor local-density functionals gives convincingly superior agreement with experiment, we have chosen to use both for the remainder of this work.

α–$\mathbf{Al_2O_3}$

The structure of alumina has been studied extensively using both theoretical and experimental methods (see Ref. [141] and references therein). Here we briefly review its structure and compare our calculated bulk properties to experiment and other recent calculations.

The crystal structure of alumina consists of a hexagonal close packed array of oxygen atoms with Al atoms occupying two thirds of the interstitial octahedral sites[142]. The structure can be viewed in either its primitive rhombohedral cell containing two molecular units (for a total of 10 atoms), with $D_{3d}^6(R\bar{3}c)$ symmetry, or in the more traditional hexagonal unit cell containing 6 molecular units. The location of the atoms within the primitive cell are specified by two internal coordinates: u, which gives the location of one of the Al atoms along this cell's long axis in terms of the hexagonal c lattice parameter, and v, which is the distance from the c axis to any of the O atoms in units of the basal plane hexagonal lattice parameter, a.

We have calculated the bulk properties of alumina using a planewave cutoff energy of 400 eV and 6

System	Method/XC	a (Å)	c (Å)	u	v	B_0 (GPa)	E_{coh} (eV)
Al	present/LDA	3.971				81.4[a], 84.1[b]	4.09
	LAPW/LDA[c]	3.978				83.9	
	PW/LDA[d]	3.97				82	4.05
	present/PW91	4.039				71.9[a], 73.5[b]	3.54
	PW/PW91[e]	4.03				72	3.51
	LAPW/PW91[c]	4.094				72.6	
	PW/PW91[d]	4.05				75	3.46
	PW/PBE[d]	4.05				77	3.51
	Experiment	4.03[f]					
	Experiment[g]					79.4, 82.0	
	Experiment						3.39[h]
$\alpha-Al_2O_3$	present/LDA	4.715	12.861	0.352	0.306	254[a], 239[b]	37.1
	present/PW91	4.792	13.077	0.352	0.306	231[a], 246[b]	33.0
	OLCAO/LDA[i]	4.833	12.611	0.355	0.312	242	
	AE-LCGTO/LDA[j]	4.767	12.969	0.352	0.306	243.8	36.5
	Experiment[k]	4.758	13.00	0.352	0.306		
	Experiment[l]	4.763	12.98	0.352	0.306		
	Experiment[m]					253 ± 1	
	Experiment[n]						31.8

[a] Full range volume fit.
[b] Limited range volume fit.
[c] Ref. [125]
[d] Ref. [126]
[e] Ref. [127]
[f] Ref. [128]
[g] Refs. [129–131]
[h] Ref. [69]
[i] Ref. [132]
[j] Ref. [133]
[k] Refs. [134, 135]
[l] Refs. [135, 136]
[m] Ref. [137]
[n] Ref. [138]

Table 3.1: Calculated bulk properties for Al and α–Al_2O_3 and comparison with other recent calculations and experimental data. "Present" refers to the current calculations, "PW" refers to a planewave pseudopotential calculation, "AE-LCGTO" refers to an all-electron linear combination of Gaussian-type orbitals method, "OLCAO" to the orthogonalized linear combination of atomic orbitals method, and "LAPW" to the linearized augmented plane wave method.

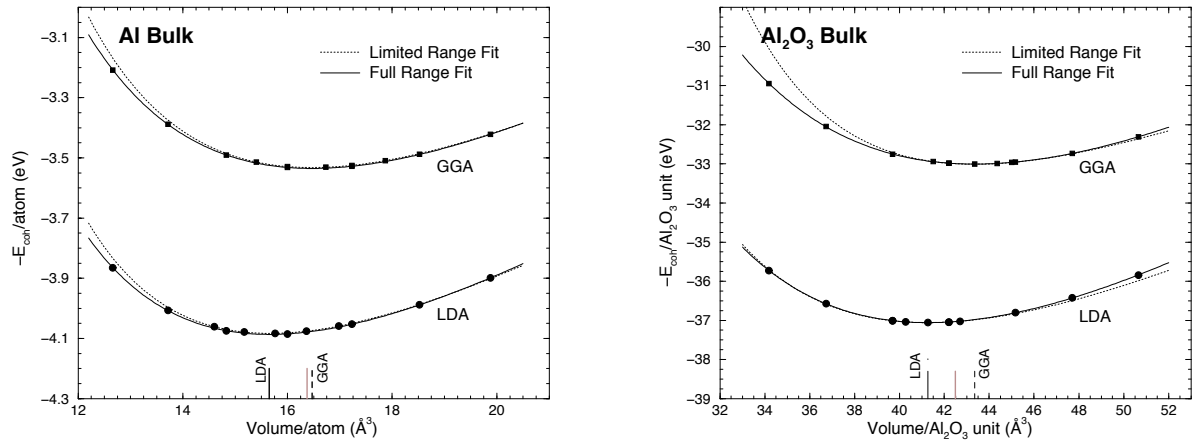

Figure 3.1: Cohesive energy vs. volume for bulk Al and alumina as calculated within the LDA and GGA. For each data set, two separate fits to the *ab initio* data were performed. The solid lines are fit to a wider range of volume data ("full range fit"), while the dotted lines are fit to a restricted data set centered about the experimental volume ("limited range fit"). The vertical bars along the plot abscissa give the location of the calculated equilibrium volumes with respect to the experimental volume (indicated by a grey bar), extrapolated to 100 K in the case of alumina, and 0 K for Al.

$\mathbf{k}$-points in the IBZ. These values resulted in convergence in the total energy to within 1-2 meV per atom. We use the same norm-conserving pseudopotential for the Al atoms as used for bulk Al, and an ultrasoft pseudopotential for O with an outer cutoff radius of 0.82 Å.[1] The results of the Murnaghan fit for both LDA and GGA calculations are shown in Fig. 3.1 and Table 3.1, and exhibit good agreement with experiment and other first principles calculations. Again, we have performed fits to two ranges of volume data: the limited range fit spans -4% to +4% of the experimental volume, whereas the full range fit includes volumes ranging from -20% to +19% (see Fig. 3.1). As was the case for Al, our GGA calculations give slightly better agreement with the experimental data for the lattice constants (LDA: underestimated 0.97%, GGA: overestimated 0.67%) and cohesive energy. The two values for the experimental lattice constants at 100 K were obtained by applying thermal expansion data from Ref. [135] to the room temperature data of Refs. [134] and [136], as done in Ref. [141]. The zero-pressure bulk modulus predicted by the GGA full range fit (231 GPa) underestimates the experimental[2] value by 8.5%, and better agreement is obtained upon fitting to the limited range volume data (246 GPa). Conversely, for the LDA, the near perfect agreement (254 GPa) with the experimental B_0 obtained with the full range fit degrades upon fitting to the limited range volume data (239 GPa). Both volume sets give essentially identical values for the lattice constants and cohesive

[1] Specifically, these are the "Al_h" and standard "O" pseudopotentials (pp) from the VASP pp database. We also performed some calculations on alumina using ultrasoft pp's for *both* Al and O. These pp's have an undesirable core overlap of nearly 0.4 Å when used in the close confines of the alumina crystal. For this set, we found that the LDA lattice constants were in better agreement with experiment than those given by GGA, however, the LDA bulk modulus was worse (LDA: $a = 4.75, c = 12.94, B_0 = 240$. GGA: $a = 4.82, c = 13.16, B_0 = 234$). Although for the bulk these differences are minor, we found that use of ultrasoft pp's for both elements had a significant effect upon our adhesion energies, changing some values by as much as 25%.

[2] The experimental value is based on an analysis by Richet *et al.*[137] of 16 experimental and theoretical values, from which it was determined that the "best" value was 253 ± 1 GPa.

System	# Layers	σ(LDA)	σ(GGA)
Al	3	0.97	0.76
	5	1.02	0.81
	7	1.02	0.81
	9	1.00	0.80
	11	1.02	0.82
$\alpha-Al_2O_3$	9	2.02	1.50
	15	2.12	1.59
	21	2.12	1.59
	27	2.12	1.59

Table 3.2: Surface energy σ vs. slab thickness for Al(111) and α–Al_2O_3(0001). Units are J/m^2.

energy. An important point of validation is the good agreement with the available *all electron* calculations recently reported by Boettger[141]. This suggests that use of the pseudopotential approximation—often of questionable validity for highly ionic systems—is indeed valid here.

In summary, we have shown that the present methods are generally in good agreement with the existing experimental data and other first principles calculations. We find that neither the LDA nor the GGA gives convincingly superior agreement with experiment, therefore our remaining calculations will utilize both functionals.

3.2.2 Surface Properties

Since the ultimate goal of this work is to simulate the structure, energetics, and bonding at a *bulk-like* interface between Al and alumina, it is essential that the slabs used in forming the interface be sufficiently thick so as to exhibit bulk-like interiors. This is necessary to avoid simulating the adhesion properties of a thin film, which can be very different from that of the bulk. One way to test for the presence of a bulk-like interior is to check for convergence of the slab's surface energy as a function of slab thickness (i.e., the number of atomic layers comprising the slab). Equivalently, one can check to see that the incremental change in total energy upon increasing the slab thicknesses has converged to a value close to what is found in the bulk.

A second consideration is surface structure. It is well known that the Al–terminated (0001) surface of alumina undergoes an extensive relaxation that extends several layers into the bulk[46]. In order to predict accurate interface structures with this material, it might be argued that an additional series of surface calculations is needed to insure that the relaxations of at least the first few atomic layers are converged with respect to slab thickness. We find that the convergence of the first few interlayer relaxations follows the convergence of the surface energy .

Al(111)

Experimentally, the Al(111) plane has been found to be the preferred interfacial plane for epitaxial growth of Al on α–Al_2O_3(0001)[102, 104]. Additionally, since Al has the FCC crystal structure, the (111) surface

System	Method/XC	σ
Al	present/LDA	1.02
	PW/LDA[143]	0.94
	present/PW91	0.82
	LMTO/PW91[144]	1.20
	Experiment[145, 146]	0.81
$\alpha-Al_2O_3$	present/LDA	2.12
	PW/LDA[109]	1.76
	PW/LDA[112]	1.98
	PW/LDA[110]	1.94
	MB/LDA[111]	2.13
	present/PW91	1.59
	PW/PW91[110]	1.59
	LAPW/PW91[113]	2.13
	PW/BLYP[45]	1.95
	PW/BLYP[118]	1.89

Table 3.3: Comparison of our calculated surface energies with other recent calculations and experiment (where available). The acronyms describing the methods used are the same as in Table 3.1, with "MB" referring to the mixed basis method, and "LMTO" referring to the linearized muffin tin orbital method. Units are J/m^2.

is the most densely packed surface and therefore should exhibit the lowest surface energy. Our Al(111) surface simulation cell has hexagonal geometry with one atom per layer, and the in-plane lattice vectors are consistent with the bulk lattice parameters as discussed in the preceding section (2.81 Å for LDA, and 2.86 Å for GGA). In order to prevent unwanted interactions between the slab and its periodic images, a vacuum region must also be included in the cell; our convergence tests find that a 10 Å region is sufficient to converge the total energy of a 5-layer slab to within 1-2 meV per atom. The same 1-2 meV degree of energy convergence with respect to $\mathbf{k}$-point sampling was attained upon using 33 $\mathbf{k}$-points ($16 \times 16 \times 1$, Γ-centered grid) in the irreducible wedge of the Brillouin zone. The positions of all atoms in the slabs were optimized according to a conjugate gradient minimization of the Hellman-Feynman[76, 77] forces until the magnitude of the force on each atom was 0.03 eV/Å or less.

In order to determine the minimum thickness necessary for a bulk-like Al slab, we have calculated the surface energy for slabs ranging from three up to eleven atomic layers (Table 3.2) using the method proposed by Boettger and others[133, 147]. We find that the surface energy is well converged by a five-layer-thick slab—thereby indicating a bulk-like interior—which is in good agreement with other studies of the effect of Al(111) substrate thickness on the adsorption energies of Na and K[148]. Table 3.3 compares our converged surface energies with those from other recent first-principles calculations and with experiment. We note that while our LDA value is in relatively good agreement with the other LDA value reported in Ref. [143], our GGA value differs from that found in Ref. [144] even though the same GGA functional was used. Nevertheless, our GGA value is in better agreement with the available experimental data,[3] which suggests

[3]The 0 K "average" surface energy of Al is 1.2[145] J/m^2, which, using an argument based on atomic packing[146], gives a value of 0.81 J/m^2 for the (111) surface.

	Theory							Experiment	
	Present (# Layers)					Other			
Interlayer	3	5	7	9	11	[143]	[149]	[150]	[151]
1-2	-0.77	+1.92	+1.32	+0.61	+1.05	+1.18	+0.83	+0.9±0.5	+1.7±0.3
2-3		+0.42	-0.07	-0.46	-0.46	-0.40	-0.15		+0.5±0.7
3-4			-0.03	+0.11	+0.45	+0.22	+0.61		
4-5				-0.01	+0.25		+0.58		
5-6					-0.41				

Table 3.4: LDA Interlayer relaxations of the Al(111) surface as a function of slab thickness, given as a percentage of the bulk spacings.

		Theory									Experiment		
		Present (# Layers)				Other							
Interlayer		9	15	21	27	[113]	[109]	[46]	[112]	[118]	[106]	[107]	[108]
Al-O_3	1-2	-94	-83	-84	-83	-86	-86	-87	-85	-82	-63	-51	+30
O_3-Al	2-3	+2	+3	+3	+3	+6	+3	+3	+3	+7		+16	+6
Al-Al	3-4	-53	-46	-45	-46	-49	-54	-42	-45	-52		-29	-55
Al-O_3	4-5	+24	+19	+19	+19	+22	+25	+19	+20	+25		+20	
O_3-Al	5-6		+4	+4	+4	+6		+6					

Table 3.5: LDA Interlayer relaxations of the Al-terminated α–Al_2O_3(0001) surface as a function of slab thickness, given as a percentage of the bulk spacings.

that either our approach is more reliable than the LMTO method for calculating surface energies, or that non-convergence effects[133] might be to blame.

Since we intend to accurately predict the atomic structure of the Al/α–Al_2O_3 interface, we have examined the relaxations of the Al(111) surface in order to insure that they are reasonably converged as a function of slab thickness (Table 3.4). Contrary to the large relaxations present in α–Al_2O_3(0001), the (111) surface of Al exhibits a very small degree of interlayer relaxation, as one would expect of the close-packed face of an FCC metal. (The magnitude of all relaxations are less than 2% of the bulk spacing.) Our calculations show that the sign of the first layer relaxation is only given correctly for slabs which are at least five atomic layers thick, and is in good agreement with the other theoretical and experimental values. Although the sign of the second interlayer relaxation does not converge until slabs of seven layers are used, the absolute size of these relaxations is very small, on the order of 0.01Å. Thus, given that the surface energy of the slab is converged at five layers, and our belief that the increase in structural accuracy achieved by using a seven layer slab is not justified by the accompanying increase in computational cost, we feel that a five layer Al slab is sufficient for the remainder of our investigation.

α–Al_2O_3(0001)

As was done for the Al(111) surface, a series of surface energy and surface relaxation calculations was carried out on the α–Al_2O_3(0001) Al–terminated surface to determine the minimum number of atomic layers necessary for a bulk-like slab. Convergence tests showed that use of 4 $\mathbf{k}$-points in the IBZ and a

vacuum region of 10Å yielded converged total energies to within 1-2 meV per atom. All atoms were relaxed to their ground state positions by minimizing the magnitude of the Hellman-Feynman forces to a tolerance of 0.05 eV/Å/atom or less.

Table 3.2 gives the calculated LDA and GGA surface energies for alumina as a function of slab thickness for slabs ranging from 9 up to 27 atomic layers (corresponding to 3 and 9 molecular units, respectively). Once again we have used the method of Ref. [133] in order to avoid the problem of nonconvergence for thicker slabs. As can be seen in the table, very good convergence is attained upon using slabs which are 15 or more layers thick. To put our values in context, we report other first-principles estimates of this surface energy from the literature in Table 3.3. Focusing first on the LDA calculations, we can see that, with the exception of Ref. [109]—which only allowed for vertical relaxations of the atomic layers—all of the predicted values agree to within 10%. However, the agreement between the GGA values is somewhat worse. Our value of 1.59 J/m^2 is identical to the pseudopotential calculation reported in Ref. [110], but quite different from the LAPW result from Ref. [113], even though all three calculations used the same GGA functional. One possible explanation for this difference might be due to the nonconvergence problem mentioned above: both our calculation and that of Ref. [110] corrected for this error, but the details of the surface energy calculation in Ref. [113] were not reported.[4] The two remaining GGA calculations used the BLYP functional, and give values which fall roughly between the pseudopotential and LAPW values. Reference [118] used a 9 layer slab, which we believe is too thin to yield a converged surface energy, and it is not known whether Ref. [45] corrected for errors due to nonconvergence. Unfortunately, due to the difficulties in preparing a clean surface of α–Al_2O_3, there are currently no *uncontaminated* experimental data which could be used to resolve these differences.[5]

Table 3.5 lists our calculated LDA interlayer relaxations of Al–terminated α–Al_2O_3 (0001) surfaces of varying thickness for the first five interlayers.[6] As was the case for the surface energy, we find that these relaxations are well converged for slabs containing 15 or more atomic layers, and are in excellent agreement with the other first-principles results. The notable differences in magnitude and direction of relaxations predicted by theory with those from experiment have recently been explained by the presence of Hydrogen and/or hydroxyl groups on the surface. Hass and co-workers[118] showed that the presence of both molecular and dissociated water resulted in an outward movement of the terminating Al layer, thereby improving agreement with two recent experiments[106, 107]. Wang and co-workers[113] have also shown that for an O–terminated surface the presence of Hydrogen leads to an expansion of the terminal layer, in close agreement with experimental work reported by Toofan *et al*[108].

In conclusion, we have shown that our calculated values of the bulk and surface properties for both Al and α–Al_2O_3 are in very good agreement with available experimental and other first-principles results, thereby validating the application of this methodology to the study of interfacial properties.

[4]The problem of nonconvergence might not be a satisfactory explanation for these discrepancies, especially considering that the good agreement of the LDA values (most of which did not correct for this) indicates an insensitivity to this problem. Further study of the disagreement in the GGA values is needed.

[5]Weirauch and Ownby[152] have reported a surface energy of 1.63 J/m^2 for the (0001) surface of α–Al_2O_3at 1073 K. In their study, no attempt was made to remove Hydrogen or other adsorbed species from the substrate.

[6]We also calculated these relaxations within the GGA and found that they are essentially identical to the LDA values.

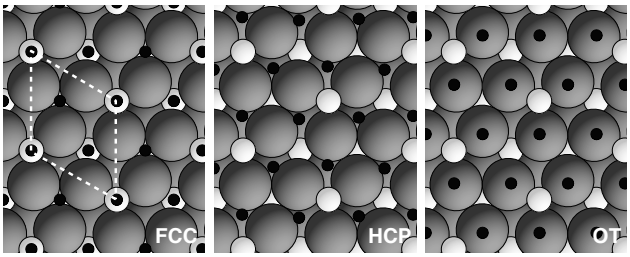

Figure 3.2: Depiction of the three distinct interfacial stacking sequences. Large grey spheres represent O atoms, small white spheres represent Al atoms (also from the oxide slab), and black circles indicate the position of the interfacial layer of the Al(111) slab. The remaining four layers of the Al slab are omitted for clarity. The monikers "FCC," "HCP," and "OT," indicate the location of the oxide slab's interfacial oxygen layer with respect to the stacking sequence of the Al(111) surface. The dotted white parallelogram gives the outline of the simulation cell looking along the $[000\bar{1}]$ direction.

3.3 Interface Geometry

Generally speaking, there are an infinite number of ways two surfaces can be joined to form an interface: the surfaces can be created by cleaving along one of many possible planes, when dealing with compounds one has to choose amongst several surface stoichiometries, and finally there is a continuum of relative rotational and translational orientations. However, cystallographic considerations indicate that for an HCP crystal interfaced to an FCC crystal, the preferred orientation relationship is given by: $(0001)_{\mathrm{HCP}} \parallel (111)_{\mathrm{FCC}}$ and $[10\bar{1}0]_{\mathrm{HCP}} \parallel [\bar{1}10]_{\mathrm{FCC}}$, in which the close-packed planes and directions are matched across the interface. This is the same orientation relationship found by Medlin *et al*.[102] for Al films grown epitaxially on a sapphire substrate (see also Ref. [104]). Unfortunately, in that study it was possible to determine neither the chemical composition of the oxide's terminating layer nor the stacking sequence of the interfacial metal atoms relative to those of the oxide. In this work we have adopted the orientation relationship reported by Medlin, and have endeavored to determine the remaining unknown variables governing the structure of the interface. To these ends, we have considered three different stacking sequences and two different oxide terminations, for a total of six candidate interfacial geometries. The stacking sequences differ in the location of the oxide's interfacial O-layer with respect to the stacking sequence of the Al (111) surface, and are illustrated in Figure 3.2. Using the nomenclature of that figure: the "FCC" stacking places the metal slab's interfacial atoms above the cation sites in the oxide, in the "HCP" stacking the metal atoms sit above the oxide's second O layer, and in the "OT" stacking the metal atoms sit directly above the surface O atoms. The oxide was chosen to be terminated by either a monolayer of Al (as discussed in the previous section), or a monolayer of O. For each of these candidate geometries final interfacial structures were obtained by minimization of the Hellman-Feynman forces for all atomic coordinates.

Based on the results of our convergence tests for the individual surfaces, our model utilizes a 15 layer slab of α–Al_2O_3 (0001) arranged in a multilayer geometry between two 5 layer slabs of Al(111). There is a 10Å vacuum region separating the free surfaces at the back of the Al slabs. This symmetric arrangement eliminates effects of spurious dipole interactions which might bias the results[148]. Each layer of the Al slab contains three atoms, and care has been taken to insure that the two interfaces are identical. There are a total

of 55 atoms in the supercells containing the Al–terminated interfaces, and 53 atoms in the O–terminated models.

Based on differences in the in-plane lattice translation vectors of $\frac{2a}{3}[10\bar{1}0]_{Al_2O_3}$= 2.74Å and $a[\bar{1}10]_{Al}$= 2.86Å, the experiments presented in Ref. [102] calculated the lattice misfit of the interface to be 4.3%. The interface was observed to be semi-coherent, in that the metal film was not found to be pseudomorphically strained through the film thickness to match the in-plane dimensions of the substrate. A misfit of this size suggests that close to the interface there are likely to be large regions of coherency—in which the metal film is strained to match the dimensions of the substrate—separated by a widely-spaced periodic array of misfit dislocations. Since performing calculations on a supercell that accommodates the dislocation structure is impractical for a misfit of this size, our calculations use the coherent interface approximation, in which the softer Al slabs are strained to match the dimensions of the unreconstructed (1×1) α–Al_2O_3 (0001) surface unit cell. As our interface simulations use the bulk LDA lattice constants, the 3.1% misfit in our system is somewhat smaller than that which is found in experiment.[7] In practice, we are simulating the regions between dislocations. Even though our estimates of bond nature, atomic structure, and adhesion energy will be accurate for these regions, our estimate of the global adhesion energy will be approximate in the sense that it neglects misfit effects. For further discussion of misfit effects in adhesion energy calculations see Ref. [153].

3.4 Computational Procedure

We have used two different methods to estimate the ideal work of separation, Eq. 1.4. The first method is based on the Universal Binding Energy Relation (UBER):[32]

$$\mathcal{W}_{ad}(d) = -\mathcal{W}^0_{ad}\left(1 + \frac{d - d_0}{l}\right)\exp\left(-\frac{d - d_0}{l}\right) \tag{3.2}$$

where $\mathcal{W}^0_{ad}$ and d_0 are the equilibrium adhesive energy per unit surface area and equilibrium interfacial separation, respectively, and l is a scaling length. In this method, the unrelaxed slabs are brought incrementally closer together starting from a large initial separation, and at each interface separation the total energy is calculated. The procedure continues until the energy passes through a minimum at the equilibrium interfacial separation, and then begins to rise again at subsequently shorter distances. Finally, the energy vs. distance data is fit to the UBER, yielding both the ideal work of separation and equilibrium separation as output.

The UBER has been successfully applied to interfaces constructed from slabs which do not exhibit significant surface relaxations, and hence were well approximated by the truncated bulk material[31–33]. Unfortunately, this is not the case when dealing with α–Al_2O_3 (0001), and this leads to ambiguity in choosing the correct structure of the oxide surface: Is it best to use a relaxed or unrelaxed surface for the energy vs. interfacial separation calculations, or some combination of both? One could argue that using a bulk-like termination is most realistic since the oxide will adopt a more bulk-like structure when interfaced with

[7] $\frac{2a}{3}[10\bar{1}0]_{Al_2O_3(LDA)}$ = 2.722Å and $a[\bar{1}10]_{Al(LDA)}$ = 2.808Å. The strain rate in our post-GGA calculations is higher (4.9%) since these involved only an evaluation of the total energy using the smaller, fixed LDA lattice constants.

Grid Dimension	# k-points	E_{diff}	$\mathcal{W}_{\text{ad}}$
$2 \times 2 \times 1$	2	-1.04	+0.85
$4 \times 4 \times 1$	4	+0.02	-0.02
$6 \times 6 \times 1$	7	-0.07	+0.05
$8 \times 8 \times 1$	10	+0.02	-0.02
$10 \times 10 \times 1$	14	-0.02	+0.01
$12 \times 12 \times 1$	19	0.00	0.00

Table 3.6: Convergence of $\mathcal{W}_{\text{ad}}$ in J/m^2 with respect to the number of irreducible $\mathbf{k}$-points. E_{diff} refers to the difference in total energy between the interface and isolated slabs in eV. The zero of energy is set to the value obtained in the 19 k-point calculation.

Al. Yet this choice will yield the wrong structure at large separations since it neglects the energetically and structurally large relaxations of the oxide surface. One possible solution would be to use the UBER interfacial geometry as a starting point for an additional geometry optimization calculation. The work of separation could then be estimated by finding the energy difference between the *relaxed* interface and the *relaxed* isolated slabs. We have adopted this relaxation approach as our second method for calculating $\mathcal{W}_{\text{ad}}$, and will make comparisons with our (unrelaxed) UBER calculations below.

To minimize numerical errors, the calculations on each interface model were performed using the same $\mathbf{k}$-points set and, where possible, the same supercell size. A thorough convergence test with respect to the number of irreducible $\mathbf{k}$-points was performed on the unrelaxed HCP Al–terminated interface geometry (HCP-Al) at an interfacial separation of 2Å (Table 3.6). It was determined that 10 $\mathbf{k}$-points gave a converged $\mathcal{W}_{\text{ad}}$ to within about 0.03 J/m^2, and this set was then used for all interface geometries. Relaxed structures were generated using a combination of conjugate gradient (for the initial relaxations) and quasi-Newton (mainly for fine-tuning) minimization of the Hellman-Feynman forces. All atomic coordinates were optimized until the magnitude of the force/atom was less than 0.05 eV/Å.

Depending on the nature of the interfacial bonding and atomic structure, the *adhesive* bonds formed between the metal and ceramic may be stronger than the *cohesive* metallic bonds within the metal. To assess this possibility, we have performed a few additional calculations of $\mathcal{W}_{\text{ad}}$ at selected points within the metal, thereby simulating adhesive metal transfer to the oxide.

3.5 Aluminum–terminated Interfaces

3.5.1 Adhesion and Atomic Structure

Results for UBER calculations on the Al–terminated interface systems are shown in Fig. 3.3. A nonlinear least squares fit to the *ab initio* LDA data gives the OT site as having the largest $\mathcal{W}_{\text{ad}}$ of 1.55 J/m^2, with the HCP and FCC sites ranking second and third, respectively (see Table 3.7). The values for the equilibrium interfacial separation are ordered such that the largest $\mathcal{W}_{\text{ad}}$ occurs for the smallest separation.

Taking the optimal structures given as output from the UBER calculations and using them as input for a series of LDA geometry optimization calculations yielded a *different* set of adhesion energies and interfacial

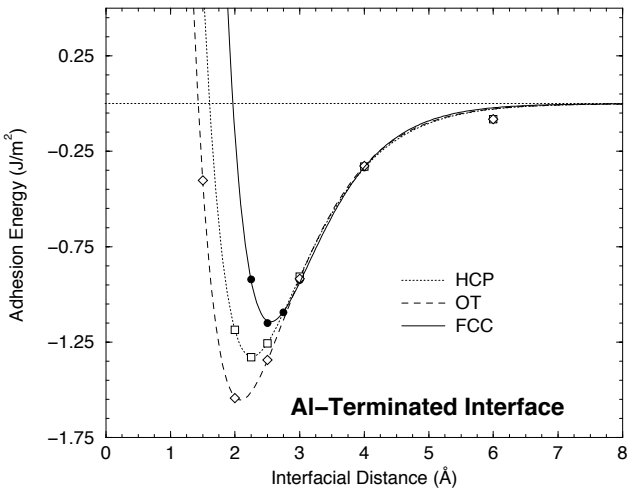

Figure 3.3: UBER curves for the Al–terminated interface as calculated within the LDA

separations. Table 3.7 compares these values to what was found for the UBER. As can be seen in the table, the relaxed values are of the same order of magnitude as those predicted by the UBER, but the *ordering* of the different sites has changed. Instead of the OT site having the strongest adhesion, the FCC site—which was predicted to have the weakest adhesion by the UBER calculation—is now preferred, with a drastically reduced interfacial separation of 0.70 Å, and $\mathcal{W}_{\rm ad} = 1.36$ J/m^2 (LDA), 1.06 J/m^2 (GGA). (An earlier study of Pt and Ag adsorption on alumina at a coverage of one monolayer also found the FCC stacking sequence to be perferred[46]). These values are in good agreement with the experimental $\mathcal{W}_{\rm ad}$ value of 1.13 J/m^2, (scaled to 0 K, as in Ref. [21]) determined from the contact angle of a sessile drop of Al on a single-crystal substrate of alumina in vacuum[154, 155]. The final relaxed structure of this interface is shown in Fig. 3.4, where one can see that there are substantial changes in the atomic geometry of the Al slab atoms near the interface. The most notable feature is the large displacement of one of the metal atoms (labeled "Al_2" in Fig. 3.4) towards the oxide. This atom fills the cation site that would normally be occupied were the alumina crystal structure continued along the $[0001]$ direction. It sits 1.46 Å above the O-layer (O_1) in the alumina, which is close to the distance of 1.33 Å found in the bulk. (The "vacancy" in the Al created by the displacement of the Al_2 atom is too small (having a "nearest-neighbor" distance of about 1.7 Å) to accomodate a replacement Al atom via diffusion from the bulk.) The ability of the interface to realize this lowest energy structure is facilitated by the FCC stacking sequence since it is the only structure that initially places the Al slab above the octahedral holes in the alumina. In addition to this feature, there is also a noticeable buckling of the atomic positions within each layer of the Al well into the slab, and the center of mass of the entire slab has shifted slightly closer to the oxide. Finally, the oxide's surface Al-layer (Al_1) resumes a more bulk-like position 0.76 Å above the O_1-layer upon formation of the interface, essentially undoing its relaxation in the clean surface. (This effect has also been seen for the adsorption of water and d-metal overlayers on alumina[46, 118]). In the bulk this distance would normally be 0.84 Å.

We note in passing that the similarity of the magnitudes of $\mathcal{W}_{\rm ad}$ as calculated by both methods is mainly due to a fortuitous cancellation effect between the relaxation energies of the interface and the isolated slabs.

		Unrelaxed(UBER)		Relaxed		
Stacking	**Termination**	$\mathbf{d_0}$	$\mathcal{W}_{\mathbf{ad}}$(LDA)	$\mathbf{d_0}$	$\mathcal{W}_{\mathbf{ad}}$(LDA)	$\mathcal{W}_{\mathbf{ad}}$(GGA)
fcc	Al	2.55	1.14	0.70	1.36	1.06
hcp	Al	2.26	1.33	2.57	0.69	0.41
ot	Al	2.09	1.55	1.62	1.18	0.84
fcc	O	1.45	9.11	0.86	10.7	9.73
hcp	O	1.38	9.56	1.06	10.3	9.11
ot	O	1.71	9.43	2.00	9.90	8.75
Experiment					1.13[a]	

[a] Ref. [21]

Table 3.7: Relaxed and unrelaxed values for ideal work of separation ($\mathcal{W}_{\mathrm{ad}}$) and minimum interfacial distance (d_0). The units are J/m^2 and Å, respectively.

For many of the interfaces, the amount by which the energy of the interfacial structure is reduced by allowing for atomic relaxations is approximately equal to what is found for the slabs.

In the remaining two stacking sequences for the Al–termination, the degree of atomic relaxation is much smaller. The HCP-Al system undergoes virtually no relaxation other than retraction of the Al_1-layer towards the oxide bulk. This explains the increase in d_0 upon relaxation of the UBER structure. In the OT-Al system one metal atom is slightly displaced towards the oxide, and there is a slight rotation of the interfacial metal layer with respect to the alumina's O sublattice.

Upon completing the LDA calculations, we followed up with a series of "post-GGA" total energy calculations for each LDA geometry (Table 3.7). We find that our PW91 GGA values for $\mathcal{W}_{\mathrm{ad}}$ have the same trend, but are systematically smaller than the corresponding LDA results by about 20-40%. Again, the FCC stacking sequence has the largest $\mathcal{W}_{\mathrm{ad}}$ of 1.06 J/m^2, which is in better agreement with the experimental data than the LDA value. We note that this trend of predicting lower binding energies is consistent with what is generally seen for the GGA,[8] yet we feel that the nearly 40% deviation for the HCP stacking is unusually large. At present we have no explanation for this discrepancy except to note that similar results have been noticed by others[1].

3.5.2 Electronic Structure and Bonding

Apart from simply analyzing the atomic structure and energetics of these interfaces, we have also used several methods to characterize the nature of the interfacial electronic structure and bonding. Since the valence electrons play a vital role in determining solid state phenomena, an analysis of this type can offer some explanation for the observed structures and adhesion energies and facilitate predictions for other interfaces. We begin our investigation with an examination of the charge density.

[8] Compare, for example, the LDA and GGA surface energies listed earlier in this paper.

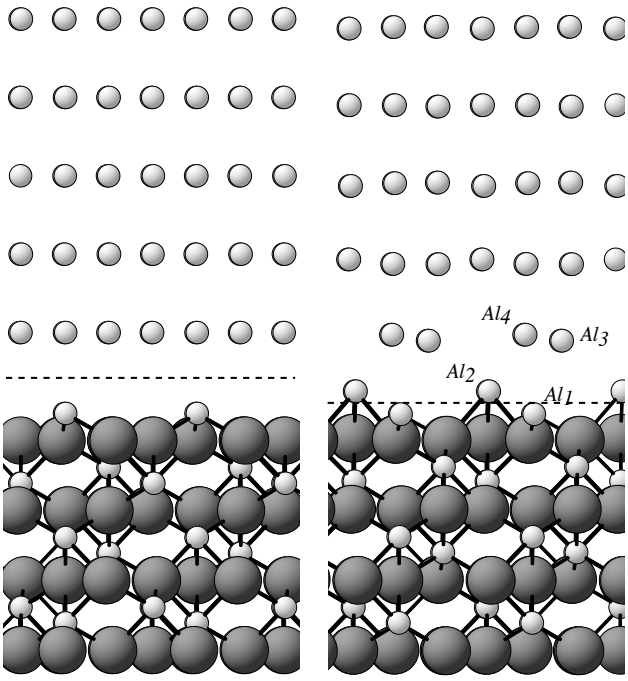

Figure 3.4: Left: the lowest energy geometry of the FCC–Al interface as predicted by UBER calculations; and, right: the final, relaxed structure. Small spheres represent Al atoms, large spheres represent O atoms. The direction of view is along $[1\bar{2}10]$, and the location of the interface is indicated with a dashed line. The interfacial Al atoms are labeled according to their height above the interfacial O-layer (O_1). The lower portion of the structure has been omitted for clarity.

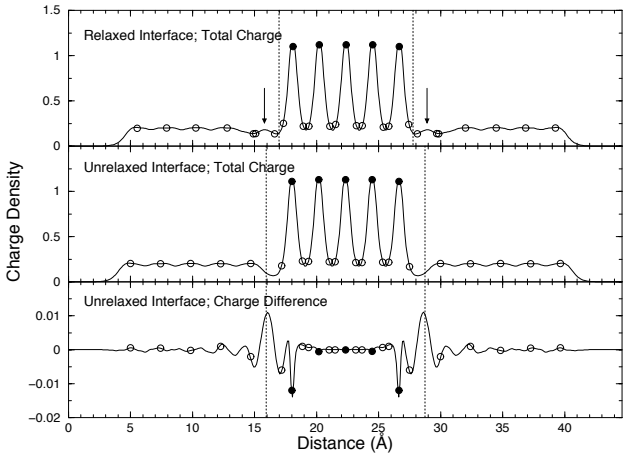

Figure 3.5: Planar averaged total charge density for the FCC-Al interface along the (0001) direction. Filled black circles give the location of the O atoms, open circles represent the Al atoms, and the vertical lines bisect the region separating the Al slab from the oxide slab. Top panel: charge density from the relaxed interface; Middle panel: charge density as predicted by the UBER calculation; Bottom panel: difference charge density (total UBER charge - charge density from the unrelaxed, isolated slabs).

Charge Density

Figure 3.5 shows the planar-averaged valence charge density along a direction perpendicular to the FCC-Al interface for three different scenarios. In addition to showing the symmetry of the interface geometry, the figure also gives locations of the atoms by open and closed circles (Al and O atoms, respectively). The location of the interface is represented with a dotted vertical line.

The top panel of the figure gives the total charge density for the optimal, relaxed interface. When compared to the density from the unrelaxed (UBER) system in the middle panel, one can see that the Al slab atoms near the interface are displaced towards the oxide, with one of these atoms (Al_2) ultimately situated closer to the oxide than to the metal. As a result of this displacement there is a depletion of charge mainly within the first layer of the Al slab, indicative of weakened metallic bonding. This is a short-range effect, however, since the charge density returns to the bulk value by the second layer. Additionally, a small peak (identified by vertical arrows in Fig. 3.5) in the charge density appears between the Al_2 atom and the remaining interfacial metal atoms (Al_3, Al_4). As will be shown later, this can be explained in terms of covalent bonding, both within the metal (compensating for the reduction in metallic bonding), and *across* the metal–ceramic interface.

The middle and bottom panels of Fig. 3.5 show the total and difference charge density for the (unrelaxed) structure predicted by the UBER calculations. The difference charge was evaluated by subtracting the sum of the isolated slab charge densities from the total interface charge density. Unlike the charge profile for the relaxed interface, the unrelaxed charge shows virtually no distortion arising from interfacial bonding at any depth into the constituent slabs, yet there is a pronounced depletion region at the interface which is partially filled upon allowing for atomic relaxations. The difference charge density shows regions of charge depletion on the oxides's O_1-layer and Al_1-layers and on the first layer of the Al slab; there is relatively little

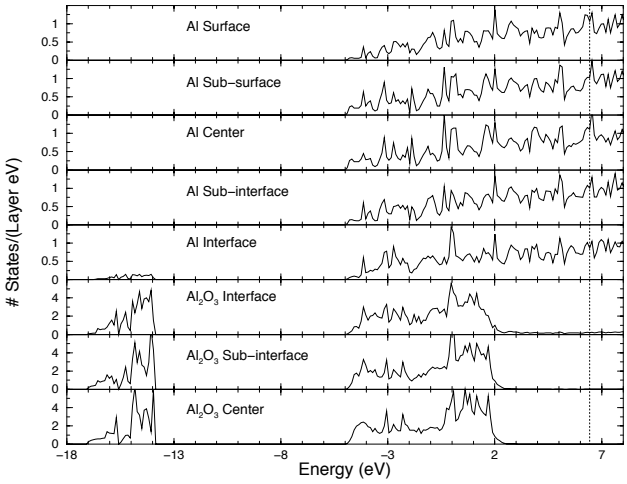

Figure 3.6: Total DOS projected onto selected atomic layers for the FCC-Al interface. The projection begins in the top panel with the surface layer on the Al slab, and progresses through this slab to the interface and finally into the center of the oxide. The dotted vertical line gives the location of the Fermi energy.

change in the density for layers deeper into the slabs. The depleted charge accumulates in the interfacial region, suggesting a covalent bond. However, as we will later see, this interpretation is premature in that it neglects the important role played by atomic relaxations. Indeed, the covalency evident here will ultimately be overshadowed by an ionic interaction, a fact which is obscured by analyzing *only* the unrelaxed structures.

Partial Density of States

Figures 3.6 and 3.7 depict the layer-projected and Al-atom-projected densities of states (DOS), respectively, for the relaxed FCC-Al interface.[9] Looking at Fig. 3.6, we note first that the effect of the interface is rapidly screened by the metal slab, as there is little indication of changes to the bulk Al DOS beyond the interfacial layer. At the interface layer there is a small degree of overlap between the hybridized $3sp$ states on the Al atoms in the -17 to -14 eV range with the O $2s$ levels, suggesting a covalent, σ-type bonding. The effect of the interface on the oxide's DOS is also well-localized. (In the oxide a layer is defined as consisting of one molecular unit of alumina.) Apart from the presence of some metal-induced gap states (MIGS) on the interface layer, the electronic structure is already bulk-like by the sub-interface molecular unit.

A more insightful way to visualize local changes to the electronic structure is to project the DOS onto selected Al atoms. This provides a common basis for comparison since Al is present in both slabs. It is then possible to single out individual atoms for analysis, and thereby assess their importance in bonding without the ambiguity that results when DOS data are projected onto layers.

Looking then at Fig. 3.7 we notice several important features that are either not apparent or obscured in Fig. 3.6. Firstly, the aforementioned low energy states on the interfacial Al layer are due to a bonding

[9]For the Al slab atoms we used an enlarged covalent radius of 1.51Å for the Wigner-Seitz radius (r_{ws}). For the oxide we chose: $r_{ws}^{\mathrm{Al}} = 1.19$Å and $r_{ws}^{\mathrm{O}} = 1.29$Å, which are scaled averages of the respective covalent and ionic radii. All r_{ws} were scaled so that the sum of the volume of the Wigner-Seitz spheres covered $\sim 100\%$ of the simulation cell volume.

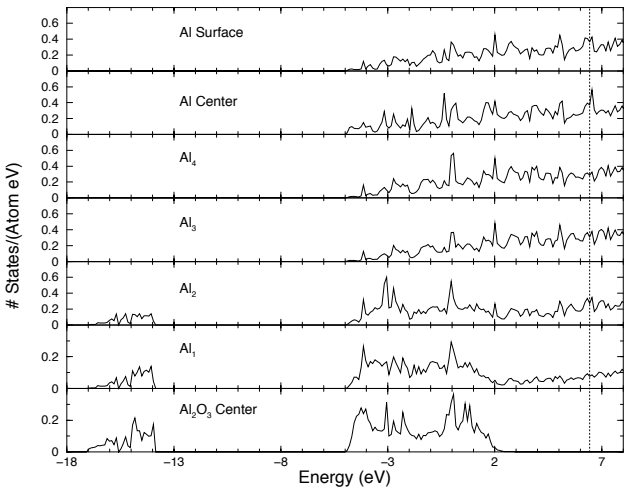

Figure 3.7: Total DOS projected onto selected Al atoms for the FCC-Al interface. "$Al_{1\text{-}4}$" refers to the distinct interfacial Al atoms identified in Fig. 3.4. The vertical dotted line gives the location of the Fermi energy.

interaction involving *only* the Al_2 atom. This is the atom pulled towards the oxide, and which ultimately occupies what would otherwise be a cation site in bulk alumina. In addition to the appearance of these new states, there is a depletion of states in the 2-6 eV range relative to the DOS for the more bulk-like Al slab atoms. This is consistent with what is seen for the cations of the oxide (the Al_1 and "Center" atoms), where the DOS in this range are either depleted or suppressed as they fall within the oxide's band gap. Finally, the Al_1 panel reveals that the MIGS mentioned in the layer-projected DOS are to a large extent localized on the oxide's interfacial cation.

To summarize our findings from the DOS analysis, we see that the changes in electronic structure for both slabs are generally confined to regions close to the interface, and that covalent bonding effects primarily involve only one atom from the metal slab (Al_2). The bond character is qualitatively similar to what is seen for the cation-anion interaction in the bulk oxide, involving overlap between hybidized Al $3sp$ states and O $2s$ states.

Electron Localization

Although a DOS analysis can reveal valuable information about the nature of covalent bonding, it provides limited insight into matters related to ionicity and charge transfer. Data such as these are key to understanding the character of interfacial bonding, and therefore we have employed other tools to obtain it. Recently, a novel graphical means for analyzing electron localization has been proposed and applied to the study of atoms, molecules, and solids[92, 93, 156, 157]. The so-called "electron localization function" (ELF) allows one to identify regions of space having a high concentration of paired and unpaired electrons which can subsequently be interpreted as bonds, lone pairs, and dangling bonds. Depending on the topology and magnitude of the ELF it is also possible to distinguish between metallic, covalent, and ionic bonding types. This makes the ELF a superb tool for inquiries into the nature and extent of atomic bonding, and we present

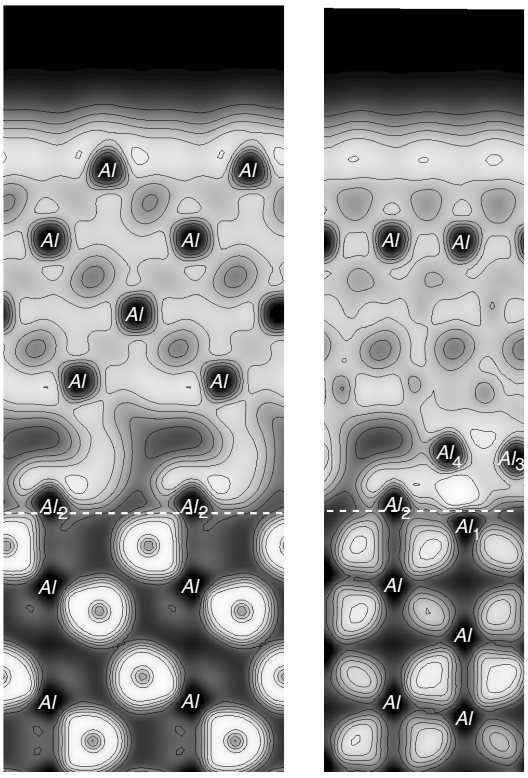

Figure 3.8: Two slices through the ELF for the FCC-Al interface taken along the $(10\bar{1}0)$ (left panel) and $(11\bar{2}0)$ (right panel) planes, showing four of the HCP O-layers in the oxide (bottom) and all five atomic layers from one of the Al slabs (top). The position of the interface is indicated by the dashed horizontal line, and the Al atoms which intersect the contour plane are labelled.

here—what is to our knowledge—the first application of the ELF to the study of metal-ceramic interfaces.

Figure 3.8 shows contour plots of the ELF data through two slices of the FCC-Al interface along the $(10\bar{1}0)$ and $(11\bar{2}0)$ planes. For clarity only one of the Al slabs (top) and slightly more than four O-layers of the alumina slab (bottom) are shown; a portion of the vacuum region is also visible at the top of the slices. We have chosen the origin of the $(10\bar{1}0)$ plane so that the slice passes through both the Al_2 atom (which is closest to the alumina) and one of its nearest neighbor O_1 atoms, allowing one to see the bonding interaction between them. This slice also passes through several other Al–O bonding pairs deeper into the oxide, and bisects many of the atoms in the Al slab. The $(11\bar{2}0)$ plane has its origin set so that it passes through all four Al atoms (Al_1–Al_4) adjacent to the O_1-layer. This positioning allows us to assess backbonding in the Al slab and any additional interactions between the Al slab and the oxide's Al_1-layer.

The magnitude of the ELF in the figure is given by a grey-scale color coding in which low values are represented by black, intermediate values by increasingly lighter shades of grey, and high values by white. By definition, ELF values fall within the interval $[0, 1]$, and in our plots five equally spaced contour levels divide the range $[0, 0.85]$. The ELF is approximately one both in regions where electrons are paired in a covalent bond, and near lone electrons from a dangling bond. Since we are using pseudopotentials to

simulate the effect of the atomic nucleus and core electrons, there is no physical significance to the data within the core regions, and the ELF assumes a small value there due to the low charge density.

Turning our attention towards the $(10\bar{1}0)$ plane (left panel), we note first the stark difference in ELF behavior between the metal and oxide slabs. In the bulk metal there is no evidence of strongly localized electrons, and the ELF assumes values close to 0.5 throughout the interstitial regions, which is characteristic of the homogeneous electron gas and metallic bonding. For the most part, changes to this behavior as a result of forming the interface are restricted to the interfacial layer. The oxide, on the other hand, consists mainly of regions of low charge density with most electrons localized on the O atoms. This indicates a highly ionic type of bonding. Nevertheless, there is still a small degree of covalency present, as the regions of high ELF (ELF "attractors") around the O atoms are not spherically symmetric and exhibit lobes directed towards the neighboring Al atoms. (The asymmetry is best seen in the $(11\bar{2}0)$ slice.) This corroborates our findings of limited covalency in bulk alumina from our preceding DOS analysis.

The $(10\bar{1}0)$ slice clearly illustrates the nature of the bonding between the O_1-layer and the subsumed Al_2 atom (whose location coincides with the region of low ELF just above the interface line in Fig. 3.8). In comparing the behavior of the ELF near the Al_2–O_1 bond with that of the Al–O bonds deeper into the oxide, we see that they are practically *identical*: most of the charge remains localized on the O_1 atoms, with distortions of the ELF attractor directed towards the Al_2 atom. This confirms our conclusions from the DOS analysis showing that the Al_2 atom has an electronic structure approaching that of the cations in bulk alumina, and suggests that a main contribution to Al–O interfacial bonding is of a mixed ionic-covalent type similar to what is seen in bulk alumina.

In addition to the Al_2–O_1 interfacial bonds, Fig. 3.8 gives evidence for Al–Al covalent bonding across the metal–ceramic interface. This can be seen in the $(11\bar{2}0)$ plane as the prominent white region between the Al_4 atom and the Al_1-layer. Additionally, there is another backbonding covalent-type ELF attractor between the Al_2 atom and a neighboring atom in the metal slab (Al_4), which is just barely visible in the $(10\bar{1}0)$ slice. These covalent bonds explain the small peak in the charge density seen in the top panel of Fig. 3.5 between the Al_2 atom and the Al_3/Al_4 atoms.

Finally, our ELF analysis indicates that atomic relaxation within the Al slab results in the formation of a charge depletion region in the vicinity of the original (unrelaxed) position of the Al_2 atom. (Note the region of low ELF above the Al_2 atom in Fig. 3.8.) This reduction in charge density was also visible in Fig. 3.5. The weakened metallic bonding within this region suggests a possible cleavage point for the interface. To test this hypothesis, we calculated $\mathcal{W}_{\text{ad}}$ for cleavage between the subsumed metal atom (Al_2) and the remainder of the metal slab. This is equivalent to a scenario in which the metal atom most strongly bound to the oxide is transferred to the oxide upon separation of the interface, *i.e.,* adhesive metal transfer. Our calculations give 2.06 (LDA)/1.63 (GGA) J/m^2 for cleavage within the metal, *vs.* 1.36 (LDA)/1.06 (GGA) J/m^2 at the interface, indicating that adhesive metal transfer for this interface is unlikely.

Mulliken Population Analysis

A common tool used to provide a semi-quantitative measure of charge transfer and ionicity is a Mulliken population analysis[158], in which the electronic charge is partitioned amongst the individual atoms. Although this partitioning can be performed in the context of a plane wave calculation by dividing the space around each atom into Wigner-Seitz spheres or polyhedra, a more intuitive division results by using a basis set of atomic orbitals. Since the absolute value of the atomic charge populations depends sensitively upon the choice of basis set (see Table 3.8), only differences between related structures using the same basis are meaningful in establishing trends. Our Mulliken analysis was performed using the SIESTA electronic structure code, developed by P. Ordejón and co-workers[90, 159]. SIESTA uses pseudopotentials and a basis set of pseudo-atomic orbitals for expansion of the valence electron wavefunctions. Our calculations utilized a "single zeta plus polarization" (*spd* orbitals) basis set to achieve a self consistent charge density on the relaxed interface structures generated by the converged plane wave calculations. For the purpose of making comparisons, we also performed calculations on the optimal LDA bulk crystals. All calculations were checked for convergence with respect to $\mathbf{k}$-point sampling; however, we did not endeavor to check the basis set for completeness, as we are only interested in evaluating trends.

The first result made clear by our population analysis is that there is a net charge transfer from the metal slabs to the oxide. With this choice of basis, we find about 0.6 electrons (e) transferred from both Al slabs, or about $0.3e$ per interface. (We again emphasize that the absolute magnitude of these numbers holds no physical significance of its own, and that a meaningful interpretation can be made only by comparing to another reference system. For example, later we will see that for the optimal O–terminated interface the amount of charge transfer is more than double that of the present structure.) By summing the charges layer-by-layer, we further find that most, if not all, of the charge lost by the metal comes only from the interfacial layer, as the remaining layers are each approximately neutral. Looking within this layer we find that it is the Al_2 atom that is mainly responsible for the charge transfer, with a charge of $+0.3e$ (see Table 3.9). It is interesting to note that in bulk alumina the corresponding Mulliken charge on the Al cations is $+0.73e$, which is slightly more than twice the value found for the Al_2 atom. This seems reasonable since this atom has only half the number of nearest-neighbor oxygens (3) it would have in bulk alumina (6). Furthermore, there are two different types of Al–O bonds in the bulk: three "long" bonds each of 1.97 Å and three "short" bonds of 1.86Å, and one would expect that the anions closer to the cation would exert a relatively stronger oxidizing effect. Since the Al_2 atom sits in one of the long bond sites we expect it to be oxidized by less than half the amount it is in the bulk, consistent with our results. Additionally, the oxide's Al_1-layer (which has short bonds to the three O_1 atoms) has an effective charge of $+0.4e$, slightly more than half of what is found in the bulk.

The remaining two atoms in the metal interfacial layer (Al_3, Al_4) exhibit smaller charges which are equal in magnitude but opposite in sign: about +0.1 and -0.1 electrons, respectively. These two charges appear to be the result of a position dependent image interaction[160–162]. Even though all the interfacial metal atoms sit in hole sites above the O_1-layer, these sites are not identical (see Fig. 3.2): one is located directly above the alumina's interfacial cation, while the remaining two are adjacent to O atoms, yet they differ

in their distance to the cations deeper into the alumina. Consistent with image charge theory, both metal atoms neighboring the negatively charged O atoms assume positive charges of +0.3e and +0.1e, respectively. Likewise, the Al_4 atom closest to the alumina's Al_1-layer (at +0.4e/atom) takes on a negative charge of -0.1e.

Excluding the Al_1-layer, the Mulliken population values for the remainder of the oxide atoms are virtually *identical* to what is found in the bulk. This is to be expected because in the FCC stacking sequence, the interfacial O atoms are still able to maintain their 4-fold coordination by oxidizing the subsumed Al_2 atom. The formal charge on each O atom is approximately -0.47e, with each Al cation at +0.7e.

Our finding of charge transfer from metal to oxide differs from what was observed by Verdozzi *et al*.[46] in their DFT study of the bonding between Pt and Ag monolayers on Al–terminated α–Al_2O_3(0001). They reported relatively weak bonding caused by metal polarization to the oxide's surface electrostatic field. On the other hand, a calculation (using a different local basis set) of bulk Nb on the same substrate by Batirev and co-workers[45] found a partially ionic metal-ceramic bond in which 0.37e were transferred to the oxide.

Bond Order Analysis

Just as a Mulliken population analysis can provide a semi-quantitative measure of ionicity, a Mayer bond order analysis[91] can give insight regarding the relative strength of ionic and covalent/metallic bonding between a given pair of atoms. This is done by assigning a numerical value to the bond in question. In an ideal situation (i.e., for an "appropriate" choice of basis set) a vanishing bond order would indicate either no bonding or a perfectly ionic bond. A value of unity would correspond to a single covalent bond, a double bond would have a value of 2, *etc*. Fractional values would then be interpreted as a mixture of ionic and covalent bonding, or metallic bonding.

Batirev and co-workers[45] recently demonstrated the value of a bond order analysis in an interface study of Nb(111) on α–Al_2O_3(0001), in which they found hybridization between Nb-4d and O-2p levels for the Nb-O bonds formed at an O–terminated interface. These bonds were found to extend into the second layer of the Nb, with bond orders of 0.6 and 0.3, for the first and second layers, respectively. In this section we describe the results of our bond order analysis performed on the optimal relaxed FCC-Al interface. We have once again used the SIESTA code, which we modified to calculate this information.

We have calculated bond orders for four systems: the bulk aluminum crystal, the bulk oxide, and the FCC O– and Al–terminated interfaces (Table 3.9). Although the final calculations used the same basis as in our Mulliken analysis (szp, single zeta + polarization), we briefly investigated the effect of basis set size on bond order for the bulk systems (see Table 3.8). We find that there is a noticeable dependence of the bond order on basis set, which is most evident upon inclusion of polarization orbitals. Even though the values of these bulk bond orders are fractional (as one would expect for metallic Al and ionic-covalent α–Al_2O_3), their basis set dependence suggests that one should not place too much emphasis on their absolute values. Rather, it is more meaningful to consider relative changes with respect to related systems (i.e., bulk *vs*. interface).

Table 3.8 shows that in bulk alumina the bond order of a short Al–O bond is 0.67 when using the szp basis. We find no significant deviations from this value for the same bonds within the oxide slab in

System	Basis Set	Bond Order	q(Al)	q(O)
Al	single zeta (sz)	0.21	0	
	double zeta (dz)	0.18	0	
	sz + polarization (szp)	0.26	0	
	dz + polarization (dzp)	0.28	0	
$\alpha-Al_2O_3$	sz	0.55	+0.95	-0.63
	dz	0.53	+0.97	-0.65
	szp	0.67	+0.73	-0.49
	dzp	0.76	+0.33	-0.22

Table 3.8: Bond orders and Mulliken charges for bulk Al and α–Al_2O_3 as a function of basis set size. The alumina bond orders are for the short Al–O bonds.

	FCC–Al	FCC–O	$\alpha-Al_2O_3$	Al
Mulliken Charge				
Al_1	+0.4	+0.4	+0.73	
Al_2	+0.3	+0.2		
Al_3	+0.1	-0.05		
Al_4	-0.1	+0.1		
O_1	-0.47	-0.46	-0.49	
Bond Order				
Al_1–O_1 *(short)*	0.7	0.65	0.67	
Al_2–O_1 *(long)*	0.42	0.45	0.5	
Al_1–Al_2	0.15	0.21		
Al_1–Al_3	0.24	0.19		0.26[a], 0.30[b]
Al_1–Al_4	0.56	0.21		
Al_2–Al_3	0.03	0.45		
Al_2–Al_4	0.41	0.04		

[a] (111) inter-plane
[b] (111) intra-plane

Table 3.9: Bond orders and Mulliken charges for the optimal Al– and O–terminated interfaces compared with the bulk oxide and metal. The Al atoms are labeled as in Figs. 3.4 and 3.10, and O_1 refers to the interfacial O-layer.

.

the relaxed interface. Here the average short bond order is about 0.66, and it is generally *independent* of proximity to the interface. One exception occurs, however, for the bonds between the oxide's Al_1-layer and its neighboring O_1 atoms. Here there is a slightly larger bond order of 0.7, suggesting a small increase in covalency with respect to bonds found in the bulk. The long Al–O bonds have a smaller bond order of 0.5, consistent with a reduction in covalency as a result of their longer bond length. These are also relatively insensitive to position within the slab.

Table 3.8 also shows that the nearest neighbor bond order in bulk Al is 0.26. This value is not maintained for all bonds in the interfacial Al slabs, as the lateral compression of the slabs (which was necessary to match the in-plane lattice constants of the metal to those of the oxide across the interface) induces an asymmetry in the bond orders between atoms within the same (111) plane vs. those in adjacent planes. We find that in regions away from the interface the *intra*-plane bond orders assume a value of 0.3, while the *inter*-plane bonds are identical to that found in the (unstrained) bulk, at 0.26. Presumably this agreement is a result of allowing for atomic relaxation in the [111] direction.

Unlike what was seen in the oxide, the presence of the interface generates changes in bond orders within the metal slab. These are confined to interactions either between the distorted interfacial layer and the next deepest layer (l_1–l_2 type), or within the interfacial layer itself (l_1–l_1 type). For l_1–l_2 bonding, we find that on average the bonds become more covalent, with a bond order of 0.35. The largest bond order within the metal, 0.41, occurs for the l_1–l_1 backbond between the Al_2 atom and one of its nearest neighbors, Al_4. Although the two atoms engaged in this bond were originally part of the same layer, the relaxation of the Al_2 atom towards the oxide has practically created a new layer closer to the interface. A portion of this bond can be seen in the $(10\bar{1}0)$ ELF slice of Fig. 3.8 as the white region to the upper right of the Al_2 atom. We conclude that formation of the interface results in a reduced metallic bonding within the near-interface regions of the metal in favor of forming more directional, covalent-type backbonds.

Obviously, the most important bonds in this system are those which span the interface. These can be divided into two groups. The first involves the three Al_2–O_1 bonds. In our earlier ELF and Mulliken analysis, we concluded that these bonds were qualitatively similar to the long Al–O bonds found in the bulk oxide. By comparing the bond orders at the interface with those found in the bulk we can determine *how* similar they are. Our calculations give: 0.38, 0.46, and 0.43, respectively for the three bonds, for an average bond order of 0.42 (see Table 3.9). This is only slightly smaller than the corresponding bulk value of 0.5, thereby confirming our earlier analysis. The deviation can be explained by differences in the bond lengths. In the bulk, the normal bond length is 1.97Å, whereas at the interface these three bonds are all longer, with lengths of 2.03, 2.11, and 2.04Å, respectively. (The longer bonds have the smaller bond orders.) This signals a small reduction in covalency. We ultimately conclude that these bonds are very similar to the long Al–O bonds found in bulk α–Al_2O_3.

The second type of interfacial bond links the oxide's Al_1-layer to an interfacial metal atom (Al_4) with a relatively large bond order of 0.56. This is about twice the value of other Al–Al bonds in the metal, and is easily seen in the $(11\bar{2}0)$ slice of Fig. 3.8 as the large white region at the interface. There is certainly some degree of covalency present in this interaction, as evidenced by the compact shape of the ELF attractor. This is a somewhat surprising result, as we did not expect to find significant bonding between the oxide's cations

and the metal. It would be interesting to determine what fraction of $\mathcal{W}_{\rm ad}$ could be attributed to this bond, and to compare the adhesion properties of our Al/α–Al_2O_3 system to those involving other corundum-like oxides with different cations: i.e., α–Fe_2O_3 and α–Cr_2O_3. Interfaces using these oxides will be the subject of a future study.

Finally, we note the presence of some weaker hybridization between the Al_1-layer and the Al_3 atom. The bond order here is 0.24, in close agreement with the metallic bond orders deeper into the Al slab. This interaction would explain the metal-induced gap states on the interfacial oxide layer seen in Fig. 3.6.

Summary of Bonding Analysis

We have found that there are *two* primary bonding interactions present at the FCC-Al interface. First, as revealed by the DOS, ELF, and bond order analyses, the Al–O bonds formed between the Al_2 atom and the alumina's O_1 atoms are very similar to the Al–O bonds found in the bulk oxide, and are therefore mainly ionic with a smaller degree of covalency. Secondly, our bond order and ELF analyses showed that there is a covalent interaction between the oxide's Al_1 (surface cation) layer and the Al_4 atom from the interfacial metal layer. Additionally, the atomic displacements within the metal's interfacial layer create small charge depletion regions that disrupt the metallic bonding. To compensate, Al–Al covalent backbonds are formed, which make cleavage within the metal unfavorable with respect to cleavage at the interface. Finally, although there is charge transfer from the metal to the oxide, within the oxide there are only small deviations from bulk-like bonding behavior, as the bond orders and Mulliken charges maintain their bulk values right up to the interfacial layer.

3.6 O–terminated Interfaces

3.6.1 Adhesion and Atomic Structure

The properties for the O–terminated interfaces are very similar to those of the Al–terminated ones: they undergo a similar relaxation, have the same preferred stacking sequence, have similar features in the DOS, and exhibit many of the same types of bonding. The major difference, then, is one of magnitude. The adhesion, relaxation, and bonding are all significantly stronger for the O–terminations. This is to be expected considering that a major component of the bonding in the Al–terminated case was ionic. By removing the oxide's surface Al-layer, the exposed O_1-layer becomes even more reactive (due to the presence of dangling O bonds), and it has a correspondingly more pronounced effect on the atomic and electronic structure of the neighboring metal slab.

Figure 3.9 shows the UBER curves for the three stacking sequences of the O–terminated interfaces,[10] with the resulting fitted parameters found in Table 3.7. Unlike the Al–terminations—in which there were substantial differences in $\mathcal{W}_{\rm ad}$ and d_0 between the different stackings—here the differences are minor, with all stackings having roughly $\mathcal{W}_{\rm ad} \simeq 9$ J/m^2, and $d_0 \simeq 1.5$Å. As a consequence of the strong Al–O interaction, the $\mathcal{W}_{\rm ad}$ values are now nearly an order of magnitude larger, with the HCP stacking having the largest

[10] We are uncertain why the quality of the fit is somewhat worse in this case.

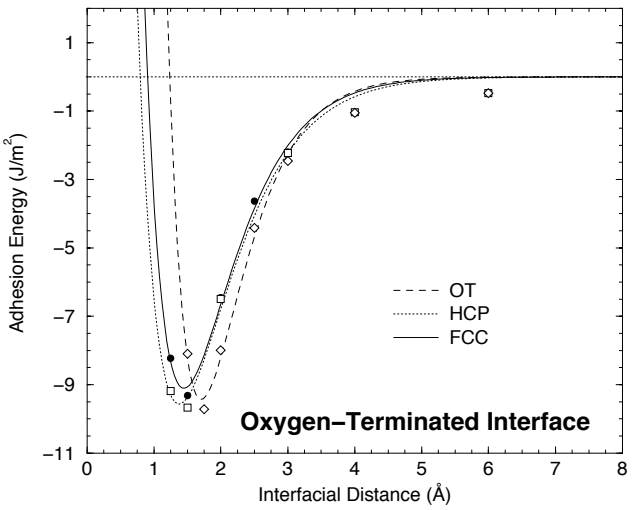

Figure 3.9: UBER curves for the O–terminated interface as calculated within the LDA.

value, $\mathcal{W}_{\rm ad} = 9.56$ J/m^2. Even the stacking with the largest interfacial separation is still more than 0.4 Å closer than the *smallest* separation found for the Al–terminations.

Starting from the minimum energy UBER configurations, further geometry optimizations yielded the relaxed $\mathcal{W}_{\rm ad}$ and d_0 values listed in Table 3.7. As was seen for the Al–terminations, relaxation results in a *re-ordering* of the adhesion energies for the different stackings. Whereas the HCP stacking was preferred according to the UBER calculation, the FCC geometry has the largest $\mathcal{W}_{\rm ad}$ after allowing for relaxation, with an increase of nearly 1.6 J/m^2 (LDA) over the unrelaxed result to a value of 10.7 J/m^2. We note that once again the system with the largest adhesion energy also has the smallest interfacial separation. This result is in partial agreement with Bogicevic and Jennison's[1] calculations for adsorption of Al on "ultrathin," O–terminated Al_2O_3 films. In contrast to our results, they found that at a coverage of 1 ML the OT site was preferred. However, for coverages greater than 1 ML, *either* the FCC or OT site was favorable. Finally, comparing the post-GGA adhesion energies with the corresponding LDA values, we find that the GGA predicts the same relative ordering of the adhesion energies, but with a slightly reduced magnitude of about 10-15%.

Our values of $\mathcal{W}_{\rm ad}$ for the Al/α–Al_2O_3 interface are less than those found for the Nb/α–Al_2O_3 system in Ref. [45]. In particular, our GGA value of 1.06 J/m^2 for the FCC-Al geometry is less than half that found for the corresponding Al–terminated Nb/α–Al_2O_3 structure, 2.8 J/m^2. However, for the O–terminated systems our value is only slightly smaller: 9.73 J/m^2 vs. 9.8 J/m^2. This trend is consistent with Bogicevic and Jennison's[1] calculations, in which for coverages up to 1 ML, Nb overlayers were found to bond more strongly than Al to an Al_2O_3 substrate.

Both the optimal UBER and final relaxed geometries of the FCC stacking sequence are shown in Fig. 3.10. The presence of the interface induces large changes in the local atomic structure of the metal well into the sub-interface layer. Instead of only one atom from the interfacial metal layer being pulled towards the oxide (as was the case for the Al–termination), there are now *two* atoms which sit in the alu-

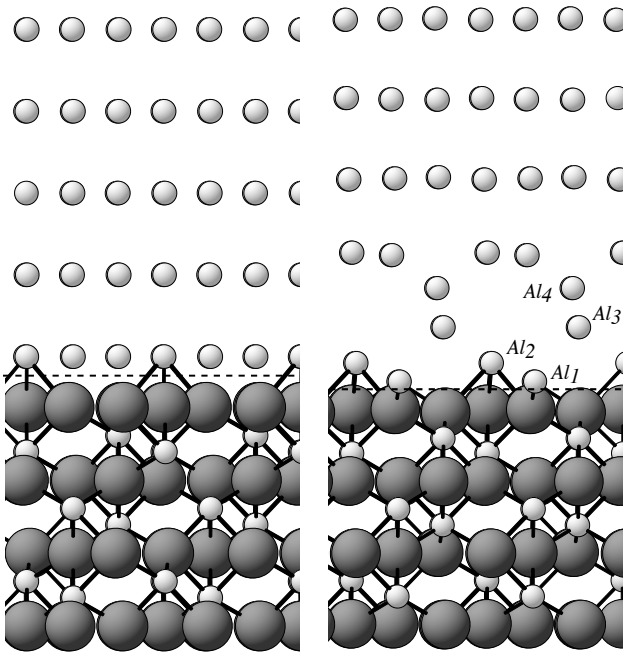

Figure 3.10: Left: the lowest energy geometry of the FCC–O interface as predicted by UBER calculations; and, right: the final, relaxed structure. Small spheres represent Al atoms, large spheres are Oxygen atoms. The direction of view is along $[1\bar{2}10]$, and the location of the interface is indicated with a dashed line. The interfacial Al atoms are labeled according to their height above the interfacial O-layer (O_1) The bottom portion of the structure has been omitted.

mina's cation sites (Al_1, Al_2). The atom closest to the oxide (Al_1) rests 0.86 Å above the O_1-layer, a mere 0.02 Å farther than in bulk alumina, and has bond lengths of 1.87, 1.84, and 1.83Å with its nearest neighbor O_1 atoms, as compared to the bulk distance of 1.86Å. The second displaced Al (Al_2) sits 1.42 Å above the O_1-layer, compared to the bulk spacing of 1.33 Å. It forms three long Al_2–O_1 bonds of length 1.96, 1.97, and 2.17Å. The corresponding bond length in the bulk is 1.97Å. These relaxations create a small void in the metal, separating what remains of the Al slab from the newly extended oxide structure. There are no significant changes in the oxide structure, as can be seen in Fig. 3.10. Additionally, a third metal atom (Al_3) in the sub-interface layer relaxes towards the interface, and the center of mass of the entire Al slab shifts away from the oxide. The remaining two stacking sequences undergo substantially smaller relaxations. The structure of the on-top (OT) site is virtually identical to its UBER geometry, with the exception of a rigid outward shift of the metal slab, and the HCP site experiences a small degree of atomic re-arrangement that is confined to the metal slab's interfacial layer.

An interesting consequence of allowing for atomic relaxations is the insensitivity of the oxide's final interfacial structure to its initial termination. By comparing the relaxed FCC structures of either termination (Figs. 3.4 and 3.10), we notice that in both cases the oxide is ultimately terminated by a *bilayer* of Al, with a geometry very similar to what is found in the bulk. In effect, the oxide has extended its stacking sequence across the interface in such a way that it seems more natural to consider the subsumed atoms as part of the alumina, with the true location of the interface shifted towards the metal.

3.6.2 Electronic Structure and Bonding

Charge Density

Figure 3.11 shows the planar averaged charge density for the FCC-O interface. As in Fig. 3.5, the top panel shows the total charge density for the fully relaxed interface, while the middle and bottom panels give the unrelaxed total and difference charge densities, respectively. Contrary to what was seen for the Al–terminated interface, the relaxed charge density is now depleted relative to the bulk in both the first *and* second layers of the Al slab, and is accompanied by a more substantial atomic rearrangement extending to the same depth. Within this charge depletion region there are two small peaks in the charge density (indicated by vertical arrows in Fig. 3.11), consistent with the formation of Al–Al covalent backbonds between the displaced Al atoms. The unrelaxed total density is relatively featureless except for the disappearance of the interfacial depletion region that was present in the FCC-Al system, Fig. 3.5. This is a result of the smaller interfacial separation in the O–terminated geometry. In the charge difference plot we note a depletion of charge around both Al atoms adjacent to the under-coordinated interfacial O atoms. Not surprisingly, this missing charge makes its way onto the more electronegative O ions, indicating the formation of an ionic bond. This interpretation will be verified by subsequent analyses of the electronic structure.

Partial Density of States

The layer-projected (Fig. 3.12) and Al atom-projected (Fig. 3.13) DOS for the FCC-O interface share many features with that of the FCC-Al system: the effects of the interface on the electronic structure of both the

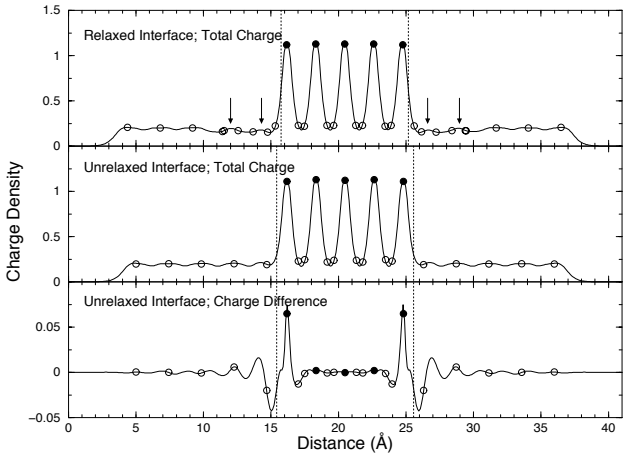

Figure 3.11:]
Planar averaged total charge density for the FCC-Oxygen interface along the (0001) direction. Filled black circles give the location of the O atoms, open circles represent the Al atoms, and the vertical lines bisect the region separating the Al slab from the oxide slab. Top panel: charge density from the relaxed interface; Middle panel: charge density as predicted by the UBER calculation; Bottom panel: difference charge density (total UBER charge - the charge from the isolated, unrelaxed slabs).

metal and the oxide are localized to within the first layer, there is a metallization (MIGS) of the interfacial oxide layer, and there is a set of new low energy states present on the interfacial metal atoms in the -16 to -13 eV range due to overlap with the O_1 $2s$ states. The main difference between the O– and Al–terminations is that there are now *two* atoms from the Al slab that participate in bonding with the interfacial O_1-layer. These are the two atoms (identified as Al_1 and Al_2 in Fig. 3.13) that are pulled closest to the oxide and which sit in the cation sites (see Fig. 3.10). Both exhibit the appearance of new overlap states with the O_1 $2s$ levels, and both show a depletion of states in the energy range coinciding with the oxide's band gap. Yet it is the Al_1 atom (closest to the oxide) that experiences the most pronounced changes in electronic structure, as its DOS closely resembles that of an Al atom from the center of the oxide ("Al_2O_3 Center"). Because two atoms now participate in covalent interactions with the oxide, the distortion of the Al slab's interfacial layer DOS (the "Al Interface" in Fig. 3.12) is more substantial than in the Al–terminated case: there now appear to be roughly twice as many states overlapping with the O_1 $2s$ levels, and the depletion within the oxide's band gap is more pronounced. We therefore conclude that there is still some degree of covalency maintained in the interfacial bonds between the subsumed metal atoms and the O_1-layer. Furthermore, since the DOS projected onto these metal atoms is qualitatively similar to what is seen in the bulk oxide, it is reasonable to classify the Al–O_1 interface bonds as being similar to those found in bulk alumina.

Electron Localization

Two contour plots of the ELF for the FCC interface are shown in Fig. 3.14. The slices are taken along the same directions and through the same origin as in Fig. 3.8. As was seen for the Al–terminated FCC interface, the bonding interaction between the two subsumed metal atoms and the alumina's O_1-layer is remarkably

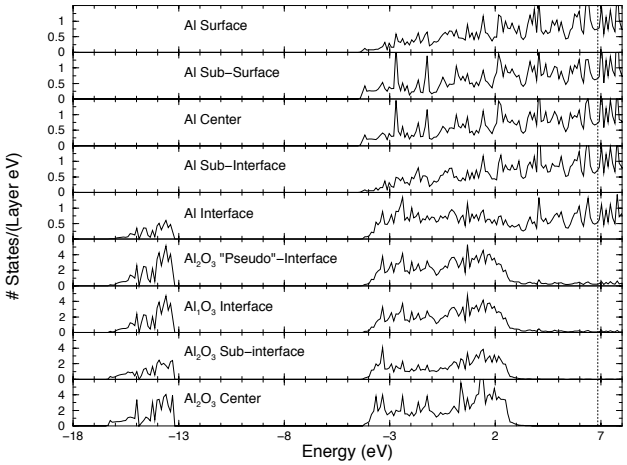

Figure 3.12: Total DOS projected onto selected atomic layers for the FCC–Oxygen system. The projection begins in the top panel with the surface layer on the Al slab, and progresses through this slab to the interface and finally into the center of the oxide. The "Al_2O_3 Pseudo-Interface" layer groups the Al_1O_3 interfacial unit from the oxide with the adjacent Al atom from the metal slab. The vertical dotted line gives the location of the Fermi energy.

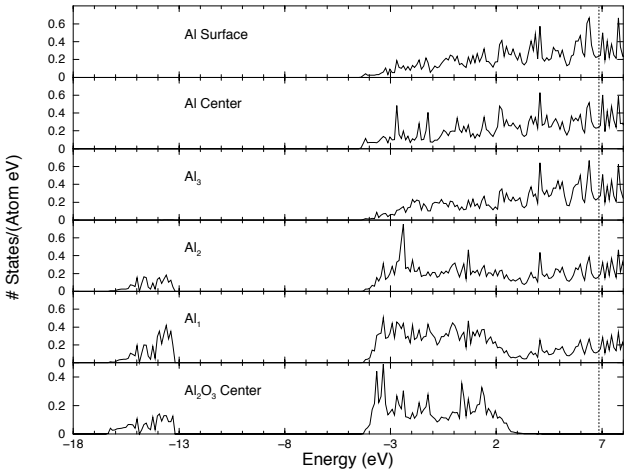

Figure 3.13: Total DOS projected onto selected Al atoms for the FCC–Oxygen system. "Al_{1-3}" refers to the three interfacial Al slab atoms identified in Fig. 3.10, and the vertical dotted line gives the location of the Fermi energy.

similar to the Al–O interaction visible in the bulk oxide. The majority of the charge is located on the anions—but in a highly asymmetric fashion—with lobes directed towards their neighboring cations. We thus conclude that the bonding is again mainly ionic with a smaller degree of covalency. In further likeness to the Al–terminated interface, we also find regions of increased charge localization just above the interface in the $(10\bar{1}0)$ slice. These indicate the formation of covalent backbonds between the subsumed metal atoms and the remainder of the Al slab, which compensate for the disruption in metallic bonding induced by the large changes in atomic geometry and ionic bonding. The atomic rearrangements are also responsible for the creation of a series of small voids in the charge density that extend well into the second layer of the Al slab, as seen in the $(11\bar{2}0)$ slice. In comparison, the voids are localized to within the first metal layer in the FCC-Al interface, Fig. 3.8. These regions of low density suggest a weakening of the structural integrity of the Al slab, and indicate a likely failure point for the interface under tensile stress applied perpendicular to the interface. Indeed, by cleaving the interface within the metal (between the Al_1 and Al_2 layers), we calculate $\mathcal{W}_{\text{ad}} = 0.67/0.56$ J/m^2 (LDA)/(GGA), which is more than an order of magnitude smaller than the 10.7/9.73 J/m^2 (LDA)/(GGA) required to break the bonds at the original location of the metal–ceramic interface. A similar case of adhesive metal transfer was observed by Batirev and co-workers[45] in their study of the O–terminated Nb/α–Al_2O_3 interface. They found that it was more favorable to cleave Nb–Nb bonds, and thereby transfer 1 ML of Nb to the oxide, than to cleave the strong Nb–O bonds at the interface.

Mulliken Population Analysis

Not surprisingly, a Mulliken analysis for the FCC-O interface reveals a much larger ionic interaction than was present in the FCC-Al system. There is now more than *double* the amount of charge transferred from the metal slabs to the oxide, about $1.3e$ total, or about $0.65e$ per interface. Whereas in the FCC-Al geometry most of this charge came from the one subsumed metal atom, now at least three metal atoms are found to participate in ionic bonding, with charge depletion present into the second interfacial metal layer (see Table 3.9). The two metal atoms closest to the oxide have charges of $+0.4e$ (Al_1) and $+0.2e$ (Al_2), with a smaller charge of $+0.1e$ found on one atom (Al_4) in the next deeper layer of the metal. The third interfacial metal atom (Al_3) has a slight negative charge of -0.05e. We note that the charge on the closest subsumed atom is *identical* to that found on the oxide's interfacial Al_1-layer in the FCC-Al case ($+0.4e$). This is to be expected since these atoms occupy essentially the same position. The Al_2 atom has a smaller charge of $+0.2e$ relative to the same in the FCC-Al structure ($+0.3e$). This reduction can be partially explained by charge depletion further into the metal slab, since by adding the charge on this atom to that of its Al_3 and Al_4 neighbors ($0.2e + 0.1e - 0.5e$) we recover most of the charge found in the Al–terminated structure. As before, the charges on the oxide atoms show little indication of disruption by the interface, and are virtually identical to their bulk values.

Bond Order Analysis

The results of our bond order analysis on the FCC–Oxygen structure further confirm that the interfacial Al_1–O_1 and Al_2–O_1 bonds are very similar to those found in the bulk oxide. For the Al_1–O_1 bond we calculate an

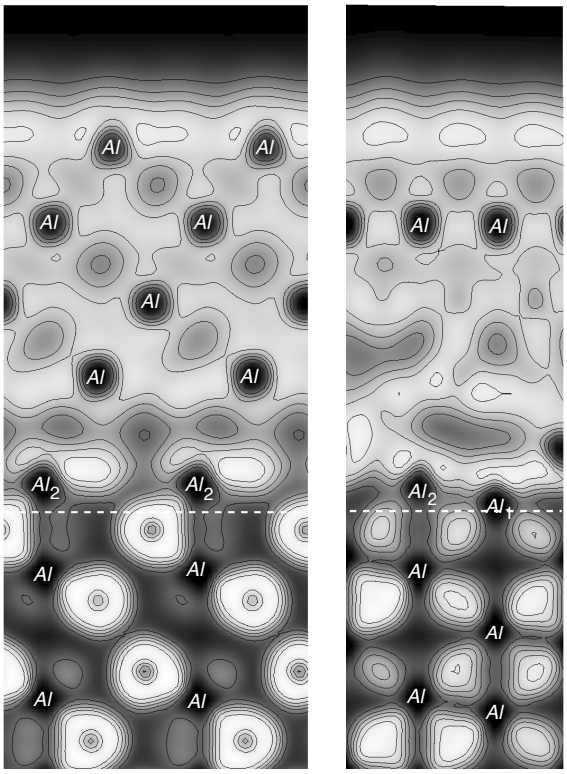

Figure 3.14: Two slices through the ELF for the FCC-Oxygen interface taken along the $(10\bar{1}0)$ (left panel) and $(11\bar{2}0)$ (right panel) planes, showing four of the HCP Oxygen layers in the oxide (bottom) and all five atomic layers from one of the Al slabs (top). The position of the interface is indicated by the dashed horizontal line, and the Al atoms which intersect the contour plane are labelled.

average bond order of 0.65 (see Table 3.9). This is in *very* close agreement with the typical short Al–O bond order of 0.66 found in the interior of the alumina slab. As mentioned earlier, a separate bulk calculation gave a value of 0.67 (Table 3.8). The three Al_2–O_1 bonds have an average bond order of 0.45. Although this is somewhat smaller than the corresponding bond order of $\simeq 0.5$ in the bulk region of the oxide, this discrepancy can be explained by the slightly longer bond lengths across the interface. In particular, the bond length/bond order values for these three bonds are given by: 1.96Å/0.53, 1.97Å/0.51, and 2.17Å/0.32, respectively. As one can see, the third bond is stretched by 0.2Å beyond its bulk length of 1.97Å, and it has a correspondingly smaller bond order, while the other two bonds are in excellent agreement with the bulk values. The close agreement in bond orders between the interfacial Al–O bonds and those found in the bulk oxide clearly demonstrates the ionic nature of the bonding at the FCC-O interface.

The combination of charge transfer with the large displacements of the metal atoms in the FCC-O geometry results in a local reduction in metallic bonding and a coincident increase in more directional, covalent Al–Al backbonds. (The same behavior was seen in the FCC-Al system.) For example, we find a bond order of 0.45 between the Al_2 and Al_3 atoms. In comparison, the normal bond order for an interlayer metallic bond is 0.26. This bond is visible in the $(10\bar{1}0)$ ELF slice from Fig. 3.14 as the region of high localization just above the interface. There is additional evidence of covalency deeper into the metal slab, where the bond between the Al_3 atom and its neighbor in the sub-interface layer is 0.39. Furthermore, the metallic bonds between the Al_1 atom and its nearest-neighbor metal atoms (Al_2, Al_3, and Al_4) are all weaker than in bulk Al: 0.21, 0.19, and 0.21, respectively (see Table 3.9). This explains the preference for cleavage within the Al (where only weakened metallic bonds must be broken) rather than at the interface (where strong, ionic Al–O bonds form). A similar reduction in Nb metallic bonding was observed in Ref. [45] for the O–terminated Nb/α–Al_2O_3 interface. In contrast to the metal, the bond orders in the oxide slab are virtually undisturbed by formation of the interface; even the bonds in the sub-interface layer have bond orders nearly identical to those found in the bulk.

It is interesting that our finding of ionic bonding supplemented by Al $3sp$–O $2s$ overlap for the FCC-O interface is qualitatively similar to the combination ionic and covalent/metallic bonding found for O–terminated Nb/α–Al_2O_3 in Ref. [45], despite the differences in metallic components. A more thorough study[1] of the adsorption properties of several transition metal overlayers on O–terminated ultrathin Al_2O_3 found that—with the exception of Nb—the preferred method of bonding (at 1 ML coverage) is via metal polarization induced by the oxide's surface Madelung potential.

Summary of Bonding Analysis

Our DOS, ELF, and bond order analyses show that the Al–O bonds formed across the FCC-O interface are very similar to those found in the bulk oxide, and are mainly ionic with a small degree of Al $3sp$–O $2s$ overlap. Due to the highly reactive, O–terminated alumina surface, roughly twice as much charge is transferred from the metal to the oxide relative to the FCC-Al system. Finally, although the Mulliken charges and bond orders within the oxide are relatively undisturbed by the presence of the interface, there are significant changes within the metal, where Al–Al covalent backbonds form to compensate for a reduction

in metallic bonding and disruption of atomic order near the interface.

3.7 Summary and Conclusions

In this chapter we have presented an *ab initio* study of the Al(111)/α–Al_2O_3(0001) metal–ceramic interface using bulk-like slabs and taking into account the effects of stacking sequence, oxide termination, and full atomic relaxations. A major focus was to determine the nature of the interfacial bonding. We find that, regardless of termination, the optimal interface geometry is obtained for the FCC stacking sequence, which places the metal atoms above the O hole sites in the alumina. An atomic geometry optimization resulted in substantial atomic displacements in the metal near the interface, wherein some atoms were pulled towards the oxide and assume positions which would normally be occupied by the Al^{3+} cations in the bulk crystal. The subsumed atoms are arranged such that they effectively terminate the oxide with a bilayer of Al, *independent* of its initial termination. Based on their positions and electronic structure, it seems more natural to consider these atoms as belonging to the oxide slab rather than to the metal, with the location of the metal-ceramic interface shifted into the metal. These atomic distortions also open up small charge density voids within the near-interface region of the metal, suggesting a possible cleavage point for the interface when placed in a uniform tension field. We examined this possibility by cleaving the interface within the metal, and found that separation preferrentially occurs at the original metal–ceramic interface for the FCC-Al geometry. However, the strong bonds at the FCC-O interface favor cleavage within the metal (adhesive metal transfer).

Two methods were used to estimate the ideal work of adhesion. First, we performed a series of total energy vs. interfacial separation calculations using unrelaxed slabs, and fit the data to the Universal Binding Energy Relation to obtain the optimal unrelaxed interfacial separation and adhesion energy. These geometries were then used as starting points for a determination of the relaxed interfacial structures and their corresponding adhesion energies. In allowing for atomic relaxations, we found that both the magnitude and rank-ordering of the adhesion energies for the different stacking sequences *changed* relative to the unrelaxed UBER results, underscoring the importance of including these effects. The calculated adhesion energies of 1.36 J/m^2 (LDA) and 1.06 J/m^2 (GGA) for the relaxed FCC-Al interface are in good agreement with the experimental value of 1.13 J/m^2, and suggest that an Al–terminated interface is the most physically realistic structure for low partial pressures of O_2 gas. For the FCC-O interface these values are about an order of magnitude larger, 10.7 J/m^2 and 9.73 J/m^2, respectively.

Finally, we applied several techniques to analyze the interfacial bonding for the optimal FCC-Al and FCC-O structures. Our primary finding is that the interfacial Al–O bonds in both systems are *very* similar to the cation-anion bonds found in bulk alumina, and are therefore mainly ionic with a smaller degree of covalency. In the O–terminated interface this ionic interaction is the dominant bonding mechanism, and it is responsible for the large adhesion energies. However, our ELF and bond order analyses for the FCC-Al interface indicate that there is some additional, covalent bonding between the oxide's surface Al monolayer and the metal. This suggests that the oxide cations could influence the value of $\mathcal{W}_{\rm ad}$. By analyzing the Mulliken charges we determined that there is twice as much charge transfer to the oxide in the O–terminated

interface relative to the Al–termination, and that the charge state of the subsumed atoms is similar to the cation charges found in the bulk oxide. Lastly, the bond orders and Mulliken populations in the oxide are generally unchanged by the presence of the interface, suggesting that most of its bonding requirements are satisfied by oxidizing the subsumed metal atoms. On the other hand, there is a reduction in metallic bonding in the Al near the interface as a result of its distorted atomic structure and charge transfer to the oxide. This is compensated for by the formation of more directional, covalent-type backbonds.

Chapter 4

The Al(111)/WC(0001) Interface

4.1 Introduction

Although there has recently been much activity aimed at understanding metal/oxide interfaces[7, 47, 163], much less is known about metal–ceramic adhesion involving non-oxide ceramics. Within this class, the transition metal carbides and nitrides are a particularly notable omission, considering their exceptional hardness, strength, and corrosion resistance[51]. In this chapter we present the first theoretical investigation of *any* metal/WC interface, focusing on Al/WC. WC is widely used in tribological applications as a wear-resistant coating for the purposes of reducing adhesion. However, the factors which determine the adhesive properties of a given coating are still poorly understood, and the evaluation of many coatings is often performed on a trial-and-error basis. At the other extreme, in microelectonics packaging there is generally a need for *strong* adhesion between a carbide or nitride layer and a metallic interconnect. Since the mechanical properties of an interface depend sensitively upon the detailed atomic and electronic structure at the junction, knowledge of this type would be a valuable tool in optimizing the performance of these, and other, systems. The goal of the present chapter is to calculate the electronic structure, W_{ad}, optimal geometries, and the interface stability of several representative polar Al/WC interfaces within a first-principles framework in order to better understand the nature of metal–ceramic adhesion. Previous studies have shown this approach to be reliable in reproducing W_{ad} values from experiment[7, 47, 56, 163]. The Al/WC system serves as a convenient model of simple-metal/transition metal carbide adhesion, in that both polar and non-polar interfaces may be considered with moderately-sized simulation cells resulting from similar lattice geometries. Our emphasis here is on the polar Al(111)/WC(0001) geometry; the Al(110)/WC(11$\bar{2}$0) system is discussed breifly in Ch. 6 and elsewhere[164].

This chapter is organized as follows: Section 4.2 presents the results of our bulk and surface calculations on the pure materials. The major results of this chapter are presented section 4.3, where we discuss the interfacial stability, adhesion, electronic structure, and the effects of alloys on the Al/WC metal-ceramic interface. Finally, we summarize our findings in Section 4.4.

XC	Pseudopotential	a (Å)	c (Å)	c/a	V_0 (Å^3)	B_0 (GPa)	E_{coh} (eV)
GGA	PAW	2.932	2.849	0.972	21.21	365	16.87
	Ultra-soft	2.920	2.840	0.973	20.98	375	16.67
LDA	Ultra-soft	2.881	2.802	0.973	20.15	418	19.70
	LCAO[a]	2.88	2.81	0.977	20.18	413	17.8
Experiment		2.91[b]	2.84[b]	0.976[b]	20.83	329[c]; 577[d] 434[e]; 443[f]	16.7[g]

[a] Ref. [165]
[b] Ref. [51]
[c] Ref. [166]
[d] Ref. [167]
[e] Ref. [168, 169]
[f] Ref. [169, 170]
[g] Estimated as in Refs. [69, 165, 171]

Table 4.1: Comparison of WC bulk properties: LDA vs. GGA and ultra-soft pseudopotentials vs. the projector augmented wave method. Experimental data and another first-principles calculation (based on a linear combination of atomic orbitals) are also presented.

4.2 Bulk and Surface Calculations

4.2.1 Bulk Properties

To assess the accuracy of the pseudopotential approximation and the importance of gradient corrections to exchange and correlation effects, we have performed a series of calculations on the bulk Al and WC phases. Results for Al were presented in Ch. 3 (see also Ref. [163]), where it was shown that the lattice constant, bulk modulus, and cohesive energy obtained with a norm-conserving RRKJ-type[81] GGA pseudopotential were in good agreement with experimental and other first-principles calculations; we refer the reader to Ch. 3 or Ref. [163] for further details.

The most stable phase of WC has the HCP crystal structure, with alternating W and C layers arranged in an $ABAB\ldots$ stacking sequence along the $\langle 0001 \rangle$ direction[51]. In order to gauge the significance of the W $4p$ semi-core states, we have performed calculations on WC using both ultrasoft-type[74, 75] (US) (in which the p states are treated via partial-core corrections[73]) and "all electron" Projector Augmented Wave (PAW) pseudopotentials[172, 173] (pp's). Total energies were carefully checked for convergence with respect to $\mathbf{k}$-points and planewave cutoff energy; it was found that 50 $\mathbf{k}$-points were sufficient to insure convergence to $\sim$1-2 meV/atom. To achieve the same level of accuracy, different planewave cutoff energies were required depending on which pp was used: 290 eV for US, 400 eV for PAW. Table 4.1 compares our results for the lattice constants, bulk modulus, and cohesive energy to that of experiment[51, 69, 166–171] and another first-principles LDA LCAO calculation.[165] Within the GGA, we find that use of the PAW results in only minor changes to the US values.[1] As a second comparison, Fig. 4.1 shows the WC GGA bandstructure evaluated using both the US and PAW pp's. The two methods agree very well for the

[1] In fact, use of the PAW leads to slightly *worse* agreement with experiment in terms of the lattice constants and cohesive energy.

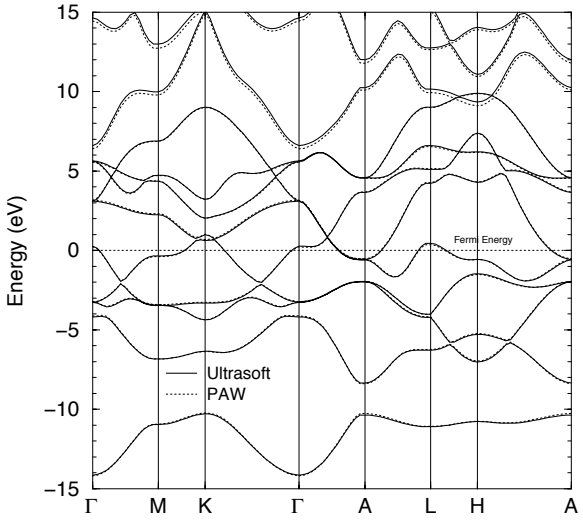

Figure 4.1: Comparison of WC bandstructure as calculated using ultrasoft (solid lines) and PAW (dotted lines) pseudopotentials.

occupied states (virtually to within the plot resolution of the band lines), although there is some deviation for the higher-lying unoccupied bands. Since the PAW is more computationally expensive, and since our tests show little—if any—loss of accuracy upon using the US pp's, we have utilized the US pp's for the remainder of this work.

Table 4.1 also illustrates that the GGA more accurately reproduces the experimental lattice constants and cohesive energy of WC, as compared to the LDA. On average, the GGA lattice constants are less than 0.2% larger than experiment, whereas the LDA values are about 1.2% too small. These trends are consistent with the "overbinding" commonly found in LDA calculations. Although the GGA bulk modulus is roughly 10% less than that predicted within the LDA,[2] because of the large scatter in the experimental data (possibly due to poor sample characterization) it is not possible to ascertain which method is more accurate in this regard. Overall, we conclude that the GGA yields the best agreement with experiment, and our remaining calculations are therefore performed at the GGA level of theory.

Although the electronic structure of WC has been analyzed via first-principles methods by other groups (see Ref. [165] and references therein), we present here a brief review of these properties in order to facilitate comparisons with what is found at our Al/WC interfaces. Generally, the bonding in WC can be classified as a combination of metallic, ionic, and covalent. The metallic aspect can be attributed to the partially filled W d bands, as evident in the bandstructure (Fig. 4.1) or, more readily, in the partial density of states[3] (pDOS) (Fig. 4.2). Further evidence of metallic bonding is present in the difference charge density of Fig. 4.3, where there is a delocalized region of charge accumulation in the interstitial regions. The ionic nature of the W-C bond is also most clearly revealed in Fig. 4.3, as a substantial amount of charge density centered on the W atoms is transferred to the more electronegative C atoms upon formation of the carbide. Lastly, the presence

[2] A similar discrepancy was observed for both Al and α–Al_2O_3.

[3] The Wigner-Seitz radii for evaluation of the angular momentum-projected DOS were set at: $r_W = 1.6$Å, $r_C = 0.96$Å, and $r_{\mathrm{Al}} = 1.51$Å.

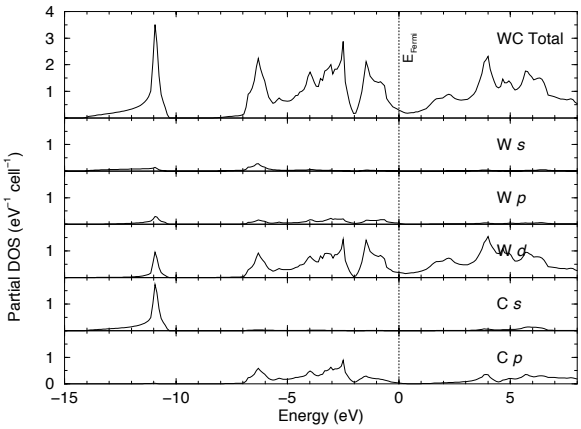

Figure 4.2: Total and angular-momentum projected DOS for bulk WC.

of a covalent interaction is indicated by the similar energy position and and shape of the pDOS (Fig. 4.2) for the C p (and to a lesser extent, s) and W d states.

4.2.2 Surface Properties

Convergence Tests

The purpose of this study is to simulate the interface between two *bulk-like* slabs. It is therefore necessary to insure that the slabs used are sufficiently think so as to exhibit bulk-like interiors, as it is known that the adhesion properties of thin films can differ significantly from those of thicker structures. To these ends, we have conducted convergence tests on the Al(111) and WC(0001) slabs in preparation for their use in interface calculations.

In Ch. 3 we presented results for the convergence of the Al(111) surface. We found that a relatively small slab consisting of only 5 atomic layers was sufficient to converge the surface energy and relaxations of the first two interlayer spacings. We have adopted that geometry in this study, and direct the reader to that Chapter for more information regarding those calculations.

The (1×1)(0001) (basal) surface of WC is classified as a polar surface since its terminal surface layer consists of a single species of C anions or W cations. Experimentally, this surface has been known to have a catalytic activity similar to Pt and Pd, and as such has been the focus of several experimental[174–176] and theoretical[177] investigations. The basal geometry poses some practical difficulties in determining the surface energy in the context of a supercell-based electronic structure calculation. That is, for a stoichiometric slab it is not possible to terminate both surfaces of the slab with the same species. In addition, an asymmetric geometry induces a spurious dipole moment within the supercell,[148] which can bias atomic forces and energies. A solution to this problem can be achieved by using a symmetric slab. This eliminates dipole effects, and allows the calculation of the surface energy (for a specific termination) by assuming a reasonable range of values for the C and W chemical potentials[178] (see the following section). By using a symmetric slab it is also possible to check for the presence of a bulk-like interior without requiring a surface

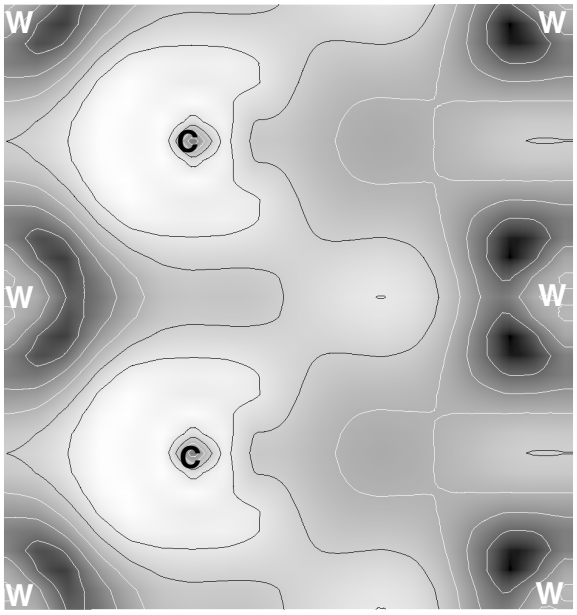

Figure 4.3: WC difference charge density (relative to the isolated atoms) through a $(11\bar{2}0)$ slice intersecting both W and C atoms. Charge redistribution is visualized by a greyscale scheme in which lighter shades (black contour lines) indicate charge accumulation, and darker shades (white contours) indicate charge depletion.

energy calculation.

Our tests on WC(0001) were performed using both C- and W-terminated slabs ranging from 3 to 13 layers thick. Additional $\mathbf{k}$-point convergence tests revealed that 10 irreducible $\mathbf{k}$-points were needed to converge the total energy to $\sim$1-2 meV/atom. A 10Å vacuum region was also included in the supercells to prevent interactions between periodic images, and all atomic coordinates were optimized to a force tolerance of 0.05 eV/Å/atom or less. We used three metrics to check for the presence of a bulk-like interior with respect to slab thickness, n: the workfunction ϕ, surface relaxations Δ_{ij}, and the total energy. Table 4.2 shows that ϕ converges rapidly with slab thickness, to within 0.1 eV for $n \geq 7$. For the W-termination we find $\phi \simeq 5.3$ eV, and for the C-termination $\phi \simeq 6.2$ eV. These values are in good agreement with those found by the unrelaxed LAPW calculations of Mattheiss and Hamann[177] (5.2 eV W-term., 6.4 eV C-term.), which

	ϕ (eV)	
# Layers, n	C-term	W-term
3	6.62	-
5	5.90	5.46
7	6.22	5.35
9	6.14	5.36
11	6.24	5.31
13	6.17	5.28

Table 4.2: Convergence of the workfunction ϕ with slab thickness for W- and C-terminated WC(0001).

Termination	Interlayer	Slab thickness, n						
		3	5	7	9	9:PAW	11	13
C	Δ_{12}	-21.8	-23.2	-22.5	-22.5	-21.8	-22.5	-22.5
	Δ_{23}		4.2	5.6	5.6	7.7	5.6	5.6
	Δ_{34}			-2.1	-2.1	-2.1	-2.8	-2.1
	Δ_{45}				0	0.7	0.7	0.7
	Δ_{56}						0	0
	Δ_{67}							0.7
W	Δ_{12}	-3.5	-4.2	-4.2	-4.2	-	-4.2	-4.2
	Δ_{23}		1.4	1.4	1.4	-	2.1	2.1
	Δ_{34}			0.7	0	-	0	0
	Δ_{45}				0.7	-	0.7	0.7
	Δ_{56}						0	0
	Δ_{67}							0

Table 4.3: WC(0001) surface relaxations as a function of termination and slab thickness. Units are percentage of bulk interlayer spacing.

were performed within the LDA using symmetric 9-layer slabs.

Table 4.3 compares the relaxations of the first few interlayer spacings Δ_{ij} as a function of slab thickness, n. Both terminations exhibit an oscillatory expansion/contraction behavior as one moves deeper into the slab (i.e., for increasing values of ij), and the contraction of the first layer of the C-terminated surface ($\Delta_{12} = -22.5\%$) is much larger than that found for the W-termination ($\Delta_{12} = -4.2\%$). Unfortunately, we are unaware of any experimental or first-principles calculations with which to compare these results. As final check on the agreement between pp's, we compared the US and PAW relaxations for the 9-layer C-terminated slab, and good agreement was obtained. Similar to our findings for the workfunction, Table 4.3 shows that relaxations up to the third interlayer (Δ_{34}) are well converged for $n \geq 7$. Lastly, we examined the change in total energy ΔE for increasingly thicker slabs. For slabs with $n \geq 7$ we found that ΔE was within 0.01 eV of the bulk energy per WC unit of -22.40 eV. Taken as a whole, these three tests consistently show that slabs with $n \geq 7$ possess a bulk-like interior and are therefore suitable for use in interface studies.

Stability

Due to the symmetry of WC(0001) it is not possible to calculate an absolute surface energy without resorting to a thermodynamic argument that accounts for the effects of non-stoichiometry. Since the stoichiometric slab has two different surfaces—one C-terminated, and one W-terminated—to extract the surface energy of one particular termination a non-stoichiometric model must be implemented, along with a generalized definition of the surface free energy, σ[178–180]:

$$\sigma = \frac{1}{2A}\left(E_{\text{slab}} - N_W\mu_W - N_C\mu_C + PV - TS\right). \tag{4.1}$$

Here E_{slab} is the total energy of a fully relaxed, 9-layer W- or C-terminated slab, A is the surface area, μ_W and μ_C are the chemical potentials of W and C, respectively, and N_W and N_C are the numbers of the

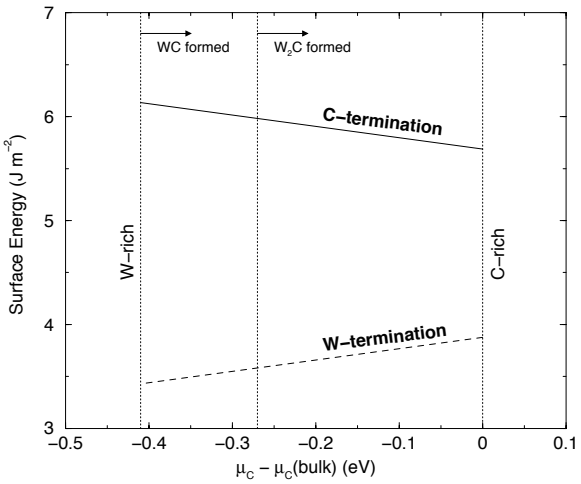

Figure 4.4: Surface energy vs. chemical potential for W– and C–terminated WC(0001) surfaces. Vertical lines indicate the range of stability of WC and W_2C.

corresponding atoms in the supercell. For typical temperatures and pressures, the PV and TS terms may be neglected. Furthermore, as the surface is assumed to be in equilibrium with the bulk, the chemical potential of the bulk carbide (μ_{WC}(bulk)), its heat of formation (ΔH), and the elemental bulk chemical potentials (μ_W(bulk), μ_C(bulk)) are related by:

$$\mu_{\mathrm{WC}}(\mathrm{bulk}) = \mu_W + \mu_C \tag{4.2}$$

$$\mu_{\mathrm{WC}}(\mathrm{bulk}) = \mu_W(\mathrm{bulk}) + \mu_C(\mathrm{bulk}) + \Delta H. \tag{4.3}$$

In addition, the chemical potential for each species must be less than the chemical potential in its bulk phase:

$$\mu_W \leq \mu_W(\mathrm{bulk}) \qquad \text{and} \qquad \mu_C \leq \mu_C(\mathrm{bulk}), \tag{4.4}$$

otherwise the compound would be unstable to decomposition into the elemental phases. In reality, there may be other compounds of different stoichiometry that further restrict the allowable range of μ_i values. For example, W_2C has a smaller (less negative) ΔH than WC, so WC would likely transform into W_2C before the bulk phases separate. Although it is conventional[178] to use the wider range of μ_i (i.e., with respect to the bulk phases), our results (Fig. 4.4) also indicate the regime where W_2C is stable.

Using the above relationships (Eq. 4.2-4.4), it is possible to rewrite Eq. 4.1 in terms of μ_C only:

$$\sigma = \frac{1}{2A}\left(E_{\mathrm{slab}} - N_W\mu_{\mathrm{WC}} + (N_W - N_C)\,\mu_C\right). \tag{4.5}$$

Equation 4.4 is plotted in Fig. 4.4 for both C- and W- terminations vs $\mu_C - \mu_C$(bulk) for the range given by:

$$\Delta H \leq \mu_C - \mu_C(\mathrm{bulk}) \leq 0. \tag{4.6}$$

Values for μ_{WC} and μ_C were taken from separate converged bulk calculations, and ΔH was determined to be -0.41 eV, in good agreement with the available (room temperature) experimental value[138] of -0.42 eV.[4] As shown in the Figure, our calculations predict that the W-termination has the lowest surface energy by about 2–2.6 J/m^2 over the entire range. In addition, the absolute values of both surface energies are relatively large, as one would expect from a polar surface. In particular, because the bonding in WC is partially ionic, cleaving along the basal plane breaks strong cation-anion bonds. This is energetically very unfavorable, and results in very reactive surfaces with large surface energies. As will be shown below, these reactive surfaces also impact interfacial adhesion energies.

4.3 Interfaces

4.3.1 Model Geometry

Our model of the Al/WC interface uses a superlattice geometry in which a 9-layer WC(0001) slab is placed between two 5-layer slabs of Al(111) (generating a 19 atom supercell), resulting in two identical interfaces per supercell. The free surfaces of the Al slabs are separated by 10 Å of vacuum, and additional $\mathbf{k}$-point tests showed that 37 sampling points were necessary to converge the total energy of the interface system to $\sim$1-2 eV/atom. In addition to interfacing the close-packed planes, the slabs were rotated about an axis normal to the interface so as to also align the close-packed directions, resulting in the orientation relationship:

$$\mathrm{Al}[\bar{1}10](111) \quad \| \quad \mathrm{WC}[11\bar{2}0](0001). \tag{4.7}$$

Using this orientation, there is a modest mismatch of 2.2% between the larger WC surface unit cell and that of the Al. To accommodate the periodic boundary conditions inherent in a supercell calculation, we invoke the coherent interface approximation[50] in which the (softer) Al is stretched to match the dimensions of the carbide. In a realistic interface, the mismatch would likely result in a widely-separated array of misfit dislocations, hence our model mimics the coherent regions between dislocations.

To identify the optimal interface geometry we performed a search over two parameters, resulting in six distinct candidate interface structures. The first parameter was carbide termination, in which the interfacial layer of WC was terminated by either W or C atoms. Secondly, we examined three stacking sequences (or rigid shifts of the slabs in the plane of the interface), placing the interfacial Al atoms in three high-symmetry positions with respect to the WC lattice structure (see Fig. 4.5). Adhesion energies and interfacial energies were then calculated for all six systems, both before and after allowing for atomic relaxations.

4.3.2 Work of Adhesion

Our estimates of the ideal work of adhesion ($\mathcal{W}_{\mathrm{ad}}$) were calculated using two different methods. The first is based on the Universal Binding Energy Relation (UBER)[32], and involves calculating the total energy

[4] Low temperature experimental thermodynamic data for WC is not available. Our calculations approximate μ_C with respect to the diamond phase, which is only 0.025 eV/atom higher in formation enthalpy than the more stable graphite phase.

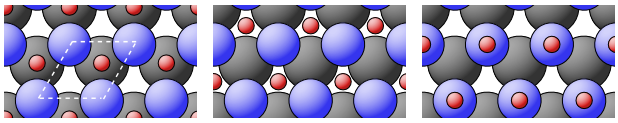

(a) HCP (b) Hole (c) OT

Figure 4.5: Three stacking sequences for the C-terminated Al/WC interface. Small spheres: Al interfacial atoms, medium-sized spheres: C atoms, large spheres: W atoms. The supercell profile along $\langle 000\bar{1} \rangle$ is shown in white.

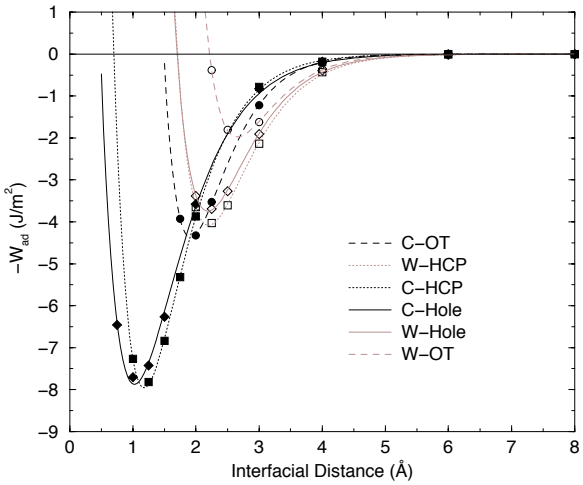

Figure 4.6: Universal Binding Energy curves for the six Al/WC interface geometries.

of an unrelaxed interface (formed by joining truncated bulk surfaces) as the interfacial separation is reduced from an initially large value. The *ab initio* data is then fit to the UBER function, yielding the optimal $\mathcal{W}_{\text{ad}}$ and interfacial separation, d_0 (see Fig. 4.6). The optimal geometries from the UBER calculations were then used to begin a second series of calculations in which the structure of each interface and isolated slabs were optimized via minimization of the atomic forces to a tolerance of 0.05 eV/Å.[5] To facilitate cancellation of errors between the interface models and interface vs. surface calculations, the same supercell dimensions and $\mathbf{k}$-points were used for all calculations.

Table 4.4 summarizes the optimal d_0 and $\mathcal{W}_{\text{ad}}$ values for all six interface structures, including both the unrelaxed (UBER) and relaxed geometries. Consistent with the argument that surfaces with larger surface energies are more reactive, and therefore more readily form bonds, we see that the C-terminated interfaces exhibit larger $\mathcal{W}_{\text{ad}}$ values for each stacking sequence. The HCP stacking yields the largest adhesion for both terminations, with relaxed values of 6.01 J/m^2 (C-term.) and 4.08 J/m^2 (W-term.) Also, the more strongly bound C-term. has an interfacial separation of 1.21Å—more than 1Å smaller than that for the W-term. The HCP geometry is preferred as it comes closest to continuing the carbide's bulk $ABAB\ldots$ stacking across

[5]Due to the symmetry of the supercell, all atomic relaxations were along a direction perpendicular to the interface only, and all in-plane forces were equal to zero.

		Unrelaxed(UBER)		Relaxed	
Stacking	**Termination**	$\mathbf{d_0}$ (Å)	$\mathcal{W}_{\mathbf{ad}}$ (Jm^{-2})	$\mathbf{d_0}$ (Å)	$\mathcal{W}_{\mathbf{ad}}$ (Jm^{-2})
HCP	C	1.18	7.96	1.21	6.01
Hole	C	1.03	7.88	1.11	5.40
OT	C	1.92	4.37	1.98	3.21
HCP: Al Cleave					2.42
HCP	W	2.20	4.09	2.22	4.08
Hole	W	2.19	3.75	2.21	3.90
OT	W	2.66	1.98	2.68	1.96
HCP: Al Cleave					2.29

Table 4.4: Unrelaxed and relaxed adhesion energies ($\mathcal{W}_{\text{ad}}$) and interfacial separations ($\mathbf{d_0}$) for the six Al/WC interface systems. Also, $\mathcal{W}_{\text{ad}}$ calculated for cleavage of the clean interface within the Al, between the interfacial and sub-interfacial layers.

the interface and into the metal; a similar effect was also observed for the Al/α–Al_2O_3 interface[163]. The on-top (OT) site is the least favorable structure, while the Hole site falls between, but somewhat closer to the HCP $\mathcal{W}_{\text{ad}}$. Unfortunately, we are not aware of any experimental data with which to compare our theoretical $\mathcal{W}_{\text{ad}}$ values.

Because this interface is characterized by relatively little atomic relaxation, the UBER interfacial distances are in good agreement (to within 0.1Å) with those obtained after relaxation. Generally, we find that allowing for relaxation increases the equilibrium UBER separation, and in most cases reduces $\mathcal{W}_{\text{ad}}$. The largest changes upon relaxation occur to the $\mathcal{W}_{\text{ad}}$ for the C-termination, which change by as much as 2.5 J/m^2. This can be explained by the energetically and structurally large relaxations present in the isolated C-terminated WC slab ($\Delta_{12} = -22.5\%$). These relaxations are about 5 times those found for the W-termination ($\Delta_{12} = -4.2\%$).

Table 4.5 shows the change in interlayer spacing (relative to bulk) for both relaxed HCP terminations as a function of distance away from the interface. Similar to what was seen in the clean surface, the WC spacings undergo an oscillatory contraction/expansion relaxation. However, the magnitude of the relaxations is much smaller in the interface, and exhibit a maximum deviation from bulk of less than 3%. This reduction is consistent with a return to a more bulk-like bonding environment as a consequence of interfacing with the Al. On the other hand, the Al spacings, although similarly small, undergo uniform contraction. This is at odds with the oscillatory behavior present in the free Al(111) surface[143, 163], and is an artifact of the tensile strain imposed by the coherent interface approximation.

One feature common to strongly bound interfaces is the phenomenon of adhesive metal transfer. This occurs during tensile loading of the interface, wherein interfacial failure occurs *within* one of the slabs comprising the interface, as opposed to at the interface proper. A portion of the fractured slab's material is then transferred to the other slab. In essence, the interfacial bonds (i.e., adhesive strength of the interface) are stronger than the cohesive strength of one of the interfaced materials. To assess whether adhesive metal transfer is a possibility for the Al/WC system, we have performed additional $\mathcal{W}_{\text{ad}}$ calculations on the optimal W-HCP and C-HCP geometries. This was done by separating the interface within the softer Al between

	Interlayer Dist. (Å), [% of Bulk]	
Interlayer	C-term.	W-term
Al_{2-3}	2.27, [-2.8]	2.23, [-4.3]
Al_{1-2}	2.32, [-0.7]	2.31, [-1.0]
Interface	1.21	2.22
WC_{1-2}	1.39, [-1.9]	1.38, [-2.7]
WC_{2-3}	1.43, [+0.9]	1.45, [+2.0]
WC_{3-4}	1.41, [-0.6]	1.42, [-0.2]
WC_{4-5}	1.43, [+0.5]	1.43, [+0.8]

Table 4.5: Interlayer spacing with respect to position perpendicular to the interface, given in terms of absolute distance (Å) and as a percentage of the respective bulk spacing (shown in square brackets). The central layer of the Al slab is denoted Al_3, the interfacial Al layer as Al_1, the central WC layer is WC_5, *etc*.

the interface and sub-interface layer (see Table 4.4 under the heading "Al Cleave"). We find that both interface terminations are subject to cleavage within the metal—to the extent that dissipative effects like plastic deformation can be neglected—as the calculated $\mathcal{W}_{\rm ad}$ of 2.3-2.4 J/m^2 within Al are much less than that for separation at the original metal–ceramic junction: 6.01 J/m^2 (C-term.), and 4.08 J/m^2 (W-term.). The possibility of adhesive metal transfer suggests that the polar Al/WC interface would not be an optimal choice for use in tribological applications such as dry machining or other applications requiring a weak a bonding between carbide and metal.

In conclusion, we find that the $\mathcal{W}_{\rm ad}$ for both (optimal) HCP terminations is relatively large, which is consistent with the polar nature of the WC(0001) surface. This large adhesion indicates a likelihood for adhesive metal transfer, as $\mathcal{W}_{\rm ad}$ values calculated within the Al slab are substantially smaller than those found at the Al/carbide junction.

4.3.3 Stability Analysis

Apart from knowing $\mathcal{W}_{\rm ad}$ for a particular interface, it is also desirable to know which interface is most stable in a thermodynamic sense. This can be assessed in a manner similar to what was done for the WC surface, by extending Eq. 4.2 to give the interfacial free energy, γ[47]:

$$\begin{aligned}\gamma &= \frac{1}{2A}\{E_{\rm int} - N_W\mu_{\rm WC} + (N_W - N_C)\,\mu_C \\ &- N_{\rm Al}\mu_{\rm Al}({\rm bulk})\} - 2\sigma_{\rm Al}. \end{aligned} \tag{4.8}$$

Here $2\sigma_{\rm Al}$ is the surface energy of the two free Al(111) surfaces, and $\mu_{\rm Al}({\rm bulk})$ is the chemical potential of bulk Al. Based on this, Fig. 4.7 plots the interface free energy for all six interface geometries as a function of $\mu_C - \mu_C({\rm bulk})$.

Although the C-HCP interface has the largest $\mathcal{W}_{\rm ad}$, its large surface energy results in the W-termination having a lower interfacial free energy, except for a small region within the C-rich regime.[6] Neglecting

[6] In this region WC is unstable to decomposition into W_2C.

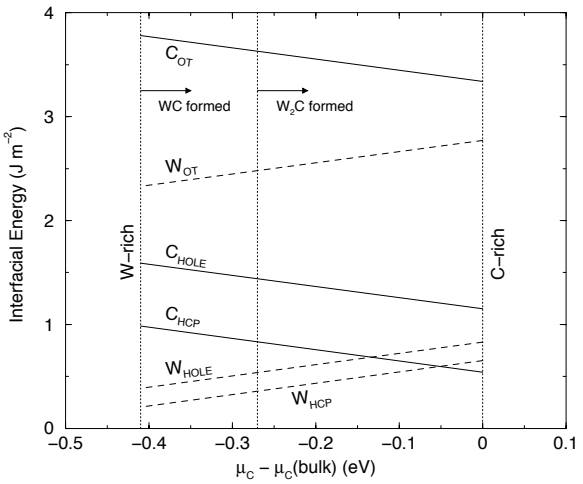

Figure 4.7: Interfacial free energy for the six Al/WC geometries as a function of $\mu_C - \mu_C$(bulk).

such effects as defect segregation, our calculations therefore predict that the W-termination should be the preferred equilibrium termination.

4.3.4 Electronic Structure

To reveal the nature of the interfacial bonding between metal and ceramic, Figs. 4.8-4.10 depict the interfacial charge density difference, it's planar average along $\langle 0001 \rangle$, and the layer-projected DOS, respectively, for the relaxed W-HCP and C-HCP interfaces. The difference charge density was evaluated with respect to the isolated slabs according to the relation:

$$\rho(\boldsymbol{r})_{\text{interface}} - \left[\rho(\boldsymbol{r})_{\text{Al(111)}} + \rho(\boldsymbol{r})_{\text{WC(0001)}}\right], \tag{4.9}$$

and is visualized in Fig. 4.8 using the same grey-scale scheme used in Fig. 4.3. The slice is oriented along $(11\bar{2}0)$, and those atoms intersected by the slicing plane are identified.

Despite their different terminations, there are some features of the interfacial electronic structure common to both systems. First of all, Fig. 4.8 shows that the interfacial charge re-distribution is a localized effect, being confined to within the first Al layer, and either the first (W-HCP) or second layer (C-HCP) in the carbide. This conclusion is supported by the DOS plot of Fig. 4.10, where the sub-interface DOS are similar to their values in the center of their respective slabs. Secondly, there are extended regions of charge depletion in the interstitial regions of the interfacial Al layer, as can be seen both in Figs. 4.8 and 4.9. This signals a reduction in lateral Al-Al metallic bonding in favor of forming new bonds across the interface.

In addition to these similarities, there are also significant differences in the interfacial bonding characteristics of the two terminations. Considering the W-HCP system first, we note in Fig. 4.8b a depletion of charge in the lateral W–W interfacial bonds similar to what is observed for the Al interfacial layer. This combination of charge density (from both the W and Al lateral bonds) is pushed into the interfacial region forming what roughly appears to be a mixed covalent/metallic bond involving a W d_{z^2} orbital. Further evi-

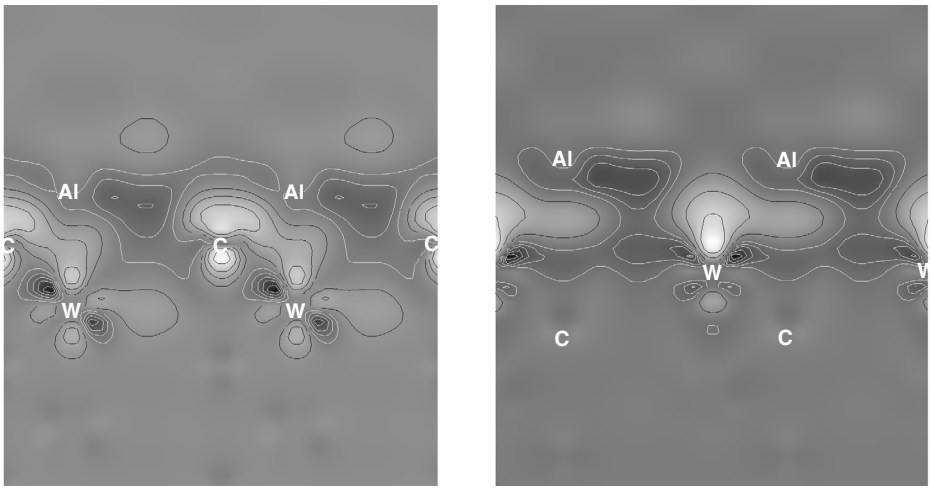

(a) C-HCP (b) W-HCP

Figure 4.8: Charge density difference (relative to the isolated surfaces) for the C-HCP and W-HCP interfaces taken along the $(11\bar{2}0)$ direction. The color scheme is the same as in Fig. 4.3, and the locations of the interfacial atoms are labeled.

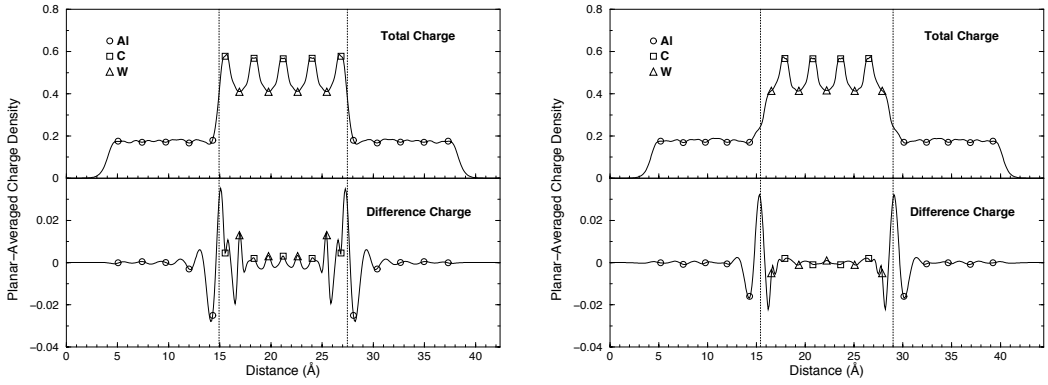

(a) C-HCP (b) W-HCP

Figure 4.9: Planar-averaged total charge and charge density difference (relative to the isolated surfaces) for the C-HCP and W-HCP geometries along a direction normal to the interfaces.

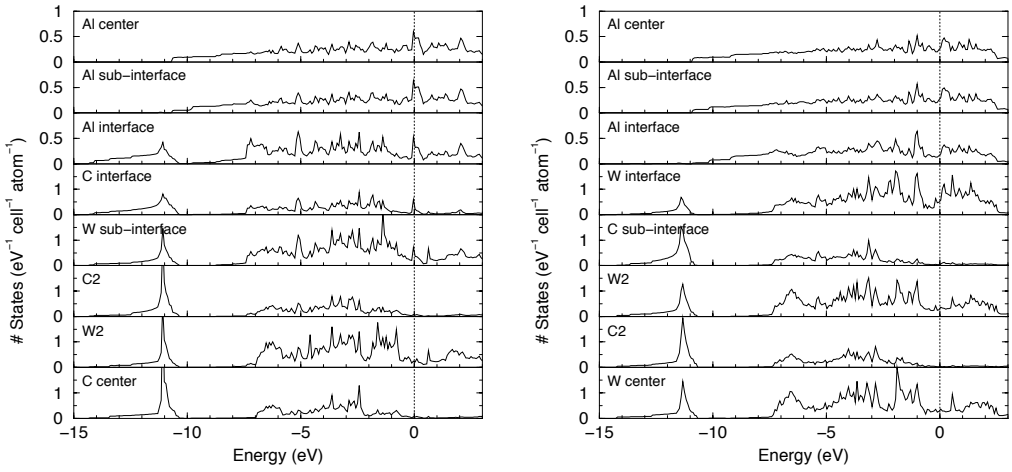

(a) C-HCP (b) W-HCP

Figure 4.10: Layer-projected DOS for the C-HCP and W-HCP interfaces.

dence for this can be seen in Fig. 4.9b where there is charge depletion on both the interfacial W and Al layers, coincident with a large increase in the interface region indicating a possible covalent/metallic bond. Lastly, the interfacial DOS (Fig. 4.10b) for the Al and W layers do not display any prominent features suggestive of a strong covalent interaction. Rather, the Al interface DOS is slightly perturbed in a fashion similar to the shape of its nearest-neighbor W atom with a similar trend observed for the W, as its DOS begins to look more free-electron like. We therefore interpret the W-HCP interfacial bond to be a combination of a weakly covalent and strong metallic interaction involving only the interfacial W d-states and Al $3sp$ states.

In contrast to the metallic/covalent character of the W-HCP system, the more strongly bound C-HCP interface shows signs of mixed covalent/ionic bonding. The effect of the interface also extends further into the carbide, as the d states on the sub-interface W atoms now participate in charge redistribution (see Fig. 4.8a). The depletion of W–W lateral bonding within the carbide's interfacial layer seen for the W-HCP system is not present for the C–C bonds in the C-HCP interfacial layer. Instead, Fig. 4.8a suggests a charge transfer from the Al interfacial layer to a C p_z orbital, and to a lesser extent a d_{z^2} orbital on the sub-interface W atom. This ionic-like effect is also visible in Fig. 4.9a, where the planar average of the charge difference shows charge depletion on the interfacial Al layer, accompanied by charge accumulation on the C and W interface atoms. However, the layer-resolved DOS for the C-HCP system (Fig. 4.10a) indicates that the charge-transfer from metal to carbide is not complete, and there remains some degree of covalent bonding. In particular, there are a new set of Al $3sp$–C $2s$ overlap states in the -14 to -10 eV range on the interfacial Al and C atoms. In addition, there is a depletion of states on the Al in the -10 to -7 eV range and in the region near the Fermi level (E_F). This depletion roughly mimics the behavior of the C p DOS states. Lastly, although the C atoms in the carbide bulk have a vanishing DOS near E_F, the presence of metallic Al at the interface induces new C gap states near E_F. Overall, the C-HCP DOS shows a much stronger covalent interaction than seen in the W-HCP system, due to formation of Al–C bonds. The partially ionic nature of

Termination	d_0 (Å)	$\mathcal{W}_{\text{ad}}$ (Jm^{-2})
C: clean	1.21	6.01
C: Li	1.42	3.50
C: Mg	1.46	4.31
W: clean	2.22	4.08
W: Li	2.36	1.98
W: Mg	2.39	2.58

Table 4.6: Changes in $\mathcal{W}_{\text{ad}}$ due to the substitutional incorporation of Li and Mg at the Al surface.

this interface explains its larger $\mathcal{W}_{\text{ad}}$ compared to the W-termination.

4.3.5 Alloy Effects on Adhesion

It is known that segregation of alloying agents to surfaces and grain boundaries (GB's) can significantly impact the mechanical properties, corrosion resistance, *etc*. of Al alloys[181, 182]. Although, most modern alloys (for example, the 5xxx series) contain several alloying agents in various amounts, Mg and Li are the dominant segregants to surfaces and GB's as a result of their larger atomic size. (Mg and Li are, respectively, 12% and 6% larger than Al.) Assuming a similar preference for segregation to interfaces, we have conducted a small set of *ab initio* calculations to determine how Li and Mg alter $\mathcal{W}_{\text{ad}}$ with respect to the clean interfaces.

Table 4.6 shows the relaxed interfacial separations (d_0) and $\mathcal{W}_{\text{ad}}$ values for the W-HCP and C-HCP interfaces assuming a substitutional monolayer of Li or Mg atoms replacing the interfacial Al layer. As in the clean interfaces, all atomic forces were minimized to a tolerance of 0.05 eV/Å. For both terminations we find that the presence of Li and Mg reduces $\mathcal{W}_{\text{ad}}$ and increases d_0—i.e., the impurity atoms weaken the interface. The reduction in $\mathcal{W}_{\text{ad}}$ is largest for the C-HCP system, where $\mathcal{W}_{\text{ad}}$ decreases by 2.5 and 1.7 J/m^2, respectively, for Li and Mg. For W-HCP the decrease in $\mathcal{W}_{\text{ad}}$ is smaller: 2.1 (Li) and 1.5 J/m^2 (Mg). The smaller effect on the W-HCP system can be explained by its larger d_0 of 2.22Å of the clean interface, versus 1.21Å for the C-HCP geometry: the W-HCP geometry initially has more free volume to accommodate the larger impurity atoms, and expands less upon their addition. This behavior suggests that strain effects play an important role in determining the effects of impurities on $\mathcal{W}_{\text{ad}}$. Nonetheless, strain effects are not the only factor at work, as can be seen by comparing the reduction in $\mathcal{W}_{\text{ad}}$ form Li with that from Mg. If strain effects alone were responsible for the changes in adhesion, then the larger Mg atoms should reduce $\mathcal{W}_{\text{ad}}$ the most. However, just the opposite behavior is seen, with Li having a stronger effect, suggesting that electronic contributions are also significant. The trend in interface separation more closely follows the behavior expected from a strain-only effect, as d_0 is largest for the Mg-containing structures. We note that an earlier study[33] of the effects impurity atoms on metal–ceramic adhesion involving C and S impurities at the Al/MgO(100) and Ag/MgO(100) interfaces found that, in general, impurities reduced $\mathcal{W}_{\text{ad}}$.

4.4 Summary and Conclusions

We have presented the first *ab initio* study of metal-ceramic adhesion involving the industrially relevant Al-WC interface. We have focused on the polar Al(111)/WC(0001) geometry due to its relatively small misfit, and Ch. 6 will investigate the non-polar Al(110)/WC$(11\bar{2}0)$ system and draw comparisons. Considerable care was taken to insure that the thickness of the slabs utilized were sufficient to insure a bulk-like interface. We find that both the clean WC surface and Al/WC interface are W-terminated, as these structures have the lowest surface and interfacial free energies. Overall, interface adhesion is relatively strong, with the optimal C and W-terminations yielding $\mathcal{W}_{\rm ad}$ values of 6.01 and 4.08 J/m^2, respectively. These values can be rationalized in terms of the large surface energies obtained for the polar surfaces. By cleaving along (0001) one creates a very reactive surface by breaking cation-anion bonds, and leaving behind a terminating layer with a large surface dipole. Despite the strong interfacial bonding, there are only small changes in the atomic structure at the interface; interlayer spacings in both the metal and the carbide are relatively close to their bulk values. Moreover, the optimal adhesion site for both terminations places the interfacial metal atoms in the HCP site with respect to the carbide stacking sequence. This geometry effectively continues the carbide crystal structure into the metal, and effect which has also been seen for the Al/α–Al_2O_3 system.

To further explain the trends in $\mathcal{W}_{\rm ad}$, we critically analyzed the electronic structure of both the C-HCP and W-HCP interfaces by referring to the charge density and layer-projected DOS. For both terminations the interface-induced changes in the electronic structure are very short-ranged and limited to the first (in the metal) or second (in the carbide) interfacial layers. The W-HCP system is characterized by a mixture of metallic/covalent bonding, whereas the stronger bound C-HCP interface exhibits ionic/covalent interactions, with charge transfer to the interfacial C layer.

Lastly, we considered the effects of Li and Mg alloying agents on $\mathcal{W}_{\rm ad}$. Consistent with their large size, we find that both reduce $\mathcal{W}_{\rm ad}$ by 1.5–2.5 J/m^2, and push the C-HCP and W-HCP interface apart, suggesting that strain effects are important. However, electronic effects are also significant, as the smaller Li impurities generate a larger reduction to $\mathcal{W}_{\rm ad}$—a result which cannot be explained in terms of strain effects alone.

Chapter 5

Al/VN vs. Al/VC

5.1 Introduction

In this chapter we present a theoretical comparison of metal–ceramic adhesion between Al/VN and Al/VC. Our emphasis here is on drawing comparisons between the effects of the non-metallic (metalloid) part of the carbide/nitride on adhesion. In particular, we would like to understand how the substitution VN $\rightarrow$ VC manifests itself in $\mathcal{W}_{\mathrm{ad}}$ and to explain any differences by analyzing the electronic structure of the interface. These ceramics are a convenient choice for the study of metal–ceramic adhesion because of their relatively low lattice mismatch with Al ($< 3.2\%$), and related "rigid band" bulk electronic structures.

The remainder of this chapter is organized as follows: Section 5.2 presents the results of our bulk and surface calculations on the pure materials. The major results of this Chapter are presented in section 5.3, where we discuss the adhesion, geometry, and electronic structure of the Al/VN and Al/VC metal–ceramic interfaces. Finally, we summarize our findings in Section 5.4.

Due to the substantial computational cost of performing a DFT calculation on supercells containing first row and transition metal elements, we emphasize that our molecular statics (0 K) predictions of structure and adhesion energies do not account for temperature and larger-scale size effects such as reconstructions and lattice mismatch. In addition, our models of VN and VC are restricted to perfect 1:1 V:N/C stoichiometry (to permit the use of smaller supercells), even though it is well known that carbides/nitrides of the Vb subgroup may contain 10-20% vacancies in the metalloid sublattice[51].

5.2 Bulk and Surface Calculations

5.2.1 Bulk Properties

To assess the accuracy of the pseudopotential approximation we have performed a series of calculations on the bulk Al, VN, and VC phases. Results for Al were presented in Ch. 3 (or see Ref. [163]), where it was shown that the lattice constant, bulk modulus, and cohesive energy obtained with a norm-conserving RRKJ-type[81] GGA pseudopotential were in good agreement with experimental and other first-principles calculations.

System	Method	a (Å)	B_0 (GPa)	E_{coh} (eV)
VN	GGA, US	4.132	316	12.21
	GGA, PAW	4.127	310	12.86
	GGA, FPLAPW[a]	4.12	333	–
	GGA, US[b]	4.13	317	–
	LDA, FPLAPW[a]	4.06	376	–
	LDA, NC[c]	4.19	338	–
	Experiment	4.126[d]	(233)[h]	12.49[e]
VC	GGA, US	4.170	304	13.86
	GGA, PAW	4.163	293	14.4
	LDA, NC[c]	4.22	321	–
	LDA, LMTO-ASA[f]	4.137	298	–
	Experiment	4.172[g]	(303)[h]	13.88[e]

[a] Ref. [183]
[b] Ref. [55]
[c] Ref. [184]
[d] $VN_{0.98}$ at 93 K, Ref. [185]
[e] Ref. [186]
[f] Ref. [187]
[g] $VC_{0.88}$ at 298 K, Ref. [185]
[h] Ref. [188]

Table 5.1: Comparison of VN and VC bulk properties as calculated using different *ab initio* methods with experiment. Results for the present study are given in the first two rows for each material. Abbreviations for the pseudopotential methods are defined as follows: US = ultrasoft pp's, PAW = projector augmented wave pp's, NC = norm-conserving pp's.

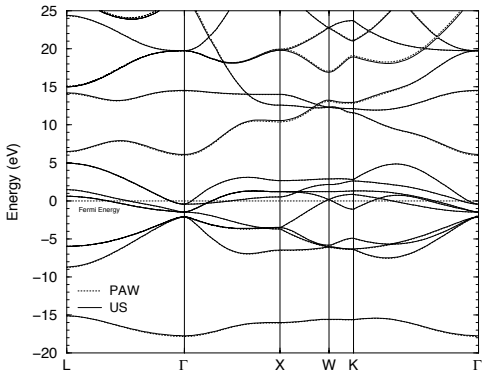

Figure 5.1: Comparison of VN bandstructure as calculated using ultrasoft (solid lines) and PAW (dotted lines) pseudopotentials.

Many transition metal mono-nitrides/carbides, including VN and VC, crystallize in the NaCl (rocksalt) structure. In order to gauge the significance of the V $3p$ semi-core states on the bulk structural and electronic properties, we have performed comparison calculations on both materials using ultrasoft-type[74, 75] (US) (in which the p states are treated only via partial-core corrections[73]) and "all electron" Projector Augmented Wave (PAW) pseudopotentials[172, 173] (pp's).

For the US pp set, the V pp was generated with an atomic valence configuration of $3d^4 4s^1$, which is the ground state as predicted by DFT. The outermost cutoff radius, r_c, was set at 1.36Å and the local potential was taken as the unscreened all-electron potential outside a radius, $r_{\rm loc}$ = 1.78Å. The C and N US pp's were implemented with valence configurations of $2s^2 2p^2$ and $2s^2 2p^3$, respectively, while using the d channel as the local pp component. Cutoff radii were set to $r_c^{\rm N} = 0.87$Å and $r_c^{\rm C} = 0.96$Å. Partial core corrections are generally unnecessary for first row elements, and therefore were not included for the metalloid elements.

The PAW pp set used a $3p^6 d^4 4s^1$ valence configuration for V, with $r_{\rm loc} = 0.94$Å and $r_c = 1.22$Å. The C and N pp's used the same valence configuration and local component as their US counterparts, while setting smaller $r_c^{\rm C} = r_c^{\rm N} = 0.79$Å. More information regarding the VASP pp's database can be found in the literature[75, 173].

Before starting the bulk calculations, the total energies of each unit cell were carefully checked for convergence with respect to $\mathbf{k}$-points and planewave cutoff energy; it was found that 56 $\mathbf{k}$-points were sufficient to ensure convergence to $\sim$1-2 meV/atom for both VN and VC. To achieve the same level of accuracy with respect to basis set size, different planewave cutoff energies were required depending on which pp set was used: 350 (400) eV for US (PAW) VN, 290 (400) eV for US (PAW) VC. Table 5.1 compares our results for the lattice constants, bulk modulus, and cohesive energy to that of experiment[185, 186, 188] and other first-principles calculations[55, 183, 184, 187]. (There is some uncertainty in the experimental data for the bulk modulus[188] due to the presence of pores and undetected impurities in the samples. These values are indicated with parentheses in Table 5.1.) We find that for both VN and VC, use of the PAW results in only minor changes to the US values, with both pp sets giving good agreement with the experimental lattice constant and cohesive energy. The trend in switching from US to PAW pp's is to produce slightly smaller lattice constants and bulk moduli, with larger cohesive energies. In the case of VN, agreement with the other

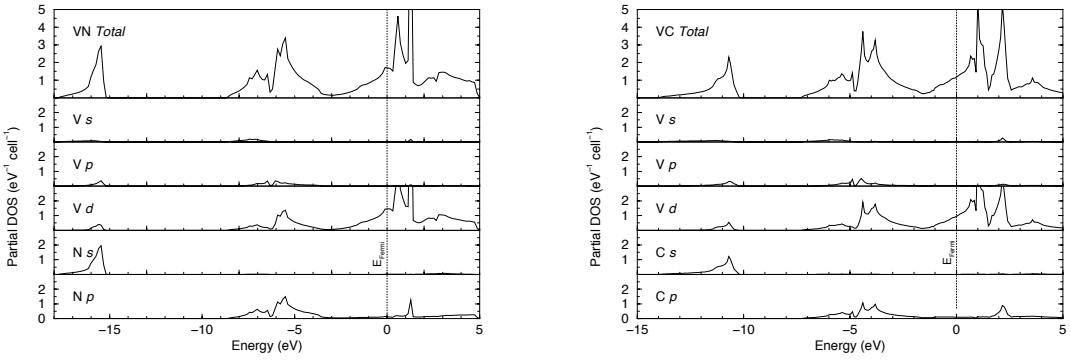

(a) VN (b) VC

Figure 5.2: Total and angular-momentum projected DOS for bulk VN and VC.

all-electron FPLAPW GGA values[183] and another calculation based on US pp's[55] is also very good. For VC, the only other *ab initio* calculations[184, 187] available for comparison are based on the Local Density Approximation (LDA) [65]. While our GGA calculations compare well with these in predicting the bulk modulus, the GGA lattice constants are in better agreement with experiment.

As a second, and perhaps more rigorous pseudopotential comparison, Fig. 5.1 shows the VN bandstructure evaluated using both the US and PAW pp's at their respective lattice constants. The two methods agree very well for the occupied states (to within the plot resolution of the band lines), although there is some minor deviation for the higher-lying unoccupied bands. Similar agreement was obtained for the US and PAW VC bandstructures. We further note that our VN bandstructure agrees well with another recent all-electron FPLAPW calculation performed by Stampfl and co-workers[183].

Since the PAW is more computationally expensive, and since our tests show little—if any—loss of accuracy upon using the US pp's, US pp's were used for the remainder of this work.

Although the electronic structure of the bulk phases of many transition metal mono-nitrides/carbides has been analyzed extensively via first-principles methods by other groups (see Refs. [183, 189] and references therein), we present here a brief review of these properties in order to facilitate discussion of the interfacial electronic properties. Generally, the bonding in VN/VC can be classified as a combination of metallic, ionic, and covalent, with the V d band being split into bonding and anti-bonding states by the octahedral crystal field of the metalloid atoms. Overall, these two materials share many features of their respective electronic structures despite having different numbers of electrons per unit cell. This so-called "rigid band" behavior manifests itself as an upward shift in the Fermi Energy of VN with respect to VC (see Fig. 5.2) as more anti-bonding states are filled by the one additional electron per unit cell provided by the N atom. Consequently, VN is observed to have a smaller cohesive energy.

The metallic nature of the bonding can be attributed to the partially filled d bands, as evident in the bandstructure (Fig. 5.1) or, more readily, by the peak in the partial density of states[1] (pDOS) near the

[1]The Wigner-Seitz radii for evaluation of the angular momentum-projected DOS were set at: $r_V^{\mathrm{VN}} = 1.51$Å, $r_V^{\mathrm{VC}} = 1.52$Å, $r_C = 0.93$Å, and $r_{\mathrm{N}} = 0.92$Å. For Al we used $r_{\mathrm{Al}} = 1.51$Å.

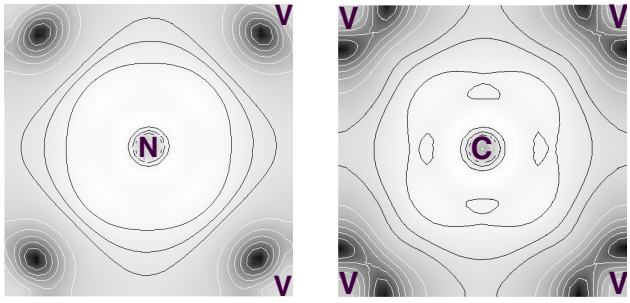

(a) VN (b) VC

Figure 5.3: Bulk VN and VC difference charge density (relative to the isolated atoms) through a (100) slice intersecting both V and N/C atoms. Charge redistribution is visualized by a greyscale scheme in which lighter shades (black contour lines) indicate charge accumulation, and darker shades (white contours) indicate charge depletion.

Fermi Energy (Fig. 5.2). The ionic nature of the V–metalloid bond is most clearly revealed in Fig. 5.3, as a substantial amount of charge density centered on the V atoms is transferred to the metalloid atoms upon formation of the compound. Moreover, the nearly spherically-symmetric shape of the nitride difference charge suggests a larger ionic effect than in the carbide, which is consistent with the larger electronegativity of N. (However, the effects of ionicity appear to be less important than the filling of covalent anti-bonding states, as the cohesive energies do not correlate with the electronegativity of the metalloid.) Lastly, the presence of a covalent p–d σ interaction is indicated by the similar energy position and shape of the pDOS (Fig. 5.2) for the N/C p and V d states.

5.2.2 Surface Properties

The purpose of this study is to simulate the interface between two *bulk-like* slabs. It is therefore important to ensure that the slabs are sufficiently thick so as to exhibit bulk-like interiors, as it is known that the adhesion properties of thin films can differ significantly from those of thicker structures. To these ends, we have conducted convergence tests on the Al(100), VN(100), and VC(100) slabs in preparation for their use in interface calculations.

One way to ensure the presence of a bulk-like slab is to check for the convergence of the surface energy with respect to the number of atomic layers, n. Upon attaining a critical thickness, the surface energy will converge to a fixed value, indicating that the two surfaces are decoupled by an intervening bulk region. We have calculated the surface energy for each of the (100) faces of Al, VN, and VC for slabs of sizes ranging from 3 to 11 layers using the method proposed by Boettger[133] (see Table 5.2). Before doing so, a separate $\mathbf{k}$-points test was performed on each surface supercell; to converge the total energy per atom to $\sim$1-2 meV, the carbide/nitride surfaces required a set of 10 $\mathbf{k}$-points, while for the Al system 36 $\mathbf{k}$-points were sufficient. All structures were relaxed to a force tolerance of 0.05 eV/Å per atom, and a 10Å vacuum region was used to prevent interactions between periodic images.

# Layers, n	Surface Energy (J/m^2)		
	Al(100)	VN(100)	VC(100)
3	0.90	1.11	1.30
5	0.89	0.97	1.32
7	0.85	0.97	1.27
9	0.89	0.95	1.29
11	–	0.95	1.27

Table 5.2: Convergence of the surface energy with respect to slab thickness.

As can be seen in Table 5.2, the surface energy for all three materials converges rapidly with increasing slab thickness to within about 0.05 J/m^2 for slabs with $n \geq 5$. An earlier study[163] on the Al/α–Al_2O_3 interface also observed rapid convergence for an Al(111) slab, where 5 layers were found to be sufficiently accurate for interface work. In that case a surface energy of 0.81 J/m^2 was measured, which is consistent with the present value of 0.89 J/m^2, as the close-packed (111) face of Al should exhibit a smaller surface energy than other low-index surfaces. We further note that the present value of the Al(100) surface energy is in good agreement with the experimental value[145, 146] of 0.94 J/m^2, as extrapolated to 0 K. We are not aware of any reliable experimental data for the surface energies of VN or VC. Nonetheless, it is reasonable that the surface energy of VC (1.27 J/m^2) should be greater than that of VN (0.95 J/m^2) considering that VC has a larger cohesive energy.

In addition to our examination of the surface energy, we considered the surface relaxations as a function of slab thickness. We found that these were also well converged by 5-7 layer slabs, with all relaxations being a relatively small 2% or less of the corresponding bulk spacings. For the VN and VC surfaces we refer here to the *average* relaxations, as there is some degree of surface rumpling present. In particular, while as a whole the first interlayer spacing in VN contracts by 1.7%, the individual V atoms relax inwards by 0.17Å, and the N atoms relax outwards by 0.1Å. In VC the relaxations are smaller: the first interlayer spacing contracts by 1.4%, the V atom moves inwards by 0.09Å, and the C atom shifts outward by the same amount, 0.09Å. For Al(100) the first interlayer spacing increases by 2%.

Based on the good convergence of the surface energies and relaxations, we conclude that slabs with $n \geq 5$ are sufficient for use in interface studies.

5.3 Interfaces

5.3.1 Model Geometry

Our model of the Al/VN and Al/VC interfaces uses a superlattice geometry in which a 7-layer VN (or VC) (100) slab is placed between two 5-layer slabs of Al(100), resulting in two identical interfaces per supercell with 24 total atoms. The free surfaces of the Al are separated by 10 Å of vacuum, and additional $\mathbf{k}$-point tests showed that 28 sampling points were necessary to converge the total energy of the interface system to $\sim$1-2 eV/atom. In addition to interfacing the (100) planes, the slabs were oriented about an axis normal to

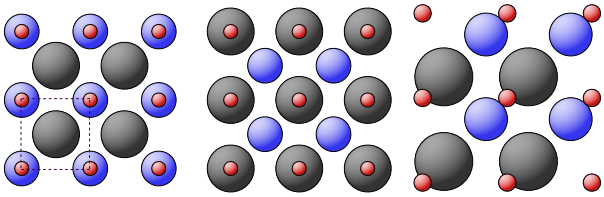

(a) N/C (b) V (c) Bridge

Figure 5.4: Three stacking sequences for the Al/VN and Al/VC interfaces. Small spheres: Al interfacial atoms, medium-sized spheres: N/C atoms, large spheres: V atoms. The supercell profile along $\langle \bar{1}00 \rangle$ is shown as a black dotted line.

the interface so as to align the [001] directions, resulting in a "cube-on-cube" orientation relationship:

$$\text{Al}[001](100) \quad \| \quad \text{VN/VC}[001](100). \tag{5.1}$$

Using this orientation, there is a modest mismatch of 2.3% (3.2%) between the larger VN (VC) ceramic surface unit cell and that of the Al. To accommodate the periodic boundary conditions inherent in a supercell calculation, we invoke the coherent interface approximation[50] in which the (softer) Al is stretched to match the dimensions of the ceramic. In a realistic interface with the above orientation relationship, the mismatch would likely result in an array of widely-dispersed misfit dislocations separated by $\sim 180\,\text{Å}$ ($\sim 129\text{Å}$) for the Al/VN (Al/VC) system. Hence, our model mimics the coherent regions between dislocations.

To identify the optimal interface geometry we considered three different stacking sequences, placing the interfacial Al atoms in one of three positions with respect to the ceramic surface lattice structure (see Fig. 5.4): above the V atoms (V-site), above the N/C atoms (N/C-site), and along the V-N/C bond direction (bridge-site). Adhesion energies were then calculated for each geometry, both before and after allowing for atomic relaxations.

5.3.2 Work of Adhesion

Our estimates of the ideal work of adhesion ($\mathcal{W}_{\text{ad}}$) were calculated using two different methods. The first is based on the Universal Binding Energy Relation (UBER)[32], and involves calculating the total energy of an unrelaxed interface (formed by joining truncated bulk surfaces) as the interfacial separation is incrementally reduced from an initial value of 8Å. The *ab initio* data is then fit to the UBER function, yielding the optimal $\mathcal{W}_{\text{ad}}$ and interfacial separation, d_0 (see Fig. 3.2). The optimal geometries from the UBER calculations were then used to begin a second series of calculations in which the structure of each interface and its isolated slabs were optimized via minimization of the atomic forces to a tolerance of 0.05 eV/Å. (For those supercells having the V- or N/C-site stacking, all atomic relaxations were along a direction perpendicular to the interface due to symmetry, and all in-plane forces were equal to zero. Structures with the bridge-site stacking were constrained to allow relaxations perpendicular to the interface only.) To facilitate cancelation of errors across the different interface models and interface vs. surface calculations, the same supercell

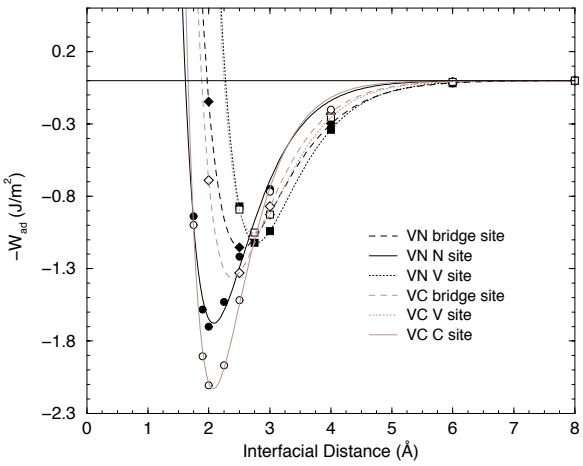

Figure 5.5: Universal Binding Energy curves for the Al/VN and Al/VC interface geometries.

dimensions and $\mathbf{k}$-points were used whenever possible.

Table 5.3 summarizes the optimal d_0 and $\mathcal{W}_{\rm ad}$ values for all six interface structures, including both the unrelaxed (UBER) and relaxed geometries. We see that the interfaces with the Al atoms placed above the metalloid atoms exhibit the largest $\mathcal{W}_{\rm ad}$ values for both ceramics: 1.73 J/m^2 for Al/VN and 2.14 J/m^2 for Al/VC. Bonding at the V-site is weakest, and is similar (0.91-0.96 J/m^2) for both systems. Intermediate to these two extremes is the bridge site, in which only partial Al–metalloid bonds form. The preference for the metalloid adhesion site is consistent with earlier adhesion studies[25, 33, 42] involving interfaces of MgO(100) (which also has the rock-salt structure) with Ti, Ag, and Al.

In the LDA-LCAO study from Ref. [33], Hong and co-workers noticed that the difference in $\mathcal{W}_{\rm ad}$ between Al/MgO and Ag/MgO correlated with the difference in the surface energies of the metals. This behavior is also evident in the LDA, LMTO results of Schönberger *et al*, who considered the Ti/MgO and Ag/MgO systems. In the present case we observe the same behavior, only applied to the surface energies of the ceramics. Specifically, the largest $\mathcal{W}_{\rm ad}$ value occurs for the interface containing the ceramic with the largest surface energy: VC. Moreover, the difference in $\mathcal{W}_{\rm ad}$ between the VC and VN interfaces is roughly 0.4 J/m^2, for both the metalloid and bridge sites. This is similar to the difference in ceramic surface energies of 0.32 J/m^2.

The relatively small $\mathcal{W}_{\rm ad}$ values (1.7, 2.1 J/m^2) calculated herein are in reasonable qualitative agreement with those of Refs. [42] and [33], which range from 2.2 J/m^2 for Ti/MgO down to 1.6-1.9 J/m^2 for Ag/MgO. (However, a direct comparison between these results is not recommended due to differences in computational details such basis sets and exchange-correlation functionals.) The agreement is likely due more to the geometry of the ceramic surfaces rather than the details of the individual metal–ceramic interactions. Namely, the (100) face of rocksalt-type crystals is a non-polar surface with equal numbers of cations and anions within each layer parallel to the interface. The layers are therefore charge neutral, and exhibit smaller surface energies than their polar counterparts. Since smaller surface energies generally indicate a less reactive surface, these non-polar geometries tend to adhere weakly when interfaced with another surface. We

Ceramic	Stacking	Unrelaxed $\mathbf{d_0}$ (Å)	Unrelaxed $\mathcal{W}_{\mathbf{ad}}$ (Jm^{-2})	Relaxed $\mathbf{d_0}$ (Å)	Relaxed $\mathcal{W}_{\mathbf{ad}}$ (Jm^{-2})
VN	N-site	2.08	1.68	2.11	1.73
	V-site	2.78	1.12	2.80	0.91
	Bridge	2.53	1.16	2.53	0.98
VC	C-site	2.08	2.13	2.13	2.14
	V-site	2.72	1.05	2.73	0.96
	Bridge	2.38	1.36	2.31	1.38

Table 5.3: Unrelaxed and relaxed adhesion energies ($\mathcal{W}_{\text{ad}}$) and interfacial separations ($\mathbf{d_0}$) for the six Al/VN and Al/VC interface systems.

	Avg. Interlayer Dist. (Å), [% of Bulk]	
Interlayer	Al/VN	Al/VC
Al_{2-3}	1.98, [-2.0]	1.95, [-3.5]
Al_{1-2}	2.04, [+1.0]	2.00, [-1.0]
Interface	2.11	2.13
$Ceramic_{1-2}$	2.06, [-0.5]	2.08, [-0.5]
$Ceramic_{2-3}$	2.12, [+2.4]	2.08, [-0.5]
$Ceramic_{3-4}$	2.05, [-1.0]	2.09, [0]

Table 5.4: Interlayer spacing with respect to position perpendicular to the interface, given in terms of absolute distance (Å) and as a percentage of the respective bulk spacing (shown in square brackets). The central layer of the Al slab is denoted Al_3, the interfacial Al layer as Al_1, the central ceramic layer is $Ceramic_4$, *etc*.

have observed similar trends in polar vs. non-polar geometries for other interface systems[163, 190], and in a follow-up study will cast this relationship in a more quantitative context[164].

In general, there is good agreement between the unrelaxed UBER and relaxed $\mathcal{W}_{\text{ad}}$ and d_0 values. In allowing for relaxation, interfacial distances change by less than 0.05 Å, and $\mathcal{W}_{\text{ad}}$ is altered by about 0.2 J/m^2 at most. Similar agreement was observed in our earlier study[190] of the Al/WC interface, in which only minor amounts of atomic relaxation were present. However, significant differences between UBER and relaxed $\mathcal{W}_{\text{ad}}$ values have been noted for systems which undergo substantial relaxation[163].

Table 5.4 shows that allowing for interfacial atomic relaxation results in only small changes to the average interlayer distances (3.5% or less of the respective bulk spacings). In Al, three of the four interlayer distances undergo contraction, presumably in an effort to counteract the lateral tensile strain incurred by matching to the larger ceramic surface cells. In both VN and VC the first interlayer contracts by 0.5%, which is slightly less than what is found for the free surfaces: 1.7% and 1.4%, respectively. However, the degree of rumpling of the ceramic interfacial layer in both systems is nearly identical to that found for the surfaces. In Al/VN the N atom relaxes towards the Al slab, while the V atom contracts slightly deeper into the VN bulk region, resulting in a N–V distance of 0.32 Å. At the surface these atoms are separated by 0.27 Å. In Al/VC the C–N distance is 0.21 Å and in the surface it is 0.18Å.

In summary, we find relatively small $\mathcal{W}_{\text{ad}}$ values for both Al/VN and Al/VC interfaces, consistent with the non-polar nature of the rocksalt (100) surface and with earlier studies of metal/MgO adhesion. The

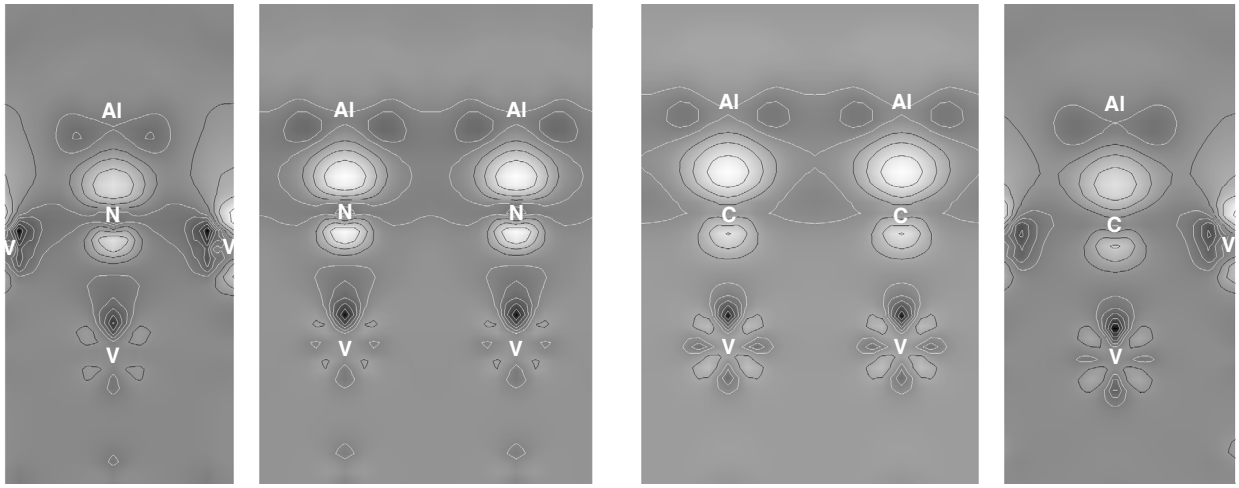

(a) Al–VN(011) (b) Al–VN(001) (c) Al–VC(001) (d) Al–VC(011)

Figure 5.6: Charge density difference (relative to the isolated surfaces) for the Al/VN and Al/VC interfaces taken along the (011) and (001) directions. The color scheme is the same as in Fig. 5.3, and the interfacial atoms intersected by the slice plane are labeled.

magnitude of the difference in $\mathcal{W}_{\rm ad}$ and its rank-ordering for Al/VN vs. Al/VC can be roughly understood in terms of the differences in the surface energies of the respective ceramics.

5.3.3 Electronic Structure

To reveal the nature of the interfacial bonding between the metal and ceramic, Figs. 5.6-5.8 depict the interfacial charge density difference, its planar average along $\langle 100 \rangle$, and the layer-projected DOS, respectively, for the relaxed Al/VN and Al/VC interfaces using the optimal metal-on-metalloid stacking sequence. The difference charge density was evaluated with respect to the isolated slabs according to the relation:

$$\rho(\boldsymbol{r})_{\rm interface} - \left[\rho(\boldsymbol{r})_{\rm Al(100)} + \rho(\boldsymbol{r})_{\rm VN/VC(100)}\right], \tag{5.2}$$

and is visualized in Fig. 5.6 using the same grey-scale scheme used in Fig. 5.3. Two slices along (011) and (001) are shown for each interface, and those atoms intersected by the slicing planes are identified.

Since the electronic structure of the bulk ceramics are closely related, it should come as no surprise that there are several features of the interfacial electronic structure common to both systems. First of all, Fig. 5.6 shows that the interfacial charge re-distribution is a localized effect, being confined to the first Al layer, and to within the second layer in the ceramics. This conclusion is supported by the DOS plot of Fig. 5.8, where the sub-interface DOS are similar to their values in the center of their respective slabs. Secondly, there are extended regions of charge depletion in the interstitial regions of the interfacial Al layer, as can be seen both in Figs. 5.6 and 5.7. This signals a reduction in lateral Al–Al metallic bonding in favor of forming new bonds across the interface. Likewise, Fig. 5.6 shows that lateral bonding in the ceramic interfacial layer also

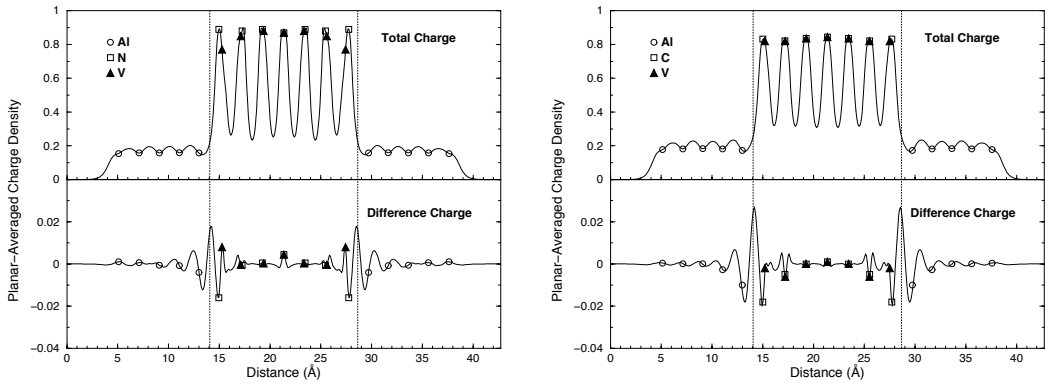

(a) Al/VN

(b) Al/VC

Figure 5.7: Planar-averaged total charge and charge density difference (relative to the isolated surfaces) for the Al-above-metalloid geometries along a direction normal to the interfaces. The location of the interfaces is given by dotted vertical lines.

weakens, as seen by the reduction in V d-charge in panels 5.6(a) and 5.6(d).

The dominant metal–ceramic bonding mechanism appears to be a covalent Al–N (or Al–C) σ-type bond. The bonds can be clearly seen in Fig. 5.6 as the roughly spherical regions of charge accumulation along the Al–metalloid bond direction. In addition, the lower panels of Fig. 5.7 show that this charge is peaked slightly closer to the metalloid atom than to the Al, consistent with differences in electronegativity between Al and C/N. The different magnitudes of the planar-averaged charge accumulation at the interface in Fig. 5.7 also explains the observed differences in the magnitudes of $\mathcal{W}_{\rm ad}$: the larger peak in the Al–C bond charge illustrates that more charge accumulates there than in the weaker Al–N bonds of Al/VN. The DOS from Fig. 5.8 shows that in Al/VN the bonding is likely due to hybridization of the Al 3sp states with the N 2s band in the -17 to -15 eV range. For Al/VC the same type of overlap occurs, except that it now involves the C 2s within the -14 to -10 eV range.

To summarize, we find that the dominant interfacial bonding mechanism is the essentially the same for both systems, and involves a covalent Al 3sp–N/C 2s σ-type interaction. The larger $\mathcal{W}_{\rm ad}$ of Al/VC can be explained by the relatively higher charge density (as compared to Al/VN) within the bond orbital.

5.4 Summary and Conclusions

We have performed a GGA-DFT study of the adhesion, structure, and bonding of the Al/VN and Al/VC interfaces in order to determine the importance of the ceramic's metalloid component on interfacial properties. We find that for both systems the preferred stacking sequence places the Al atoms above the metalloid sites, consistent with earlier studies of metal/MgO interfaces. $\mathcal{W}_{\rm ad}$ values were calculated to be 1.73 J/m^2 for Al/VN and 2.14 J/m^2 for Al/VC. The larger $\mathcal{W}_{\rm ad}$ value for Al/VC can be attributed to the higher surface energy of VC(100), indicative of a more reactive surface and greater preference for bond formation. In ad-

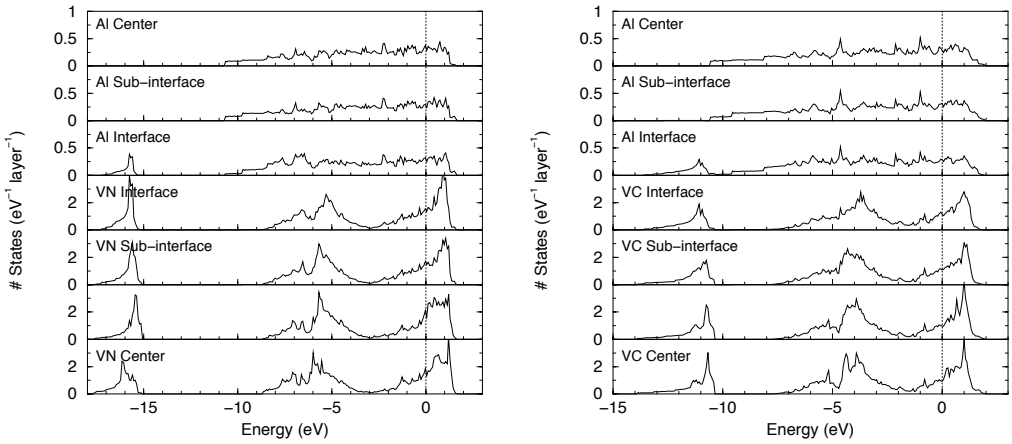

(a) Al/VN (b) Al/VC

Figure 5.8: Layer-projected DOS for the Al/VN and Al/VC interfaces, using the optimal (Al-above-metalloid) stacking sequence.

dition, the difference in $\mathcal{W}_{\text{ad}}$ was found to be roughly the same size as the difference in the ceramic surface energies, further suggesting a dependence of interfacial properties upon those of its underlying surfaces. An analysis of the interfacial electronic structure revealed that both systems form covalent Al–N/C σ-type bonds. The Al–C bond orbital exhibited a greater concentration of charge, in agreement with that interface's larger $\mathcal{W}_{\text{ad}}$.

Chapter 6

Trends in Metal–Ceramic Adhesion

Interfaces between metals and ceramics play a vital role in many industrial applications[7]: heterogeneous catalysis, microelectronics, thermal barriers, corrosion protection, and metals processing are but a few representative examples. Nonetheless, experimental complications associated with the study of a buried interface, and theoretical difficulties arising from complex interfacial bonding interactions have hindered the development of models capable of predicting fundamental interfacial quantities. Recently, advances in *ab initio* simulation techniques and the development of high resolution experimental probes have made interfacial studies more tractable, as evidenced by the appearance of several reports[1, 32, 45–49, 56, 191, 192] addressing the issue of metal–ceramic adhesion[7]. However, with the exception of only one study[1], all of these focused on but one or two particular interface systems. These works have provided valuable insight into the atomic and electronic structure of several different interfaces, but the disparity of methods and approximations used (especially in the context of the *ab initio* calculations) make it difficult to extract meaningful trends across studies performed by different groups.

This chapter reports the first *ab initio* study of the influence of ceramic composition on metal–ceramic interfacial adhesion. By performing a systematic study of 7 different Al/ceramic interfaces (amounting to 20 different interface geometries) wherein the ceramic composition was varied amongst oxides, carbides, and nitrides, we have identified and endeavored to explain a simple trend in adhesion. In essence we have conducted the inverse investigation of Bogicevic and Jennison[1], who considered the adsorption of several metal overlayers on aluminum oxide. In our study the metallic component of the interface was instead held constant.

As discussed in Ch. 1, a fundamental quantity which influences the mechanical properties of an interface is the ideal work of adhesion, $\mathcal{W}_{\rm ad}$[7], which is defined as the energy required to break interfacial bonds and reversibly separate an interface into two free surfaces, neglecting diffusion and plastic deformation. (The degree of plastic deformation which occurs during interfacial fracture is known to depend upon $\mathcal{W}_{\rm ad}$[8].) Formally, $\mathcal{W}_{\rm ad}$ is defined either in terms of the surface and interfacial energies (relative to the respective bulk materials) or by the difference in total energy between the interface and its isolated surfaces:

$$\mathcal{W}_{\rm ad} = \sigma_{1v} + \sigma_{2v} - \gamma_{12} = \left(E_1^{\rm tot} + E_2^{\rm tot} - E_{12}^{\rm tot}\right)/A. \tag{6.1}$$

System	a(Å)	c (Å)	B_0 (GPa)	E_{coh} (eV)
Al	4.039		73.5	3.51
	4.03[a]		79.4[b]	3.39[c]
α–Al_2O_3	4.792	13.077	246	33.0
	4.763[d]	12.98[d]	253[e]	31.8[f]
WC	2.920	2.840	375	16.7
	2.904[g]	2.835[g]	443[g]	16.7[h]
VN	4.132		316	12.2
	4.126[i]		-	12.5[j]
VC	4.170		304	13.9
	4.172[i]		-	13.9[j]

[a] Ref. [128]
[b] Ref. [129]
[c] Ref. [69]
[d] Refs. [135, 136]
[e] Ref. [137]
[f] Ref. [138]
[g] Ref. [193]
[h] Ref. [165]
[i] Ref. [185]
[j] Ref. [186]

Table 6.1: Comparison of calculated bulk properties with experiment. Experimental data is listed in the second row for each material.

Here σ_{iv} is the surface energy of slab i, γ_{12} is the interface energy, E_i^{tot} is the total energy of slab i, and E_{12}^{tot} is the total energy of the interface system. The total interface area is given by A.

Although Eq. 6.1 defines $\mathcal{W}_{\text{ad}}$ in terms of both the surface and interfacial energies, it hides the implicit dependence of γ_{12} itself upon the properties of the surfaces. In fact, the strength of the interfacial bonding depends to a large extent upon the *reactivity* of the individual surfaces, as measured by their surface energies. Since large surface energies indicate the presence of energetically unfavorable features such as large surface dipoles and dangling bonds, these surfaces often reconstruct or seek to passify their dangling bonds by bonding to adsorbates or, when possible, other surfaces. In this chapter we illustrate how knowledge of the surface energy (and its implications on surface reactivity) enables the prediction of trends in the strength of interfacial bonding. Specifically, we find that the size of σ correlates with the magnitude of the interfacial adhesion.

To ensure the precision of energies and geometries, separate $\mathbf{k}$-point and planewave cutoff energy convergence tests were performed on all relevant structures: bulk, surfaces, and interfaces. In all cases total energies were converged to within 1-2 meV per atom. As our goal is to simulate interfaces between two bulk-like materials, additional checks were performed to ensure that the slabs comprising each interface were sufficiently thick to exhibit a bulk-like interior (see Table 6.2). More detailed accounts of the pseudopotential implementations and convergence testing can be found in the previous chapters or the relevant papers[163, 190, 194].

Surface	# Layers	$\sigma\ (J\,m^{-2})$
Al(100)	5	0.89
Al(110)	4	1.05
Al(111)	5	0.81
α–$Al_2O_3(0001)^{Al}$	15	1.59
α–$Al_2O_3(0001)^{O}$	13	7.64, (4.45-10.83)
$WC(0001)^{W}$	9	3.66, (3.43-3.88)
$WC(0001)^{C}$	9	5.92, (5.69-6.14)
$WC(11\bar{2}0)$	4	3.88
VN(100)	7	0.95
VC(100)	7	1.28

Table 6.2: Calculated surface energies, σ. Also, slab dimensions (given in # of atomic layers) used in the interface calculations. For the non-stoichiometric surfaces both the average σ and the range of possible σ are given. Superscripts give the termination of those surfaces cleaved along a polar plane.

Interface	Orientation	Polarity	Strain (%)	$\mathcal{W}_{ad}\ (J\,m^{-2})$
Al/α–$Al_2O_3{}^{Al}$	$(111)[\bar{1}10]_{Al} \parallel (0001)[10\bar{1}0]_{Al_2O_3}$	NP	4.9	1.06
Al/α–$Al_2O_3{}^{O}$	$(111)[\bar{1}10]_{Al} \parallel (0001)[10\bar{1}0]_{Al_2O_3}$	P	4.9	9.73
Al/WC^{W}	$(111)[\bar{1}10]_{Al} \parallel (0001)[11\bar{2}0]_{WC}$	P	2.2	4.08
Al/WC^{C}	$(111)[\bar{1}10]_{Al} \parallel (0001)[11\bar{2}0]_{WC}$	P	2.2	6.01
Al/WC	$(110)[1\bar{1}0]_{Al} \parallel (11\bar{2}0)[0001]_{WC}$	NP	0.4	3.14
Al/VN	$(100)[001]_{Al} \parallel (100)[001]_{VN}$	NP	2.3	1.73
Al/VC	$(100)[001]_{Al} \parallel (100)[001]_{VC}$	NP	3.2	2.14

Table 6.3: Interfacial orientation relationship, polarity (P = polar, NP = non-polar), strain, and $\mathcal{W}_{ad}$ for the interfaces under consideration. Where necessary, the terminations of some of the ceramics are indicated by a superscript.

The accuracy of the pseudopotential approximation was assessed by performing a series of calculations on the bulk phases of all materials used in this study. The results of these calculations are compiled in Table 6.1 and compared with available experimental data. Consistent with other state-of-the-art GGA-DFT studies, we find excellent agreement with experiment: lattice geometries agree to within 1%, bulk moduli to within 10-15%, and cohesive energies to within 5%.

In order to accurately evaluate surface energies (see Table 6.2) we followed the method proposed by Boettger[133], which avoids the problem of non-convergence of σ with respect to slab thickness. Large slabs of up to 15 atomic layers were used. For the polar systems (α–$Al_2O_3(0001)^{O}$, $WC(0001)^{W}$, and $WC(0001)^{C}$) this method is not applicable because a non-stoichiometric slab must be implemented to allow for identical termination of both surfaces. In those cases it is only possible to calculate the surface energy to within a range determined by the requirement that the chemical potentials of the elements in the compound μ_i are less than those of the pure elements in their standard states (ss): $\mu_i \leq \mu_i^{ss}$ (see Ch. 4 or Refs. [178, 190, 195] for more details). The average of σ over this range is reported in Table 6.2 and was then used in relating

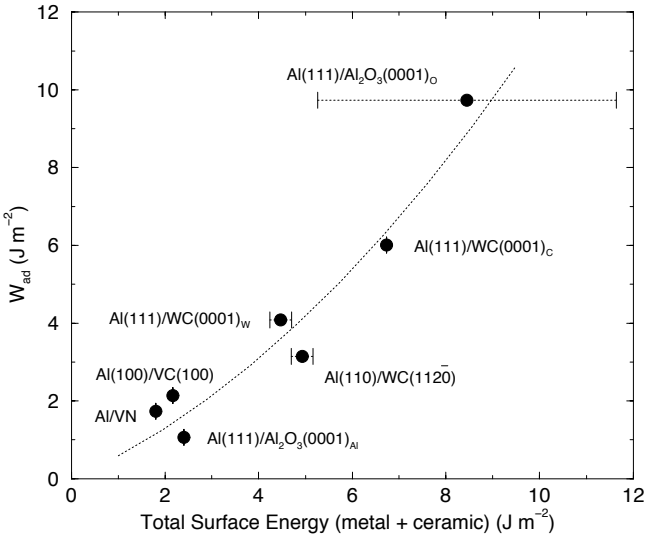

Figure 6.1: $\mathcal{W}_{\rm ad}$ vs. the summed surface energies ($\sigma_{\rm Al} + \sigma_{\rm ceramic}$). Each data point refers to the most favorable stacking sequence for a given interface termination, and horizontal error bars give the range of possible surface energies for those systems containing non-stoichiometric compounds.

$\mathcal{W}_{\rm ad}$ to σ. We note that of the 10 σ's reported in that Table, three of the four largest belong to polar surfaces, in which cleaving the surface requires the breaking of strong anion–cation bonds. (All of α–Al_2O_3, WC, VN, and VC exhibit some degree of ionic bonding.) The remaining six non-polar surfaces have relatively small surface energies: $\sigma \leq 1.6\,{\rm J\,m^{-2}}$.

It should be pointed out that the large surface energies exhibited by some of the polar surfaces (in particular α–$Al_2O_3(0001)^{\rm O}$ and $WC(0001)^{\rm C}$) indicate that these surfaces are unlikely to exist under equilibrium conditions without undergoing a reconstruction or relaxation process (by which they could lower their surface energies). It is debatable whether such structures could be created under *non*-equilibrium conditions. For example, an α–$Al_2O_3(0001)^{\rm O}$ surface could be possible by applying a large partial pressure of O_2 gas or ozone over an Al-terminated surface in UHV. In any event, our purpose here is not so much to make direct comparisions to experiment, but rather to establish trends based on model systems.

Our interface models used a superlattice geometry in which a central ceramic slab was sandwiched between two slabs of Al, resulting in two identical interfaces per supercell. When possible, orientation relationships from experiment[102] were used (see Table 6.3 for a complete listing). A vacuum region of $\sim$ 10Å separated the free surfaces of the Al, thereby preventing interactions between periodic images. The thicknesses of all slabs were carefully checked to ensure a bulk-like interior; the number of atomic layers used in the interface calculations are listed in Table 6.2. To accommodate the periodic boundary conditions, all but one interface system[1] used the coherent interface approximation in which the softer Al slabs were compressed or stretched to match the surface lattice constants of the ceramic. Since it is known

[1]The Al/WC$(11\bar{2}0)$ system has a very low strain % as it contains a misfit: a (4×1) surface of WC$(11\bar{2}0)$ is interfaced to a (5×1) Al(110). Due to the large unit cell necessary for this calculation, a superlattice geometry was not implemented and the interface was formed at only one surface of the WC.

that strain effects can adversely effect the accuracy of a determination of $\mathcal{W}_{ad}$[56], we have purposely selected interfaces with materials that are both industrially relevant and have a modest mismatch of less than 5% with the Al lattice (see Table 6.3). A realistic interface with a mismatch of this magnitude would likely possess large regions of coherency interrupted by widely spaced ($\gtrsim 100$ Å) misfit dislocations; hence our coherent models are a reasonable first approximation to the true structure.

For each interface system several different stacking sequences (i.e., relative translations of the slabs within the plane of the interface) were examined to identify the optimal bond site. In the instance of those ceramic surfaces which were cleaved along polar directions (α–$Al_2O_3(0001)^O$ and $WC(0001)^{W,C}$), both terminations were considered: Al– and O–terminations for α–$Al_2O_3(0001)$ and W– and C–terminations for WC(0001). Additionally, all structures (surfaces and interfaces) were relaxed to a force tolerance of 0.05 eV/Å per atom. To facilitate cancelation of errors, $\mathcal{W}_{ad}$ was calculated by taking the difference in the total energy of a given interface structure with that of its isolated surfaces, using the same supercell dimensions and $\mathbf{k}$-point sampling.

The results of our $\mathcal{W}_{ad}$ calculations are presented in Table 6.3. There one can see that there are substantial differences in $\mathcal{W}_{ad}$ for the polar vs. non-polar geometries. In particular, the three polar surfaces yield the largest adhesion energies, ranging from 4.08 J m^{-2} for Al/WC^W up to 9.73 J m^{-2} for Al/α–$Al_2O_3{}^O$. Of the remaining four (non-polar) interfaces, three have $\mathcal{W}_{ad}$ values of 2.1 J m^{-2} or less. On average, the polar $\mathcal{W}_{ad}$'s are 4.6 J m^{-2} larger than the non-polar systems, consistent with their larger surface energies. We note that our predicted $\mathcal{W}_{ad}$ value of 1.06 J m^{-2} for Al/α–$Al_2O_3{}^{Al}$ compares favorably with the experimental value of 1.13 J m^{-2}[21] as scaled to 0 K. However, we are not aware of additional experimental data to compare with our other values. Regarding the optimal interfacial stacking sequences, we find that for the Al/α–Al_2O_3 and polar Al/WC systems the metal atoms prefer sites which continue the natural stacking sequence of the bulk ceramic across the interface and into the Al. For Al/VC, Al/VN, and Al/WC$(11\bar{2}0)$, the Al atoms prefer to sit above the metalloid atoms (C and N). For more details regarding the adhesion, structure, and bonding of these interfaces see Ch. 3-5 or our previous papers[163, 190, 194].

Fig. 6.1 illustrates the key result of this study: a trend in $\mathcal{W}_{ad}$ vs. the sum of the metal and ceramic surface energies ($\sigma_{Al} + \sigma_{ceramic}$) comprising a given interface. Specifically, we find that interfaces built from surfaces with large σ's have larger $\mathcal{W}_{ad}$'s than those containing surfaces with small σ's. In the Figure the ordinate gives $\mathcal{W}_{ad}$ for the optimal stacking sequence of each interface system, which are labeled adjacent to the data points. For the three interfaces containing non-stoichiometric ceramic compounds the data are bracketed by horizontal error bars giving the range of possible σ. To our knowledge, this is the first report of a trend in metal–ceramic adhesion from a first-principles calculation arising from the influence of the ceramic interfacial component. The fact that *any* trend exists at all is somewhat surprising considering the large disparities in electronic structure between the ceramics and the different bonding mechanisms at the interfaces. (For example, α–Al_2O_3 is a wide-bandgap insulator characterized by mainly ionic bonding, while the carbides and nitrides are metallic and possess elements of metallic, covalent, and ionic bonding. In the interfaces, bonding ranges from strongly ionic in Al/α–$Al_2O_3{}^O$ to weakly covalent in Al/VC and Al/VN.) Nonetheless, the correlation in $\mathcal{W}_{ad}$ and σ seems intuitive when if one considers that σ is a measure of surface reactivity, and that surfaces with large σ values tend to reconstruct or form bonds to reduce σ. The

larger the value of σ, the stronger the incentive to find a mechanism by which it can be reduced. Aside from its intuitive appeal, a correlation with σ is also convenient from a practical standpoint in that surface energies are more readily calculated[2] than $\mathcal{W}_{\mathrm{ad}}$, and thus a rough guide to interfacial adhesion can be easily established. More precise estimates of $\mathcal{W}_{\mathrm{ad}}$ could then be made by performing a full interface calculation.

In summary, we have performed a systematic GGA-DFT study aimed at revealing the significance of the ceramic component upon the work of adhesion at metal–ceramic interfaces. A broad class of Al/ceramic systems were considered, including oxides, carbides, and nitrides, as well as different stacking sequences and interface terminations (both polar and non-polar). Despite significant differences in both the interfacial bonding and the inherent electronic structures of the bulk ceramics, we observe a trend in $\mathcal{W}_{\mathrm{ad}}$ with respect to the surface energies of the interfaced materials. Specifically, surfaces having larger σ's adhere at interfaces much more strongly than those with small σ's. We argue that this behavior is consistent with the intuitive notion of the surface energy being a measure of surface reactivity.

[2] In fact σ's for most metallic elements have already been calculated in Ref. [144].

Chapter 7

Conclusions

We have used Density Functional-based simulation methods to achieve two primary goals: (1) To calculate the work of adhesion, electronic structure, and atomic geometry for a broad class metal–ceramic interfaces; (2) Using those calculations, we identified a trend in $\mathcal{W}_{\text{ad}}$ with respect to the surface energies of the interfaced materials, thereby facilitating predictions of adhesion for other metal–ceramic systems. Below we summarize the results from each phase of this study.

7.1 Survey of Metal–Ceramic Interfaces

In Chapter 3 we began our investigation of interfacial properties by considering the Al(111)/α–Al_2O_3(0001) system. Six candidate interfaces were studied, including Al– and O–terminations and three distinct stacking sequences. We find that, regardless of termination, the optimal interface geometry placed the metal atoms above the O hole sites in the alumina. Optimization of the atomic geometry produced substantial atomic displacements in the metal near the interface, wherein some atoms were pulled towards the oxide and assume positions which would normally be occupied by the Al^{3+} cations in the bulk crystal. The subsumed atoms are arranged such that they effectively terminate the oxide with a bilayer of Al, *independent* of its initial termination. The electronic structure of these atoms was found to resemble those of the alumina's cations.

The calculated adhesion energies of 1.36 J/m^2 (LDA) and 1.06 J/m^2 (GGA) for the relaxed FCC-Al interface were in good agreement with the experimental value of 1.13 J/m^2, and suggest that an Al–terminated interface is the most physically realistic structure for low partial pressures of O_2 gas. For the FCC-O interface these values were roughly an order of magnitude larger, 10.7 J/m^2 and 9.73 J/m^2, respectively.

In terms of the electronic structure, we determined that the interfacial Al–O bonds in both systems were very similar to the cation-anion bonds found in bulk alumina, and were therefore mainly ionic with a smaller degree of covalency. In the O–terminated interface this ionic interaction is the dominant bonding mechanism, and it is responsible for the large adhesion energies. By analyzing the Mulliken charges we determined that there is twice as much charge transfer to the oxide in the O–terminated interface relative to the Al–termination, and that the charge state of the subsumed atoms is similar to the cation charges found in the bulk oxide.

In Chapter 4 we discussed the Al(111)/WC(0001) interface, presenting one of the first studies of metal–

ceramic adhesion involving a transition metal carbide. We found that both the clean WC surface and interface are W-terminated, as these structures have the lowest surface and interfacial free energies. Overall, interface adhesion was relatively strong, with the optimal C– and W–terminations yielding W_{ad} values of 6.01 and 4.08 J/m^2, respectively. Those values were explained in terms of the large surface energies obtained for the polar surfaces. By cleaving along (0001) one creates a very reactive surface by breaking cation-anion bonds, and leaving behind a terminating layer with a large surface dipole and reactive dangling bonds. The optimal adhesion site for both terminations placed the interfacial metal atoms in the HCP site with respect to the carbide stacking sequence. This geometry effectively continues the carbide crystal structure into the metal, an effect which was also seen for the Al/α–Al_2O_3 system.

The calculated W_{ad} values can be further understood by the differences in the electronic structure of the two interfacial terminations. The W-HCP system was characterized by a mixture of metallic/covalent bonding, whereas the stronger bound C-HCP interface exhibited ionic/covalent interactions, with charge transfer to the interfacial C layer.

In the last part of that chapter we considered the effects of Li and Mg alloying agents on W_{ad}. Consistent with their large size, we find that both reduce W_{ad} by 1.5–2.5 J/m^2, and push both interface terminations apart, suggesting that strain effects are important. However, electronic effects were also significant, as the *smaller* Li impurities generate a *larger* reduction to W_{ad}—a result which cannot be explained in terms of strain effects alone.

In order to determine the importance of the ceramic's metalloid component on interfacial properties, the related Al/VN and Al/VC interfaces were investigated in Chapter 5. We found that for both systems the preferred stacking sequence places the Al atoms above the metalloid sites, consistent with earlier studies of metal/MgO interfaces. W_{ad} values were calculated to be 1.73 J/m^2 for Al/VN and 2.14 J/m^2 for Al/VC. The larger W_{ad} value for Al/VC can be attributed to the higher surface energy of VC(100), indicative of a more reactive surface and greater preference for bond formation. In addition, the difference in W_{ad} was found to be roughly the same size as the difference in the ceramic surface energies, further suggesting a dependence of interfacial properties upon those of its underlying surfaces. An analysis of the interfacial electronic structure revealed that both systems form covalent Al–N/C σ-type bonds. The Al–C bond orbital exhibited a greater concentration of charge, in agreement with that interface's larger W_{ad}.

7.2 Trends in Adhesion from First-Principles Simulation

In the final chapter of results, Chapter 6, we showed a trend in W_{ad} with respect to the surface energies of the interfaced materials, despite significant differences in both the interfacial bonding (as shown in Chapters 3-5) and the inherent electronic structures of the bulk ceramics. Specifically, surfaces having larger σ's adhere at interfaces much more strongly than those with small σ's. We argued that this behavior was consistent with the intuitive notion of the surface energy being a measure of surface reactivity, and could perhaps be a feature shared by any general combination of interfaced media.

In conclusion, we have presented the first systematic GGA-DFT study of metal–ceramic adhesion aimed at uncovering the importance of the ceramic interfacial component.

7.3 Extensions

There are several ways this work could be further extended. The most obvious choice would be to simulate other interfaces involving additional materials. In particular, the magnetic transition metal oxides have yet to be considered in the context of an interface. Secondly, in this study we have only treated the effects of interfacial impurities or alloying agents in the most rudimentary fashion, and for only one particular interface system (Al/WC). A more realistic model would include impurity concentrations at fractional monolayer coverages (likely requiring a larger unit cell), rather than at the monolayer coverage considered here, and do so for several interface systems. For the majority of our studies the effects of misfit effects were omitted; however, most realistic interfaces are either incoherent or semi-coherent. A third avenue of study would therefore involve including these misfit effects in a manner similar to that done in Refs. [49] and [56]. Finally, DFT has recently been used to calculate the ideal shear strength of bulk crystals, thus providing an upper bound to the strength of a real material[196]. It would be interesting to extend this bulk methodology in order to estimate the analogous ideal strength of an interface.

References

[1] A. Bogicevic and D. R. Jennison, *Variations in the nature of metal adsorption on ultrathin Al_2O_3 films*, Phys. Rev. Lett. **82**, 799 (1999).

[2] I. Batyrev and L. Kleinman, *Ab-initio simulation of relaxation and adhesion of Cu(111) and Al(111)/$\alpha - Al_2O_3$ (0001) interfaces*, Bull. Am. Phys. Soc. **46**, L15.001 (2001).

[3] T. D. de la Rubia and V. V. Bulatov, *Materials reserach by means of multiscale computer simulation*, MRS Bull. **26**, 169 (2001).

[4] E. Rabinowicz, *Friction and Wear of Materials*, John Wiley and Sons, New York (1995).

[5] D. Turnbull, *Impurities and Imperfections*, Am. Soc. for Metals, Cleveland, OH (1955).

[6] A. R. Miedema and F. J. A. den Broeder, *On the interfacial energy in solid-liquid and solid-liquid metal combinations*, Z. Metallk. **70**, 14 (1979).

[7] M. W. Finnis, *The theory of metal-ceramic interfaces*, J. Phys: Cond. Mat. **8**, 5811 (1996).

[8] D. M. Lipkin, D. R. Clarke, and A. G. Evans, *Effect of interfacial carbon on adhesion and toughness of gold-sapphire interfaces*, Acta mater. **46**, 4835 (1998).

[9] M. D. Kriese, N. R. Moody, and W. W. Gerberich, *Effects of annealing and interlayers on the adhesion energy of copper thin films to SiO2/Si substrates*, Acta mater. **46**, 6311 (1998).

[10] J. R. Rice, *An examination of the fracture mechanics energy balance from the point of view of continuum mechanics*, in T. Yokobori, T. Kawasaki, and J. L. Swedlow, editors, *Proceedings of the 1st International Conference on Fracture*, pp. 309–340, Sendai, Japan (1966).

[11] A. P. Tomsia, E. Saiz, B. J. Dalgleish, and R. M. Cannon, in *Proc. 4th Japan Int. SAMPE Symp. and Exposition*, Tokyo (1995), invited keynote lecture.

[12] T. Young, Trans. Royal Soc., London **94**, 65 (1805).

[13] N. Eustathopoulos, M. G. Nicholas, and B. Drevet, *Wettability at High Temperatures*, Pergamon, Amsterdam (1999).

[14] J. V. Naidich, *The wettability of solids by liquid metals*, Prog. in Surf. Membrane Sci. **14**, 353 (1981).

[15] J. M. Howe, *Bonding, structure, and properties of metal/ceramic interfaces: Part 1. chemical bonding, chemical reaction, and interfacial structure*, Int. Mater. Rev. **38**, 233 (1993).

[16] M. Humenik and W. D. Kingery, J. Am. Ceram. Soc. **37**, 18 (1954).

[17] J.-G. Li, *Wetting and interfacial bonding of metals with ionocovalent oxides*, J. Am. Ceram. Soc. **75**, 3118 (1992).

[18] R. G. Barrera and C. B. Duke, *Dielectric continuum theory of the electronic structure of interfaces*, Phys. Rev. B **13**, 4477 (1976).

[19] A. M. Stoneham, M. M. D. Ramos, and A. P. Sutton, *How do they stick together? the statics and dynamics of interfaces*, Phil. Mag. A **67**, 797 (1993).

[20] P. Xiao and B. Derby, *Wetting of TiN and TiC by liquid metals*, Acta. mater. **44**, 307 (1996).

[21] D. M. Lipkin, J. N. Israelachvili, and D. R. Clarke, *Estimating the metal-ceramic van der waals adhesion energy*, Philos. Mag. A **76**, 715 (1997).

[22] P. Hohenberg and W. Kohn, *Inhomogeneous electron gas*, Phys. Rev. **136**, B864 (1964).

[23] W. Kohn and L. J. Sham, *Self-consistent equations including exchange and correlation effects*, Phys. Rev. **140**, A1133 (1965).

[24] M. C. Payne, M. P. Teter, D. C. Allan, T. A. Arias, and J. D. Joannopoulos, *Iterative minimization techniques for ab initio total-energy calculations: Molecular dynamics and conjugate gradients*, Rev. Mod. Phys. **64**, 1045 (1992).

[25] C. Li, R. Wu, A. J. Freeman, and C. L. Fu, *Energetics, bonding mechanism, and electronic structure of metal–ceramic interfaces: Ag/MgO(001)*, Phys. Rev. B **48**, 8317 (1993).

[26] D. J. Singh, *Planewaves, pseudopotentials, and the LAPW method*, Boston, Kluwer Academic (1994).

[27] F. Rao, R. Wu, and A. J. Freeman, *Structure and bonding at metal-ceramic interfaces: Ag/CdO(001)*, Phys. Rev. B **51**, 10052 (1995).

[28] C. Li and A. J. Freeman, *Giant monolayer magnetization of fe on MgO: A nearly ideal two-dimensional magnetic system*, Phys. Rev. B **43**, 780 (1991).

[29] R. Wu and A. J. Freeman, *Predicted c(2 x 2) buckling reconstruction of monolayer Mn on Fe(001) and its importance to the interfacial magnetic ordering*, Phys. Rev. B **51**, 17131 (1995).

[30] J. R. Smith, J. G. Gay, and F. J. Arlinghaus, *Self-consistent local-orbital method for calculating surface electronic structure: Application to Cu (100)*, Phys. Rev. B **21**, 2201 (1980).

[31] T. Hong, J. R. Smith, and D. J. Srolovitz, *Metal/ceramic adhesion: A first principles study of MgO/Al and MgO/Ag*, J. Adhesion Sci. Technol. **8**, 837 (1994).

[32] J. R. Smith, T. Hong, and D. J. Srolovitz, *Metal-ceramic adhesion and the harris functional*, Phys. Rev. Lett. **72**, 4021 (1994).

[33] T. Hong, J. R. Smith, and D. J. Srolovitz, *Theory of metal-ceramic adhesion*, Acta. Metall. Mater. **43**, 2721 (1995).

[34] A. Banerjea and J. R. Smith, *Origins of the universal binding-energy relation*, Phys. Rev. B **37**, 6632 (1988).

[35] P. Vinet, J. H. Rose, J. Ferrante, and J. R. Smith, *Universal features of the equation of state of solids*, J. Phys. **1**, 1941 (1989).

[36] M. W. Finnis, *The harris functional applied to surface and vacancy formation energies in Aluminium*, J. Phys: Cond. Mat. **2**, 331 (1990).

[37] A. J. Read and R. J. Needs, *Tests of the harris energy functional*, J. Phys: Cond. Mat. **1**, 7565 (1989).

[38] T. Hong, J. R. Smith, and D. J. Srolovitz, *Impurity effects on adhesion: Nb, C, O, B, and S at a Mo/$MoSi_2$ interface*, Phys. Rev. B **47**, 13615 (1993).

[39] T. Hong, J. R. Smith, D. J. Srolovitz, J. G. Gay, and R. Richter, *Determining ab initio interfacial energetics*, Phys. Rev. B **45**, 8775 (1992).

[40] T. Hong, J. R. Smith, and D. J. Srolovitz, *Impurity effects on adhesion*, Phys. Rev. Lett. **70**, 615 (1993).

[41] M. Methfessel, C. O. Rodriguez, and O. K. Andersen, *Fast full-potential calculations with a converged basis of atom-centered linear muffin-tin orbitals: Structural and dynamic properties of silicon*, Phys. Rev. B **40**, 2009 (1989).

[42] U. Schönberger, O. K. Andersen, and M. Methfessel, *Bonding at metal–ceramic interfaces: Ab initio density-functional calculations for Ti and Ag on MgO*, Acta metall. mater. **40**, S1 (1992).

[43] M. W. Finnis and C. Kruse, Materials at High Temps. **12**, 189 (1994).

[44] M. W. Finnis, C. Kruse, and U. Schönberger, *Ab initio calculations of metal/ceramic interfaces: what have we learned, what can we learn?*, Nanostructured Mater. **6**, 145 (1995).

[45] I. G. Batirev, A. Alavi, and M. W. Finnis, *First-principles calculations of the ideal cleavage energy of bulk niobium(111)/alpha-alumina(0001) interfaces*, Phys. Rev. Lett. **82**, 1510 (1999).

[46] C. Verdozzi, D. R. Jennison, P. A. Schultz, and M. P. Sears, *Sapphire (0001) surface, clean and with d-metal overlayers*, Phys. Rev. Lett. **82**, 799 (1999).

[47] W. Zhang and J. R. Smith, *Nonstoichiometric interfaces and Al_2O_3 adhesion with Al and Ag*, Phys. Rev. Lett. **85**, 3225 (2000).

[48] Y. F. Zhukovskii, E. A. Kotomin, P. W. M. Jacobs, and A. M. Stoneham, *Ab initio modeling of metal adhesion on oxide surfaces with defects*, Phys. Rev. Lett. **84**, 1256 (2000).

[49] R. Benedek, A. Alavi, D. N. Seidman, L. H. Yang, D. A. Muller, and C. Woodward, *First principles simulation of a ceramic/metal interface with misfit*, Phys. Rev. Lett. **84**, 3362 (2000).

[50] R. Benedek, D. N. Seidman, M. Minkoff, L. H. Yang, and A. Alavi, *Atomic and electronic structure and interatomic potentials at a polar ceramic/metal interface: $\{222\}$ MgO/Cu*, Phys. Rev. B **60**, 16094 (1999).

[51] L. E. Toth, *Transition Metal Carbides and Nitrides*, Academic Press (1971).

[52] P. Alemany, *Metal-ceramic adhesion: Band structure calculations on transition-metal/AlN interfaces*, Surf. Sci. **314**, 114 (1994).

[53] L. Wenchang, Z. Kaiming, and X. Xide, *Adsorption of Aluminum on β-SiC(100) surfaces*, Phys. Rev. B **45**, 11048 (1992).

[54] S. Li, R. J. Arsenault, and P. Jena, *Quantum chemical study of adhesion at the SiC/Al interface*, J. Appl. Phys. **64**, 6246 (1988).

[55] J. Hartford, *Interface energy and electron structure for Fe/VN*, Phys. Rev. B **61**, 2221 (2000).

[56] S. V. Dudiy, J. Hartford, and B. I. Lundqvist, *Nature of metal-ceramic adhesion: Computational experiments with Co on TiC*, Phys. Rev. Lett. **85**, 1898 (2000).

[57] J. Hoekstra and J. Kohyama, *Ab initio calculations of the β-SiC(001)/Al interface*, Phys. Rev. B **57**, 2334 (1998).

[58] S. Ogata and H. Kitagawa, *Ab initio molecular dynamics analysis of AlN/Al interface structure*, J. Japan Inst. Metals **60**, 1079 (1996), translation from Japanese.

[59] P. A. M. Dirac, Proc. Royal Soc., London **123**, 714 (1929).

[60] M. Born and R. Oppenheimer, Ann. Physik. **87**, 457 (1927).

[61] A. Szabo and N. S. Ostlund, *Modern Quantum Chemistry*, Dover, Mineola, NY (1996).

[62] E. H. Lieb, *Thomas-fermi and related theories of atoms and molecules*, Rev. Mod. Phys. **53**, 603 (1981).

[63] R. Car and M. Parrinello, *Unified approach for molecular dynamics and density-functional theory*, Phys. Rev. Lett. **55**, 2471 (1985).

[64] R. O. Jones and O. Gunnarsson, *The density functional formalism, its applications and prospects*, Rev. Mod. Phys. **61**, 689 (1989).

[65] J. P. Perdew and A. Zunger, *Self-interaction correction to density-functional approximations for many-electron systems*, Phys. Rev. B **23**, 5048 (1981).

[66] D. M. Ceperley and B. J. Alder, *Ground state of the electron gas by a stochastic method*, Phys. Rev. Lett. **45**, 566 (1980).

[67] J. P. Perdew and K. Burke, *Comparison shopping for a gradient-corrected density functional*, Int. J. Quant. Chem. **57**, 309 (1996).

[68] P. Pulay, *Ab initio calculation of force constants and equilibrium geometries in polyatomic molecules. i. theory*, Mol. Phys. **17**, 197 (1969).

[69] C. Kittel, *Introduction to Solid State Physics*, John Wiley and Sons, 6 ed. (1986).

[70] P. E. Blöchl, O. Jepsen, and O. K. Andersen, *Improved tetrahedron method for brillouin-zone integrations*, Phys. Rev. B **49**, 16223 (1994).

[71] H. J. Monkhorst and J. D. Pack, *Special points for brillouin-zone integrations*, Phys. Rev. B **13**, 5188 (1976).

[72] W. E. Pickett, *Pseudopotential methods in condensed matter applications*, Comp. Phys. Rep. **9**, 115 (1989).

[73] S. G. Louie, S. Froyen, and M. L. Cohen, *Nonlinear ionic pseudopotentials in spin-density-functional calculations*, Phys. Rev. B **26**, 1738 (1982).

[74] D. Vanderbilt, *Soft self-consistent pseudopotentials in a generalized eigenvalue formalism*, Phys. Rev. B **41**, 7892 (1990).

[75] G. Kresse and J. Hafner, *Norm-conserving and ultrasoft pseudopotentials for first-row adn transition elements*, J. Phys: Cond. Mat. **6**, 8245 (1994).

[76] H. Hellmann, *Einfuhrung in die Quantumchemie*, Deuticke, Leipzig (1937).

[77] R. P. Feynman, *Forces in molecules*, Phys. Rev. **56**, 340 (1939).

[78] M. T. Yin and M. L. Cohen, *Theory of lattice-dynamical properties of solids: Application to Si and Ge*, Phys. Rev. B **26**, 3259 (1982).

[79] W. H. Press, S. A. Teukolsky, W. T. Vetterling, and B. P. Flannery, *Numerical Recipes in Fortran 90: The Art of Parallel Scientific Computing*, Cambridge University Press, 2 ed. (1996).

[80] G. Kresse and J. Furthmüller, *Efficient iterative schemes for ab initio total-energy calculations using a plane-wave basis set*, Phys. Rev. B **54**, 11169 (1996).

[81] A. M. Rappe, K. M. Rabe, E. Kaxiras, and J. D. Joannopoulos, *Optimized pseudopotentials*, Phys. Rev. B **41**, 1227 (1990).

[82] E. Polak, *Computational Methods in Optimization*, Academic, New York (1971).

[83] P. Pulay, *Convergence acceleration of iterative sequences: the case of scf iteration*, Chem. Phys. Lett. **73**, 393 (1980).

[84] C. G. Broyden, Mathematics of Computation **19**, 577 (1965).

[85] D. D. Johnson, *Modified broyden's method for accelerating convergence in self-consistent calculations*, Phys. Rev. B **38**, 12807 (1988).

[86] N. D. Mermin, *Thermal properties of the inhomogeneous electron gas*, Phys. Rev. **137**, A1441 (1965).

[87] M. Methfessel and A. T. Paxton, *High-precision sampling for brillouin-zone integration in metals*, Phys. Rev. B **40**, 3616 (1989).

[88] J. P. Perdew, J. A. Chevary, S. H. Vosko, *et al.*, *Atoms, molecules, solids, and surfaces: Applications of the generalized gradient approximation for exchange and correlation*, Phys. Rev. B **46**, 6671 (1992).

[89] R. Hoffmann, *Solids and Surfaces: A Chemist's View of Bonding in Extended Structures*, Wiley-VCH, new york ed. (1988).

[90] D. Sánchez-Portal, P. Ordejón, E. Artacho, and J. M. Soler, *Density-functional method for very large systems with lcao basis sets*, Int. J. Quantum Chem. **65**, 453 (1997).

[91] I. Mayer, *Charge, bond order, and valence in the ab initio scf theory*, Chem. Phys. Lett. **97**, 270 (1983).

[92] A. Savin, R. Nesper, S. Wengert, and T. F. Fässler, *ELF: The electron localization function*, Angew. Chem. Int. Ed. Engl. **36**, 1808 (1997).

[93] L. D. Santis and R. Resta, *Electron localization at metal surfaces*, Surf. Sci. **450**, 126 (2000).

[94] A. D. Becke and K. E. Edgecombe, *A simple measure of electron localization in atomic and molecular systems*, J. Chem. Phys. **92**, 5397 (1990).

[95] K. Wefers, G. A. Nitowski, and L. F. Weiserman, U.S. Patent 5,126,210 (1992).

[96] P. Lamparter and R. Kniep, *Structure of amorphous Al_2O_3*, Physica B **234**, 234 (1997).

[97] K. Wefers and C. Misra, *Oxides and Hydroxides of Aluminum*, ALCOA Technical Paper No. 19, Revised, ALCOA, Inc. (1987).

[98] A. B. Anderson, S. P. Mehandru, and J. L. Smialek, *Dopant effect of yttrium and the growth of adherence of Alumina on nickel-Aluminum alloys*, J. Electrochem. Soc: Solid State Sci. Tech. **132**, 1695 (1985).

[99] F. H. Streitz and J. W. Mintmire, *Metal/oxide interfaces: An electrostatics-based model*, Composite Interfaces **2**, 473 (1994).

[100] F. H. Streitz and J. W. Mintmire, *Electrostatic potentials for metal-oxide surfaces and interfaces*, Phys. Rev. B **50**, 11996 (1994).

[101] J. E. Angelo and M. I. Baskes, *Interfacial studies using the EAM and MEAM*, Interface Sci. **4**, 47 (1996).

[102] D. L. Medlin, K. F. McCarty, R. Q. Hwang, S. E. Guthrie, and M. I. Baskes, *Orientation relationships in heteroepitaxial Aluminum films on sapphire*, Thin Solid Films **299**, 110 (1997).

[103] M. Vermeersch, R. Sporken, P. Lambin, and R. Caudano, *The Al/Al_2O_3 interface formation as studied by electron spectroscopies*, Surf. Sci. **235**, 5 (1990).

[104] M. Vermeersch, F. Malengreau, R. Sporken, and R. Caudano, *The Aluminum/sapphire interface formation at high temperature: an AES and LEED study*, Surf. Sci. **323**, 175 (1995).

[105] V. E. Puchin, J. D. Gale, A. L. Shluger, E. A. Kotomin, J. Günster, M. Brause, and V. Kempter, *Atomic and electronic structure of the corundum (0001) surface: Comparison with surface spectroscopies*, Surf. Sci. **370**, 190 (1997).

[106] J. Ahn and J. W. Rabalais, *Composition and structure of the Al_2O_3(0001)-(1x1) surface*, Surf. Sci. **388**, 121 (1997).

[107] P. Guenard *et al*., *Determination of the α-Al_2O_3(0001) surface relaxation and termination by measurements of crystal truncation rods*, Surf. Rev. and Lett. **5**, 321 (1997).

[108] J. Toofan and P. R. Watson, *The termination of the alpha-Al_2O_3(0001) surface: A LEED crystallography determination*, Surf. Sci. **401**, 162 (1998).

[109] I. Manassidis, A. D. Vita, and M. J. Gillan, *Structure of the (0001) surface of alpha-Al_2O_3 from first principles calculations*, Surf. Sci. Lett. **285**, L517 (1993).

[110] C. Ruberto, Y. Yourdshahyan, and B. I. Lundqvist, *Surface properties of kappa-alumina(001) and* $(00\bar{1})$, submitted to Phys. Rev. Lett. (2000).

[111] P. D. Tepesch and A. A. Quong, *First-principles calculations of alpha-alumina(0001) surface energies with and without hydrogen*, Phys. Status Solidi B **217**, 377 (2000).

[112] R. D. Felice and J. E. Northrup, *Theory of the clean and hydrogenated Al_2O_3(0001)-(1x1) surfaces*, Phys. Rev. B **60**, 16287 (1999).

[113] X.-G. Wang, A. Chaka, and M. Scheffler, *Effect of the environment on α-Al_2O_3(0001) surface structures*, Phys. Rev. Lett. **84**, 3650 (2000).

[114] D. R. Jennison, C. Verdozzi, P. A. Schultz, and M. P. Sears, *Ab initio structural predictions for ultrathin Al_2O_3 films on metallic substrates*, Phys. Rev. B **59**, R15605 (1999).

[115] J. A. Kelber, C. Niu, K. Shepherd, D. R. Jennison, and A. Bogicevic, *Copper wetting of α-Al_2O_3(0001): Theory and experiment*, Surf. Sci. **446**, 76 (2000).

[116] C. Niu, K. Shepherd, D. Martini, J. A. Kelber, D. R. Jennison, and A. Bogicevic, *Cu interactions with alpha-Al_2O_3(0001): Effects of surface hydroxyl groups vs. dehydroxylation by ar ion sputtering*, Surf. Sci. (2000), in press.

[117] D. R. Jennison and A. Bogicevic, *Ultrathin aluminum oxide films: Al-sublattice structure and the effect of substrate on ad-metal adhesion*, Surf. Sci. (2000), in press.

[118] K. C. Hass, W. F. Schneider, A. Curioni, and W. Andreoni, *The chemisty of water on alumina surfaces: Reaction dynamics from first principles*, Science **282**, 265 (1998).

[119] P. J. Eng, T. P. Trainor, G. E. Brown, Jr., G. A. Waychunas, M. Newville, S. R. Sutton, and M. L. Rivers, *Structure of the hydrated alpha-Al_2O_3(0001) surface*, Science **288**, 1029 (2000).

[120] K. C. Hass, W. F. Schneider, A. Curioni, and W. Andreoni, *First-principles molecular dynamics simulations of h2o on alpha-Al_2O_3(0001)*, J. Phys. Chem. B **104**, 5527 (2000).

[121] L. G. Hector, Jr., G. A. Nitowski, S. M. Opalka, L. Wieserman, D. J. Siegel, H. Yu, and J. B. Adams, *Investigation of vinyl phosphonic acid/hydroxylated alpha-Al_2O_3(0001) reaction enthalpies*, Surf. Sci. (2001), accepted for publication.

[122] M. Gautier, G. Renaud, L. P. Van, B. Villette, M. Pollak, N. Thromat, F. Jollet, and J.-P. Duraud, *alpha-Al_2O_3(0001) surfaces: Atomic and electronic structure*, J. Am. Ceram. Soc. **77**, 323 (1994).

[123] J. Bruley, R. Brydson, H. Müllejans, J. Mayer, G. Gutekunst, W. Mader, D. Knauss, and M. Rühle, *Investigations of the chemistry and bonding at niobium-sapphire interfaces*, J. Mater. Res. **9**, 2574 (1994).

[124] L. Kleinman and D. M. Bylander, *Efficacious form for model pseudopotentials*, Phys. Rev. Lett. **48**, 1425 (1982).

[125] A. Khein, D. J. Singh, and C. J. Umrigar, *All-electron study of gradient corrections to the local-density functional in metallic systems*, Phys. Rev. B **51**, 4105 (1995).

[126] I.-H. Lee and R. M. Martin, *Applications of the generalized-gradient approximation to atoms, clusters, and solids*, Phys. Rev. B **56**, 7197 (1997).

[127] A. D. Corso, A. Pasquarello, A. Baldereschi, and R. Car, *Generalized-gradient approximations to density-functional theory: A comparative study for atoms and solids*, Phys. Rev. B **53**, 1180 (1996).

[128] Y. S. Touloukian, R. K. Kirby, R. E. Taylor, and T. Y. R. Lee, editors, *Thermophysical Properties of Matter*, vol. 12, Plenum, New York (1975).

[129] G. Simmons and H. Wang, *Single Crystal Elastic Constants and Calculated Aggregate Properties: A Handbook*, MIT Press, Cambridge, MA, 2nd ed. (1971).

[130] G. N. Kamm and G. A. Alers, *Low-temperature elastic moduli of Aluminum*, J. Appl. Phys. **35**, 327 (1964).

[131] J. Vallin, M. Mongy, K. Salama, and O. Beckman, *Elastic constants of Aluminum*, J. Appl. Phys. **35**, 1825 (1964).

[132] W. Y. Ching and Y.-N. Xu, *First-principles calculation of electronic, optical, and structural properties of alpha-Al_2O_3*, J. Am. Ceram. Soc. **77**, 404 (1994).

[133] J. C. Boettger, *Nonconvergence of surface energies obtained from thin-film calculations*, Phys. Rev. B **49**, 16798 (1994).

[134] H. d'Amour, D. Schiferl, *et al*., *High-pressure single-crystal structure determinations for ruby up to 90 kbar using an automatic diffractometer*, J. Appl. Phys. **49**, 4411 (1978).

[135] Y. S. Touloukian, R. K. Kirby, R. E. Taylor, and T. Y. R. Lee, editors, *Thermophysical Properties of Matter*, vol. 13, Plenum, New York (1977).

[136] L. W. Finger and R. M. Hazen, *Crystal structure and compression of ruby to 46 kbar*, J. Appl. Phys. **49**, 5823 (1978).

[137] P. Richet, J. Xu, and H. K. Mao, Phys. and Chem. of Minerals **16**, 207 (1988).

[138] R. C. Weast, editor, *CRC Handbook of Chemistry and Physics*, CRC Press, Boca Raton, FL, 67th ed. (1983).

[139] F. D. Murnaghan, *The compressibility of media under extreme pressures*, Proc. Nat. Acad. of Sci. USA **30**, 244 (1944).

[140] J. P. Perdew, K. Burke, and M. Ernzerhof, *Generalized gradient approximation made simple*, Phys. Rev. Lett. **77**, 3865 (1996).

[141] J. C. Boettger, *High-precision, all-electron, full-potential calculation of the equation of state and elastic constants of corundum*, Phys. Rev. B **55**, 750 (1997).

[142] W. G. Wyckoff, editor, *Crystal Structures*, vol. 1-3, Krieger, Malabar, 2nd ed. (1982).

[143] J. Schöchlin, K. P. Bohnen, and K. M. Ho, *Structure and dynamics at the Al(111) surface*, Surf. Sci. **324**, 113 (1995).

[144] L. Vitos, A. V. Ruban, H. L. Skriver, and J. Kollar, *The surface energy of metals*, Surf. Sci. **411**, 186 (1998).

[145] W. R. Tyson and W. A. Miller, *Surface free energies of solid metals: Estimation from liquid surface tension measurements*, Surf. Sci. **62**, 267 (1977).

[146] W. R. Tyson, *Surface energies of solid metals*, Can. Metall. Quarterly **14**, 307 (1975).

[147] V. Fiorentini and M. Methfessel, *Extracting convergent surface energies from slab calculations*, J. Phys: Cond. Mat. **8**, 6525 (1996).

[148] J. Neugebauer and M. Scheffler, *Adsorbate-substrate and adsorbate-adsorbate interactions of Na and K adlayers on Al(111)*, Phys. Rev. B **46**, 16067 (1992).

[149] R. Ramprasad, D. A. Drabold, and J. B. Adams, *Density functional study of chemisorption of oxygen on Al(111)*, in S. M. Yalisove, C. V. Thompson, and D. J. Eaglesham, editors, *Mechansims of Thin Film Evolution*, vol. 317 of *MRS Proceedings Fall 1993* (1994).

[150] H. B. Nielson and D. L. Adams, J. Phys. C **15**, 615 (1982).

[151] J. R. Noonan and H. L. Davis, J. Vac. Sci. Tech. A **8**, 2671 (1990).

[152] D. A. Weirauch, Jr. and P. D. Ownby, *Application of the zisman critical surface tension technique to ceramic surfaces at high temperature*, J. Adhesion Sci. Technol. **13**, 1321 (1999).

[153] J. Schnitker and D. J. Srolovitz, *Misfit effects in adhesion calculations*, Model. Sim. Mat. Sci. Eng. **6**, 153 (1998).

[154] D. Chatain, I. Rivollet, and N. Eustathopoulos, J. Chim. Phys. **83**, 561 (1986).

[155] D. Chatain, I. Rivollet, and N. Eustathopoulos, J. Chim. Phys. **84**, 201 (1987).

[156] B. Silvi and A. Savin, *Classification of chemical bonds based on topological analysis of electron localization functions*, Nature **371**, 683 (1994).

[157] J. K. Burdett and T. A. McCormick, *Electron localization in molecules and solids: The meaning of ELF*, J. Phys. Chem. A **102**, 6366 (1998).

[158] R. S. Mulliken, J. Chem. Phys. **23**, 1833, 2343 (1955).

[159] P. Ordejón, E. Artacho, and J. M. Soler, *Self-consistent order-n density-functional calculations for very large systems*, Phys. Rev. B **53**, 10441 (1996).

[160] A. M. Stoneham, *Systematics of metal-insulator interfacial energies: a new rule for wetting and strong catalyst-support interactions*, Appl. Surf. Sci. **14**, 249 (1983).

[161] D. M. Duffy, J. H. Harding, and A. M. Stoneham, *Atomistic modelling of metal-oxide interfaces with image interactions*, Philos. Mag. A **67**, 865 (1993).

[162] M. W. Finnis, *Metal-ceramic cohesion and the image interaction*, Acta Metall. Mater. **40**, S25 (1992).

[163] D. J. Siegel, L. G. Hector, Jr., and J. B. Adams, *Adhesion, atomic structure, and bonding at the Al(100)/α-Al_2O_3(0001) interface: A first principles study*, Phys. Rev. B (2001), submitted.

[164] D. J. Siegel, L. G. Hector, Jr., and J. B. Adams, *Trends in metal–ceramic adhesion from first-principles*, Phys. Rev. Lett. (2001), submitted.

[165] A. Y. Liu, R. M. Wentzcovitch, and M. L. Cohen, *Structural and electronic properties of WC*, Phys. Rev. B **38**, 9483 (1988).

[166] H. L. Brown, P. E. Armstrong, and C. P. Kempter, J. Chem. Phys. **45**, 547 (1966).

[167] V. P. Zhukov and V. A. Gubanov, *Energy band structure and thermo-mechanical properties of tungsten and tungsten carbides as studied by the LMTO-ASA method*, Solid State Commun. **56**, 51 (1985).

[168] A. Reuss, Z. Angew. Math. Mech. **9**, 55 (1929).

[169] M. Lee and R. S. Gilmore, *Single crystal elastic constants of tungsten monocarbide*, J. Mater. Sci. **17**, 2657 (1982).

[170] W. Voigt, *Lehrbuch der Kristalphysik*, Teubner, Leipzig (1928).

[171] E. K. Storms, *The Refractory Carbides*, Academic, New York (1967).

[172] P. E. Blöchl, *Projector augmented-wave method*, Phys. Rev. B **50**, 17953 (1994).

[173] G. Kresse and D. Joubert, *From ultrasoft pseudopotentials to the projector augmented-wave method*, Phys. Rev. B **59**, 1758 (1999).

[174] R. B. Levy and M. Boudart, Science **181**, 547 (1973).

[175] J. E. Houston, G. E. Laramore, and R. L. Park, *Surface electronic properties of tungsten, tungsten carbide, and platinum*, Science **185**, 258 (1974).

[176] P. M. Stefan, M. L. Shek, I. Lindau, W. E. Spicer, L. I. Johansson, F. Herman, R. V. Kasowski, and G. Brogen, *Photoemission study of WC(0001)*, Phys. Rev. B **29**, 5423 (1984).

[177] L. F. Mattheiss and D. R. Hamann, *Bulk and surface electronic structure of hexagonal WC*, Phys. Rev. B **30**, 1731 (1984).

[178] K. Rapcewicz, B. Chen, B. Yakobson, and J. Bernholc, *Consistent methodology for calculating surface and interface energies*, Phys. Rev. B **57**, 7281 (1998).

[179] I. Batyrev, A. Alavi, and M. W. Finnis, *Ab initio calculations on the Al_2O_3(0001) surface*, Faraday Discuss. **114**, 33 (2000).

[180] W. Zhang and J. R. Smith, *Stoichiometry and adhesion of Nb/Al_2O_3*, Phys. Rev. B **61**, 16883 (2000).

[181] X. Liu, P. Ohotnicky, J. Adams, C. Rohrer, and R. H. Jr., *Anisotropic surface segregation in Al-Mg alloys*, Surf. Sci. **373**, 357 (1997).

[182] X. Y. Liu and J. B. Adams, *Grain boundary segregation in Al-10%Mg alloys at hot working temperatures*, Acta Mater. **46**, 3467 (1998).

[183] C. Stampfl, W. Mannstadt, R. Asahi, and A. J. Freeman, *Electronic strucutre and physical properties of early transition metal mononitrides: Density-functional theory LDA, GGA, and screened-exchange LDA FLAPW calculations*, Phys. Rev. B **63**, 155106 (2001).

[184] J. C. Grossman, A. Mizel, M. Côté, M. L. Cohen, and S. G. Louis, *Transition metals and their carbides and nitrides: Trends in electronic and structural properties*, Phys. Rev. B **60**, 6343 (1999).

[185] P. Villars and L. D. Calvert, editors, *Pearson's Handbook of Crystallographic Data for Intermetallic Phases*, vol. 2,4, ASM International, Materials Park, OH, 2nd ed. (1991).

[186] J. Häglund, G. Grimvall, T. Jarlborg, and A. F. Guillermet, *Band structure and cohesive properties of 3d-transition-metal carbides and nitrides with the NaCl-type structure*, Phys. Rev. B **43**, 14400 (1991).

[187] V. P. Zhukov and V. A. Gubanov, *Study of the energy band structures of TiC, VC, Ti_4C_3 and V_4C_3 by the LMTO-ASA method*, J. Phys. Chem. Solids **48**, 187 (1987).

[188] V. P. Zhukov, V. A. Gubanov, O. Jepsen, N. E. Christensen, and O. K. Andersen, *Calculated energy-band structures and chemical bonding in titanium and vanadium carbides, nitrides, and oxides*, J. Phys. Chem. Solids **49**, 841 (1988).

[189] J. Häglund, A. F. Guillermet, G. Grimvall, and M. Körling, *Theory of bonding in transition-metal carbides and nitrides*, Phys. Rev. B **48**, 11685 (1993).

[190] D. J. Siegel, L. G. Hector, Jr., and J. B. Adams, *Adhesion, stability, and bonding at metal/metal-carbide interfaces: Al/WC*, Surf. Sci. (2001), submitted.

[191] G. Song, A. Remhof, K. Theis-Bröhl, and H. Zabel, *Extraordinary adhesion of niobium on sapphire substrates*, Phys. Rev. Lett. **79**, 5062 (1997).

[192] D. A. Muller, D. A. Shashkov, R. Benedek, L. H. Yang, J. Silcox, and D. N. Seidman, *Atomic scale observations of metal-induced gap states at $\{222\}$ MgO/Cu interfaces*, Phys. Rev. Lett. **80**, 4741 (1998).

[193] R. Reeber and K. Wang, *Thermophysical properties of alpha-tungsten carbide*, J. Am. Ceram. Soc. **82**, 129 (1999).

[194] D. J. Siegel, L. G. Hector, Jr., and J. B. Adams, *First-principles study of metal–carbide/nitride adhesion: Al/VC vs. Al/VN*, Acta mater. (2001), submitted.

[195] X.-G. Wang, W. Weiss, S. K. Shaikhutdinov, M. Ritter, M. Petersen, F. Wagner, R. Schlögl, and M. Scheffler, *The hematite (0001) surface: Evidence for domains of distinct chemistry*, Phys. Rev. Lett. **81**, 1038 (1998).

[196] D. Roundy, C. R. Krenn, M. L. Cohen, and J. W. Morris, Jr., *Ideal shear strengths of FCC Aluminum and Copper*, Phys. Rev. Lett. **82**, 2713 (1999).

Vita

Donald Jason Siegel was born on August 7th, 1973 in Youngstown, Ohio to Donald Joseph and Joyce Cathleen Siegel. The oldest of two children, he graduated as class valedictorian from Boardman High School in 1991, and attended Case Western Reserve University in Cleveland. As an undergraduate he began his study of computational physics under the supervision of Dr. Philip Taylor, and developed a Metropolis Monte Carlo simulation of chiral nematic liquid crystals as part of his senior research project. He was a US Department of Education National Science Scholar during the years 1991-1995.

Upon graduation in 1995 with a B.S. in Physics, he enrolled in the Ph.D. program in the Department of Physics, University of Illinois at Urbana-Champaign, where he served as a teaching assistant during the 1995-1996 academic year. In the summer of 1996 he joined the research group of Dr. Jim Adams, then part of the Materials Science and Engineering Department, where he began applying Density Functional Theory to the study of metal–ceramic interfaces. During the summers of 1997-1999 he was a student intern at the Alcoa Technical Center, where he collaborated with Lou Hector, Jr. on his thesis research. He was also an intern at the General Motors Materials and Process Lab during the summer of 2000, under the supervision of Y.T. Cheng and Tom Perry. At GM he gave weekly lectures on *ab initio* simulation techniques and offered instruction in the use of the *Vienna ab initio Simulation Package*.

After receiving a Ph.D. in physics (August, 2001) for his thesis entitled *First-Principles Study of Metal–Ceramic Interfaces*, he will be a Postdoctoral Research Associate in the Thin-Film & Interface Science Group at Sandia National Laboratories, Livermore, CA.

Graduate Publications:

1. A. Landa, P. Wynblatt, D. J. Siegel, J. B. Adams, O. N. Mryasov, and X. Y. Liu, *Development of Glue-type Potentials for the Al-Pb System: Phase Diagram Calculation*. Acta mater. **48**, 1753 (2000).

2. J. B. Adams, L. G. Hector, Jr. D. J. Siegel, H. Yu, J. Zhong, and Y. T. Cheng, *Adhesion, Lubrication, and Wear on the Atomic Scale*. Surf. Interface Anal. **31**, 619 (2001).

3. L. G. Hector, Jr. G. A. Nitowski, S. M. Opalka, L. Weiserman, D. J. Siegel, H. Yu, and J. B. Adams, *Investigation of Vinyl Phosphonic Acid/Hydroxylated α-Al_2O_3(0001) Reaction Enthalpies*. Accepted into Surf. Sci.

4. D. J. Siegel, L. G. Hector, Jr., and J. B. Adams, *Adhesion, Atomic Structure, and Bonding at the Al(111)/α-Al_2O_3 Interface: a First-Principles Study*. Submitted to Phys. Rev. B.

5. D. J. Siegel, L. G. Hector, Jr., and J. B. Adams, *Adhesion, Stability, and Bonding at Metal/Metal-Carbide Interfaces: Al/WC*. Submitted to Surf. Sci.

6. D. J. Siegel, L. G. Hector, Jr., and J. B. Adams, *First-Principles Study of Metal–Carbide/Nitride Adhesion: Al/VC vs. Al/VN*. Submitted to Acta mater.

7. D. J. Siegel, L. G. Hector, Jr., and J. B. Adams, *Trends in Metal–Ceramic Adhesion from First-Principles Simulation*. Submitted to Phys. Rev. Lett.

8. D. J. Siegel, L. G. Hector, Jr., and J. B. Adams, *Electronic Structure and Bonding at the Al–terminated Al(111)/α-Al_2O_3(0001) Interface: A First-Principles Study*. Mat. Res. Soc. Proc. **654**, AA4.2.1 (2001).

9. D. J. Siegel, L. G. Hector, Jr., and J. B. Adams, *Stoichiometry and Adhesion of Al/WC*. Mat. Res. Soc. Proc. **677**, AA4.25.1 (2001).

10. Y. Li, D. J. Siegel, and J. B. Adams, *Development of an EAM Potential for Ta via the Force Matching Method*. In preparation.